INJECTION MOLDED POLY(ETHYLENE TEREPHTHALATE)-GRAPHENE NANOCOMPOSITES

By

SUDHEER BANDLA

Bachelor of Technology in Mechanical Engineering
Acharya Nagarjuna University
Guntur, Andhra Pradesh, India
2006

Master of Science in Mechanical and Aerospace Engineering
Oklahoma State University
Stillwater, Oklahoma
2010

Submitted to the Faculty of the
Graduate College of the
Oklahoma State University
in partial fulfillment of
the requirements for
the Degree of
DOCTOR OF PHILOSOPHY
May, 2015

INJECTION MOLDED POLY(ETHYLENE TEREPHTHALATE)-GRAPHENE NANOCOMPOSITES

Dissertation Approved:

Dr. Jay C. Hanan

Dissertation Adviser

Dr. Raman P. Singh

Dr. A. Kaan Kalkan

Dr. Ranji Vaidyanathan

ACKNOWLEDGEMENTS

I dedicate this work to my parents (Sasikala and Prasada Rao) for the support and inspiration they have provided in pursuing my dreams.

I take this opportunity to thank my advisor Dr. Jay C. Hanan, for his continuous guidance and support throughout the program. It is my great pleasure to have worked under his supervision and learn from his extensive knowledge in the field of material science. It was his encouragement that enabled me to gain a unique experience in both academic and industrial environments.

I want to thank my committee members; Dr. Raman P. Singh, Dr. Kaan Kalkan and Dr. Ranji Vaidyanathan for their time, valuable suggestions and permitting me use the equipment in their labs, for successfully completing this work.

This work would not have been possible without the support of Niagara Bottling LLC. I would like to thank Mr. Rali Sanderson and Mr. Bill Hall for their continuous belief and support towards this work. I also want to thank Mr. Kaokam Sanouvong, Mr. Reaj Ahmed, Mr. Mark Aceves and the current and past R&D team members at Niagara Bottling LLC for their timely assistance in effectively completing this work.

I need to thank the following people and organizations for their assistance: XG Sciences Inc. and Dr. Lawrence Drzal for their inputs related to nanoplatelets, Ovation Polymers for compounding work, Prof. Avraam Isayev and U. Akron for ultrasound-assisted compounding, Dr. Prasanna Perera, Mr. Joe Drbohlav, Auriga Polymers, for their polymerization reactor, Dr. Gregory Kamykowski, TA Instruments for inputs on rheology analysis, Dr. Erica Tseng for rheology measurements, Dr. Alexander Sasov, Bruker Micro CT, and Mr. Jeff Gulb, ZEISS X-ray Microscopy for Nano-CT,

Ms. Michelle Forbes, Sonoscan Inc., for ultrasound micrographs, Husky Injection Molding Systems, Mr. Stephen Dieter, Dieter Scientific, for their help with molding systems, Dr. Sandip P. Harimkar for density measurement setup, and Dr. Kaan Kalkan and his student Sriharsha Karumuri for Raman spectroscopy analysis.

I am fortunate to have made many friends over the past 7 years of my stay at OSU, during my Master's and PhD, who had positive influences on me. I will remember all those people for the rest of my life. Saravan Kumar Shanmugavelayudam, Ashish Singh, Arif Rahman, Kunal Mishra, Nikhil Satyala, and Kedar Pai are few people to name. I would like to thank all my current and previous lab colleagues Hrishikesh Bale, Masoud Allahkarami, Balaji Jayakumar, Advait Bhat, Vahid Shabafrooz, Chandra Sekhar Meduri, Arjun Rajukutty, Rohit Vaidya, Praful Bari and Ranjan Mahadevan for their support.

I would like to thank my brother, Sunil Bandla and all other family members who have encouraged me all these years. I need to thank my roommate and good friend, Sriharsha Karumuri, especially for the never ending and thought provoking discussions, and continuous support. I also would like to thank all my friends, round the globe, for their constant encouragement.

Name: SUDHEER BANDLA

Date of Degree: MAY, 2015

Title of Study: INJECTION MOLDED POLY(ETHYLENE TEREPHTHALATE)-GRAPHENE NANOCOMPOSITES

Major Field: MECHANICAL AND AEROSPACE ENGINEERING

Abstract: Polymer nanocomposites are known for their superior properties (mechanical, thermal, etc.) compared to conventional composites. Nanoscale reinforcements are used to make such composites as they have fewer defects and higher aspect ratios. Achieving uniform dispersion of nanoparticles in a polymer matrix is fundamental in realizing their advantage as reinforcements. Poly(ethylene terephthalate) (PET) is an aromatic polyester, commonly used in textile, packaging and engineering applications. Improving the properties of PET through addition of nanoreinforcements can enable new applications. This study investigates the processing and performance of PET-graphene nanocomposites.

Graphene is a relatively new nanomaterial with a unique combination of properties. Because of their higher effective surface area and favorable aromatic-aromatic interactions, graphene is a suitable reinforcement to improve mechanical properties of PET. Graphene nanoplatelets (GNPs) – multi-layer graphene of 5 μm average diameter were used to reinforce PET. PET and GNPs were melt compounded as high concentration masterbatches (up to 15% wt.) through twin-screw extrusion, with and without ultrasound energy. PET-GNP nanocomposites were prepared through high speed injection molding process. Masterbatches obtained from compounding were used to make nanocomposites at different weight fractions (0.5% - 15%).

PET-GNP nanocomposites were characterized for their mechanical (Young's modulus and strength), thermal (crystallization) and rheological properties. At 15% GNP weight fraction, Young's modulus of PET improved by a maximum of 224%. Dispersion analysis using transmission electron micrographs indicated a decrease in the interparticle distance of nanoplatelets with an increase in GNP concentration. Analytical predictions based on Hui-Shia micromechanical model are in agreement with the measured experimental modulus. While graphene nanoplatelets did increase the strength of PET at 15% weight fraction, its failure behavior transitioned from ductile to brittle at above 2% weight fraction. Improvement in Young's modulus of nanocomposites prepared using ultrasound-assisted compounding was not significant compared with those from twin-screw compounding. Graphene nanoplatelets acted as a nucleating agent and increased the crystallization rate. However, limited PET chain mobility above 2% GNP weight fraction counteracted nucleation and decreased the crystallization rate.

TABLE OF CONTENTS

Chapter Page

LIST OF TABLES

Table Page

LIST OF FIGURES

Figure Page

CHAPTER I

INTRODUCTION

1.1 Overview

Composites are defined as multiphase materials, which can be found in nature or man-made. Man-made composites are formulated using one or more materials for achieving properties that are not available individually [1]. Composites can be classified based on the type of the continuous (matrix) and the dispersed phases (reinforcement) [2]. Composite materials with one of the constituent phases (primarily the dispersed phase) having at least one dimension on the order of 1-100 nanometers are denoted as nanocomposites [3]. Nanocomposites can further be classified based on the category (organic/inorganic), and geometry of the nanoscale reinforcement. The first reference to the use of the term "nanocomposite" in scientific literature dates back to 1986 [4]. Nevertheless, nanocomposites can be cited as early as the 1950's [5]. They are part of nature, only to be acknowledged recently with progress in fields such as electron microscopy. A few well-studied examples of natural nanocomposites include human bone, seashells, spider silk, and armored fish [6]. It is understood that the structural hierarchy (structure at multiple length scales) built into these materials makes them perform exceptionally well compared with others of the same chemistry [7].

Material properties of composites are known to be dependent on the interaction between the matrix and the dispersed reinforcement. Large surface areas per unit volume at the nanoscale make nanomaterials function differently from their bulk counterparts. With increased interactions between the matrix and the dispersed phase, nanocomposites are considered superior over conventional composites [8]. They provide the advantage of having new properties (conductive polymers) without compromising the existing beneficial properties (strength or toughness) [9].

Polymer nanocomposites evolved out of the need for lighter (compared to metals) and higher performance materials (with improved mechanical properties, and thermal stability over the original polymer). Also, the availability of characterization tools appropriate for visualizing the small scale interactions of nanomaterials contributed to their development. Successful exfoliation and dispersion of modified clays into Nylon-6 by researchers at Toyota [10], is an early example of a polymer nanocomposite. Unique properties and the prospect for large number of polymer-nanoreinforcement combinations for making nanocomposites, have set off new possibilities in a wide range of fields from aerospace, sensors, electronics, and fuel cells to textiles, packaging, structural, armor, and biomaterials [11-15].

Poly(ethylene terephthalate) (PET) is an aromatic semi-crystalline thermoplastic polyester, synthesized in the early 1940s. With a global production of 70 M tons/year [16], PET holds a significant position in the global plastic industry. Well known for its mechanical (Young's modulus, strength, and toughness), thermal (high glass transition, and melting points), chemical resistance, and optical properties, PET is commonly used for commodity and engineering applications also due to its low cost (< $1/lb.). PET exhibits an interesting microstructure where longitudinal stretching forms strong fibers with high molecular chain orientation, and bi-axial stretching forms strong films. Linear PET is naturally semi-crystalline. Thermal (rate of cooling) and mechanical history (stretching) can drive it to be amorphous or more crystalline, thus influencing its mechanical properties [17-19]. Its maximum consumption is in fiber, packaging, filtration, and thermoforming industries. Nevertheless,

the use of PET is constrained due to the slow crystallization rate [20] and limited barrier performance [21] compared to other polyesters (PBT, PTN, etc.).

Initiatives to lightweight materials used across industries like: packaging, automotive, and aerospace, promote improving properties through better control on material processing and addition of reinforcements. For example, increasing the crystallinity of PET improves mechanical and barrier properties. However, restrictions with the material (crystallization rate) and industrial processes (cooling rate, cycle time, and stretching process) in maximizing crystallinity, limit this improvement. With the scope for improvement in the properties of PET, methods like: blending with other polymers and the addition of inorganic particles (as nucleating agents and reinforcements) have been pursued. However, often the color or clarity of PET is compromised. Progress in the field of nanomaterials and associated advantages, such as large surface areas and low weight fractions, have led to the development of PET nanocomposites [22]. The addition of nanomaterials at low fractions helps in improving the specific properties (less increase in density). Improving the physical (mechanical, thermal, and electrical) properties can make it more effective for applications similar to automotive, aerospace, and protective apparel. PET nanocomposites have been studied for about two decades. Different types of nanoreinforcements (Clay, CNF, CNT, Graphene, SiO_2, etc.) were used for improving the mechanical [23], thermal [22], barrier [24], electrical [25], fire retardation [26, 27], optical [28], surface properties [28], and crystallization kinetics [29] of PET.

Exfoliation or separation of the nanoreinforcements into individual entities and their uniform dispersion in to the polymer matrix is essential for the success of polymer nanocomposites. To achieve uniform dispersion of nanoreinforcements in polymers, multiple approaches including: melt-compounding, *in-situ* polymerization, and surface treatment of the nanoreinforcements have been tested. In the case of PET-clay nanocomposites, due to the limited polarity of PET molecules compared to Nylon, a compatibilizer was commonly used to facilitate dispersion. Nevertheless, the use of nanoclay for reinforcing PET experienced certain difficulties. For example, PET processing

involves high temperatures (270°C – 290°C) which can degrade the compatibilizer [30], decrease thermal stability [31], and subsequently decreases the molecular weight of PET through chain scission. This decrease in the molecular weight will result in deterioration of polymer properties. Carbon nanomaterials (Carbon nanofibers, Carbon nanotubes (CNTs) and Graphene) are advantageous over nanoclays, due to their superior properties (mechanical, thermal, electrical, and barrier) and simple chemistry. Multi-fold property improvements can be achieved through the dispersion of carbon nanomaterials into polymers [32]. The cost of the carbon nanotubes and the need for surfactants, limits the application of CNT nanocomposites. Graphene is the latest addition to the list of available carbon nanomaterials, with a unique combination of properties. Graphene is a single layer of carbon atoms similar to an unzipped single walled carbon nanotube. With a more effective surface area (available surface area per unit volume is double with graphene for the polymer to interact on both the faces, compared to the exterior face of a CNT), single layer graphene can be twice as effective as CNTs in reinforcing polymers. For the aforementioned reasons, graphene reinforcements were pursued here to improve the properties of PET.

Table 1: Potential improvement in polymer properties through the addition of nano-fillers.

Nano-filler	Mechanical	Electrical	Thermal	Barrier
Graphene	×	×	×	×
CNT	×	×	×	×
Clay (MMT)	×		×	×
SiO_2	×	×	×	
POSS	×		×	

Research Gap

Graphene is a relatively new nanomaterial. The development of graphene synthesis methods [33] in conjunction with the introduction of new graphene-based nanomaterials (graphene oxide, expanded

graphite, and graphene nanoplatelets [34]) has made graphene commercially viable. However, limited information on the effectiveness of the abovementioned graphene-based nanomaterials, limits their application in fabricating polymer nanocomposites. This emphasizes the need to investigate the influence of graphene nanomaterials in reinforcing polymers. With PET being one of the most used polymers, investigating the fabrication and improvement in properties of PET-graphene nanocomposites will be advantageous.

Early research on PET nanocomposites was based on laboratory processing. In that case, there was limited control on the production process variables (cooling rate and injection speed for example) as PET requires unusually high melt temperatures and quenching rates compared to most polymers and the capabilities of laboratory equipment. As explained earlier, processing conditions besides the addition of nanoreinforcements can induce crystallinity in PET. Then again crystallinity can influence the mechanical properties [17], thermal [35] and electrical [36] conductivities for PET. Crystallinity can never be consistent at the nano-scale. There will always be a crystalline domain as well as an amorphous boundary and even a more substantial amorphous matrix surrounding crystals in semi-crystalline PET. Therefore, examining nanocomposites with a uniform amorphous matrix eliminates some of the confusion in understanding the influence of nanoreinforcements. This understanding will assist towards effectively modeling nanocomposite properties and can lead to informed studies of semi-crystalline matrix versions of the composite.

1.2. Problem Statement

In spite of the decades of research in the field of nanocomposites, their manufacturing is still limited to relatively low volumes compared to conventional composites. Achieving good dispersion is the key for successful growth in applications of polymer nanocomposites. From literature, melt-compounding and *in-situ* polymerization were found to be the most studied techniques for the preparation of PET-Graphene nanocomposites. *In-situ* polymerization is effective in dispersing

graphene [37]. Nevertheless, the use of *in-situ* polymerization is limited due to process complexity (in attaining the desired molecular weight [37]) and the need for expensive reactors. Melt-compounding is a straight-forward approach involving shear mixing, but that alone has not been effective in dispersing graphene in the several polymer systems tested (decrease in the potential strength [38]). Because of the limited effectiveness of the abovementioned techniques, a new method for dispersing graphene in PET, ultrasound assisted compounding was tested here.

Another important aspect for the implementation of polymer nanocomposite applications is the ability to predict their properties. This will provide flexibility in designing manufacturing processes and reduce developmental costs. Traditional composite models (rule of mixtures) are not accurate in predicting the properties of nanocomposites. Micromechanical models based on continuum theory are effective in estimating short fiber composites. Few studies have reported the applicability of these models for nanocomposites [39, 40]. This study is the first time two different micromechanical models have been evaluated for PET-Graphene nanocomposites.

1.3. Research Objective

1. Fabrication of PET-Graphene nanocomposites

The current work investigates the effectiveness of graphene nanoplatelets (GNP) in reinforcing poly(ethylene terephthalate) (PET). As stated previously, achieving homogenous dispersion of the nanoplatelets in PET is critical for improving bulk properties. Another aspect in the selection of the dispersion method is process simplicity. Dispersing graphene in PET through a solvent approach is nontrivial, as PET dissolves only with strong chemicals such as: trifluroacetic acid/dichloromethane (1:1 v/v). PET used for all practical applications is highly viscous (500 – 1000 Pa s) with a melting temperature of 260°C - 280°C. Selecting a processing method that can allow working at high temperatures and highly viscous materials is necessary. Therefore, to achieve uniform dispersion, twin-screw compounding and ultrasound-assisted twin-screw compounding were employed for

preparing the nanocomposite (masterbatch) pellets at high loading fractions (up to 15%). Ultrasound-assisted compounding was carried out at three different ultrasound amplitudes to understand the effect on dispersion. The melt-compounded masterbatches were used to injection mold nanocomposites at different weight fractions. In order to test nanocomposites with an amorphous phase matrix, a sample geometry (tube) which aids in fast cooling and similar to typical industrial processing of PET was also employed.

In-situ intercalative polymerization of PET was attempted with the objective of evaluating nanocomposites with the level of graphene nanoplatelets dispersion, attainable through solution mixing. The surface area of the nanoplatelets is another important factor, as it can be related to the interfacial area between the polymer and nanoplatelets. Therefore, *in-situ* polymerization was attempted using nanoplatelets of two different average surface areas to begin to understand the effect of surface area on polymerization process and nanocomposite properties.

2. Evaluate the performance of PET-Graphene nanocomposites

The nanocomposites were analyzed for their mechanical properties (Young's modulus and strength). Dispersion of the nanoplatelets in nanocomposites was characterized using electron microscopy, X-ray Diffraction, and Melt Rheology. Thermal properties were studied to understand the effect of nanoplatelets on the melt and crystallization behavior of PET.

Ultrasound treatment of polymer solutions is known to induce chain scission, which is dependent on molecular weight, ultrasound intensity, temperature, and concentration [41, 42]. However, ultrasound effects on PET either in solution or melt states has not been studied. Therefore, for ultrasound processing, it is necessary to understand its effect not only on the composite but on PET as well. Molecular weight analysis of ultrasound treated PET and PET nanocomposites using Gel Permeation Chromatography (GPC) will help in quantifying any change.

Modelling nanocomposites properties requires microstructure information. Transmission electron micrographs were used in calculating the aspect ratio of the platelets. Using the platelet geometry information from the electron micrographs, nanocomposite properties were calculated based on two-phase micromechanical models developed by Halpin-Tsai [43] and Hui-Shia [44]. These micromechanical relations, originally developed for oriented short-fiber composites, were also used frequently for analyzing the modulus of nanocomposites [39, 45, 46]. Model predictions based on the actual microstructure information were compared with experimental data and the ideal condition (dispersion of single layer graphene) for evaluating the effectiveness of the dispersion method used.

CHAPTER II

BACKGROUND

2.1. Poly(ethylene terephthalate)

Poly(ethylene terephthalate) is aromatic semi-crystalline polyester. PET is synthesized through condensation polymerization, using Terephthalic acid (TPA) and Ethylene Glycol (EG) or Dimethyl Terephthalate (DMT) and Ethylene Glycol (EG) as raw materials [47]. A multi-step polymerization process is used in the manufacture of PET, to achieve the desired molecular weight and to minimize byproduct formation (e.g., Acetaldehyde). The molecular structure of PET is shown in Figure 1. The presence of a rigid aromatic ring in the molecular chain gives rise to the high melting and glass transition temperatures and, stiffens the polymer [48, 49]. It also makes the molecule have a nearly planar arrangement in the crystal structure. This combination of physical properties and chemical inertness makes PET suitable for applications such as fibers, packaging, and engineering molding. PET was originally developed as a fiber polymer with low molecular weights. Higher molecular weight PET grades were introduced with the objective of expanding its application beyond fibers. PET used for different applications are commonly classified on the basis of its Intrinsic Viscosity (I.V.). For example, PET of 0.6 dL/g I.V. (M_w ~ 54000 g/mol) is fiber grade and PET of 0.80 dL/g I.V (M_w ~ 82000 g/mol) is blow molding grade. Higher molecular weight provides better performance in terms of structural stability for molded components, but limits the processing ability of the material.

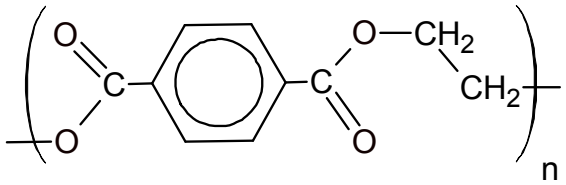

Figure 1: Molecular structure of PET.

Though PET is limited in terms of the crystallization rate and barrier performance compared to PBT and other polyesters, it's relatively low price makes it competitive. Due to this advantage, the notion of improving properties through the addition of fillers [50] and reinforcements receives wide attention. In the case of fibers, efforts to generate an extended-chain structure for achieving higher strengths were not successful, as the rapid relaxation of the molecular chains during the cooling process destroys the orientation [47]. Nanomaterials provide the advantage of reinforcing PET while minimizing the change in density of the obtained composite material. Furthermore, having the reinforcement size on the same order of the polymer coil (radius of gyration, R_g) not only provides a larger interface, but also influences mobility [51]. In the following sections, the advantage of nanoreinforcements and the types of carbon nanomaterials are discussed in detail.

2.2. Nanoreinforcements

Nanoreinforcements can be categorized based on their geometry into three different groups namely: nanoparticles, nanotubes and nanoplatelets. Nanoreinforcements are advantageous over larger reinforcements. Using Griffith's crack theory and Weibull analysis, Fukushima [52] explained that the smaller the particles, the stronger and more effective they are in reinforcing the matrix compared to their larger counterparts [53]. Another advantage is the available surface area for a unit volume. In the case of spherical particles, the surface area to volume ratio is inversely proportional to the particle radius. Figure 2 highlights the increase in the total interfacial area ($T_{Interface}$) per total volume, for spherical reinforcements as their size changes from microscale to nanoscale. The surface energy available per unit area will be high for nanoparticles, making them

chemically active [54]. These advantages have sparked a large interest in the research community to explore the use of nanoreinforcements for a number of applications [8].

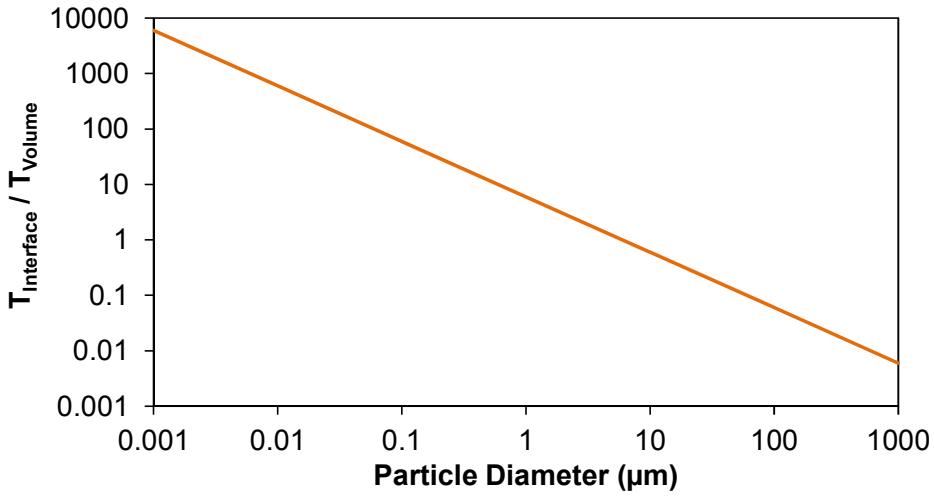

Figure 2: Particle size effect on the interface (for a spherical particle).

In the case of polymer nanocomposites, the selection of nanoreinforcements depends on many factors such as the polymer used, intended application, target properties, desired form of interaction (chemical or physical) with the polymer, material handling concerns, processing method, and cost [9]. Along with chemistry, the shape (globular particles, spheres, crystals, sheets, wires, and tubes) of the nanoreinforcement influences the characteristics of the polymer nanocomposite [9].

Based on their chemistry, nanoparticles can be classified into organic and inorganic. To date, a number of nanoparticles such as organoclays (MMT), metal nanoparticles (e.g. Al and Ag), metal oxides (e.g. Al_2O_3, ZnO, and silica), cellulose nanocrystals, and carbon derivatives (CNT's, Fullerenes, Graphite oxide, and Graphene) have been studied in polymer nanocomposites. Nanoclays and carbon nanomaterials like CNT's and Graphene were studied more (as seen from Figure 3) compared to other nanoparticles for making polymer nanocomposites.

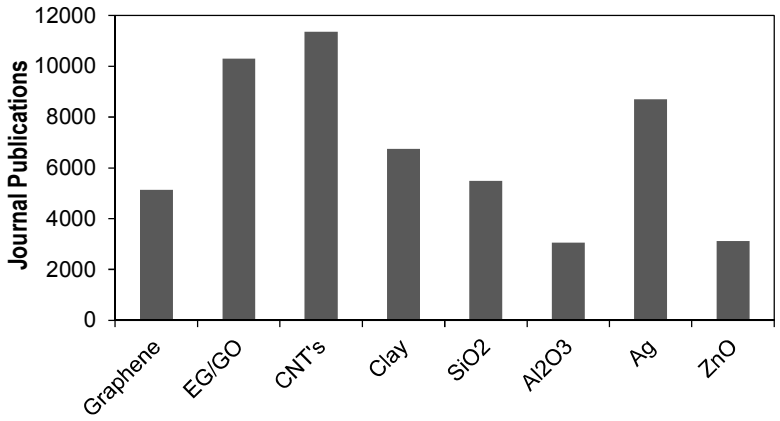

Figure 3: Number of journal publications on polymer nanocomposites using different nanoparticles (data collected from ScienceDirect on 12/30/2014).

2.3. Carbon Nanoreinforcements

Carbon is an interesting element of the periodic table, because of its unique hybridization properties and the ability to manipulate its structure [55, 56]. Commonly found in nature in a wide variety of compounds, it plays an important role from a chemistry standpoint [55]. Carbon finds applications in several industries and processes commonly in the form of graphite, amorphous carbon, and diamond. At the nanoscale, carbon materials are also interesting, showing unique structures (as shown in Figure 4) and properties. The discovery of fullerene in 1985 [57], and carbon nanotubes (CNTs) in 1991 [58], has created a new interest towards carbon-based nanomaterials with exciting properties. Later in 2004, the isolation of graphene and experimental demonstration of its properties by Novoselov *et al.* [59], accelerated carbon nanomaterials research [60].

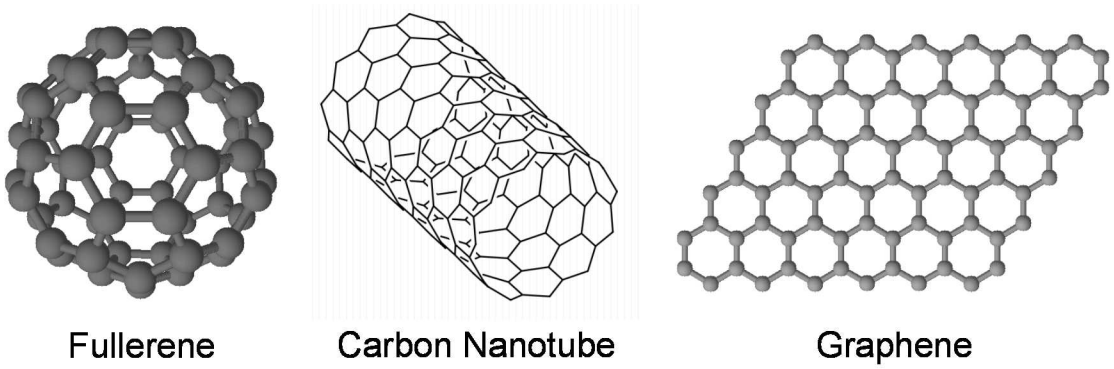

Figure 4: Carbon allotropes.

In the field of polymer nanocomposites, carbon nanomaterials (CNTs and Graphene) were considered over nanoclays and metal nanoparticles as reinforcements because of their ability to advance polymer properties on multiple fronts without compromising the existing desired properties. This will help in opening up new application areas, which were not imagined previously. As the properties of both CNTs and graphene depend on their purity, large scale synthesis of these materials with high purity is considered an important step towards realizing their advantages. The importance of graphene as a nanoreinforcement and its production and properties are discussed in the following sections.

2.4. Graphene

Graphene is defined as a single layer of carbon atoms with a two-dimensional structure (sp^2 hybridization, planar hexagonal arrangement with a C─C bond distance of 0.142 nm). It is a newly recognized nanoscale reinforcement that has generated enormous interest due to its intrinsic properties (mechanical, thermal, and electrical) [61]. The thickness of a single graphene sheet can be estimated as 0.335 nm (based on the van der Waals radii) [62]. One of the first two-dimensional materials available, graphene is considered to be the 'miracle material' with the potential to replace many contemporary materials used for different applications [63]. References to graphene and its derivative materials can be dated back to the early 19^{th} century [64].

Graphene was considered a hypothetical material and theoretically studied as the mother material for many other allotropes of carbon for more than half a century. Experimental confirmation of graphene's outstanding electrical properties gave rise to a new field of two-dimensional materials.

In the process of graphene development, researchers came up with different graphene based materials such as single layer graphene sheets (SLGS or 'graphene'), few-layer graphene (FLG), multi-layer graphene (MLG), and exfoliated graphene platelets.

2.4.1. Properties

Graphene is superior over other carbon based nanoreinforcements such as CNT's, CNF's, and Expanded Graphite (EG), in terms of its aspect ratio, flexibility, transparency, thermal conductivity and low coefficient of thermal expansion (CTE) [65].

The density of single layer graphene was calculated at 0.77 mg m^{-2}. Until recently, graphene was regarded as the strongest material [66]. It remains the strongest material with appreciable size. A Young's modulus of 1.02 ± 0.03 TPa (0.2 TPa for 4130 steel[1]) and strength of 130 ± 10 GPa (0.7 GPa for 4130 steel) were measured for a single layer graphene sheet suspended over open holes, by means of an atomic force microscope (AFM) nanoindentation technique [67]. Graphene is found to exhibit a negative coefficient of thermal expansion, $\alpha = -4.8 \pm 1.0 \times 10^{-6}\ K^{-1}$ through the 0-300 K temperature range [68] and a very high thermal conductivity (K) of 3000 W mK^{-1} comparable to that of CNT's [69]. Wang *et al.* [70] found graphene sheets are hydrophobic and determined their surface energy at room temperature to be 46.7 mJ m^{-2}.

The abovementioned properties are for a high quality single layer graphene. However, current methods for producing pristine single layer graphene are not yet adequate to serve the constantly increasing demand. Therefore, studying the effect of increasing thickness from single layer to multi-layer graphene on properties is necessary. Properties of multi-layer graphene are different

[1] AISI 4130 Steel, normalized at 870°C, data accessed on 1/10/2015 from www.matweb.com.

from that of single layer graphene. The influence of the number of layers ('*n*'), changes for each specific property. A single layer graphene sheet exhibits up to 97.7% transparency (2.3% absorption) and decreases linearly as the number of layers increases [71]. Gosh *et al.* [72] found that the thermal conductivity of graphene drops by more than 50% as the number of layers increases from 2 to 4 and is comparable to that of bulk graphite when *n* is more than 8. Through molecular dynamics (MD) simulations, Zhang *et al.* [73] have studied the mechanical properties of graphene with the change in layer number, temperature, and isotope substitution. They found that the modulus of graphene sheets decreased with increase in temperature and with increase in ^{13}C isotope density, but increased with increase in the number of layers. However, structural mechanics based atomistic modeling of multi-layer graphene structures [74], molecular simulation of the covalent and van der Waals interactions between layers [75], and experimental measurements [76], point towards a decrease in the modulus with increasing '*n*'. Mechanical properties of graphene nanoplatelets such as stiffness and poisson's ratio was found to decrease with increase in the number of comprising layers, from molecular dynamics simulations [74]. Georgantzinos *et al.* [74] estimated that the stiffness of the nanoplatelets comprising five layers decreases by 15% compared to single layer graphene. They also noticed that the properties of the graphene differ based on their orientation. Gong *et al.* [77] found that the effective modulus of multi-layer graphene with 10 layers to be 380 GPa, which is less than that of a graphite crystal. The effective Young's modulus is determined based on the stress transfer efficiency between layers for a multi-layer graphene. It deviates from the modulus of a single layer graphene when the multi-layer graphene is of more than 3 layers, at which the core layer(s) will not be in contact with the polymer. Single and multi-layer graphene used in these studies are pristine with minimal defects (from mechanical cleavage). This is an ideal condition and cannot be considered while using graphene based nanoreinforcements prepared through different techniques, discussed in the following section.

2.4.2. Preparation

Single layer graphene can be obtained through 'top down' or 'bottom up' approaches. The separation of graphene sheets from graphite through mechanical cleavage is a 'top down' approach. Though graphene obtained from this method is pristine and useful for testing purposes, it is not practical for acquiring significant quantities [78]. Alternatively, graphene can be prepared by 'bottom up' approaches through chemical methods. Chemical Vapor Deposition (CVD) [78], epitaxial growth, and synthesis through colloidal suspension are a few important methods for making graphene [33, 79]. In addition to these methods, a few other methods reported are: making graphene from CNT's by chemical etching [80] and flash reduction of graphite oxide [81].

Working with single layer graphene is deemed important for disciplines namely: physics, transparent (display), and flexible electronics. Large graphene sheets were successfully synthesized through CVD [82]. However, the use of graphene from CVD processes for composite applications is not yet practical. The synthesis of graphene based materials through chemical treatment of precursor materials such as graphene oxide [83], graphene intercalated compounds (GIC), and graphite is one of the most common approaches for scale-up of manufacturing. In some of the methods, chemically treated intercalated compounds were exfoliated using secondary processes such as oven heating, microwave heating [52], ultrasonication [84], and milling. Physical properties (aspect ratio, defect density) of the graphene obtained from the aforementioned approaches will change and can be targeted for different applications as shown in Table 3.

Graphene based nanomaterials have the potential to be produced in a large scale. Over the past decade, several developments (Exfoliated Graphene Nanoplatelets (xGnP)[2] and Nano Graphene

[2] XG Sciences Inc. by Dr. Lawrence T. Drzal, Michigan State University.

Platelets (NGP)[3]) in the area of making exfoliated graphene have led to the reduction in cost of graphene materials (as shown in Table 2). Growing knowledge on production and the potential advantages of graphene materials for a number of applications [85] will help in driving the cost down while improving the quality of the graphene being produced.

Table 2: Price of graphene nanoplatelets in bulk.

Year	Price of xGnP-M-5®
2011	$ 229/ kg
2013	$ 139/ kg
Future Projections [86]	$ 15/ kg

[3] Angstron Materials Inc. by Dr. Bor Jang, Wright State University.

Table 3: Properties of graphene through different methods [63].

Method	Crystallite size (µm)	Sample size (mm)	Charge carrier mobility (at ambient temperature) ($cm^2\ V^{-1}\ s^{-1}$)	Applications
Mechanical exfoliation	> 1,000	> 1	> 2×10^5 and > 10^6 (at low temperature)	Research
Chemical exfoliation	≤ 0.1	Infinite as a layer of overlapping flakes	100 (for a layer of overlapping flakes)	Coatings, paint/ink, composites, transparent conductive layers, energy storage, bioapplications
Chemical exfoliation via graphene oxide	~100	Infinite as a layer of overlapping flakes	1 (for a layer of overlapping flakes)	Coatings, paint/ink, composites, transparent conductive layers, energy storage, bioapplications
CVD	1,000	~1,000	10,000	Photonics, nanoelectronics, transparent conductive layers, sensors, bioapplications
SiC	50	100	10,000	High-frequency transistors and other electronic devices

2.4.3. Applications

Graphene with its unparalleled combination of properties is regarded as the "game changer" for many industries. Some of the areas where graphene will find a great deal of applications include electronics, photonics, composite materials, conductive paints, inks and coatings, barrier enhancement, filtration, friction reducers, electromagnetic shielding, sensors, solar cells, energy storage, metrology, and tissue engineering. In the roadmap presented for graphene, Novoselov *et al.* [63] have projected a timeline (shown in Figure 5) for the development of graphene production and graphene-based products. As not every application requires the same level of quality, both the growth of graphene based products and the development of large scale production processes for high quality graphene are presented as parallel events. The development of graphene based composite materials is one example, where graphite flakes with multiple layers were also found to be effective in improving properties [87]. After 2004, there has been an explosive growth in the number of publications and patents based on graphene research [60, 88-

90]. With increasing involvement of larger corporations and the rapid transfer of technologies from academic research (graphene based spin-offs [91]), graphene based products can be realized in a short time [63].

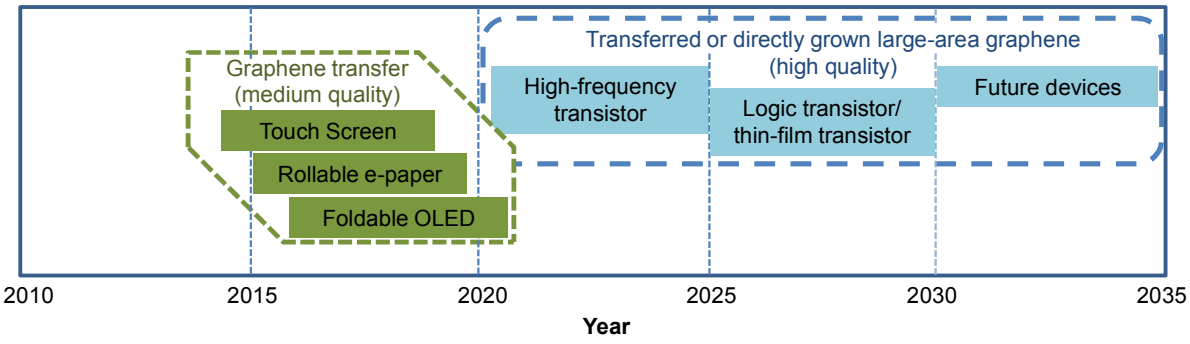

Figure 5: Projected timeline of graphene based products in the electronics industry [63].

2.5. Processing of Nanocomposites

Composite manufacturing is an extensively studied field with a number of processes available based on the size and application of the final product. Nanocomposite processing involves a process for dispersion of the nanoreinforcement and forming processes for the intended final application. Even after two decades from the introduction of first polymer nanocomposites, not many are available in the commercial domain. The feasibility of nanocomposites also depends on cost, the availability of nanoparticles, and suitable manufacturing processes. Manufacturing techniques such as: injection and compression molding, Layer-by-Layer (LBL) manufacturing [92], *in-situ* microemulsion polymerization [93, 94], and spinning [95, 96] are used for polymer nanocomposites. Selection of the process depends on the matrix resin and type of the nanoparticles used, as not all of them are effective with every polymer-nanoparticle system. Injection molding is considered the most important of all plastic processing techniques because of its, speed, scalability, and tolerance to a wide range of materials [97]. Methods attempted for achieving uniform dispersion of nanoreinforcements in a polymer are discussed in the following section.

2.6. Dispersion of Nanoreinforcements

Achieving uniform and homogenous dispersion (exfoliated state) of nanoreinforcements is vital for the success of polymer nanocomposites [98]. Nanomaterials possess a high surface energy per unit area. As a result, they tend to form agglomerates to minimize this energy. This makes it difficult to maintain their nanoscale effective dimensions and disperse in to a polymer matrix. Dispersion of nanoreinforcements into the molten polymer depends on factors such as viscosity of the melt, wettability of the reinforcement, energy imparted through the mixing process (in breaking agglomerates), and efficiency of the mixing process. Dispersion methods can be broadly categorized in to mechanical and chemical based.

Several dispersion methods were investigated under the mechanical based category. Some are listed here: melt compounding [99, 100], masterbatch processing [101], ultrasound-assisted compounding [102], chaotic advection blending [103], Solid-State Shear Pulverization (SSSP) [104, 105], Solid State Ball Milling (SSBM) [105], and acoustic mixing [106]. These techniques can be grouped under one of the following categories: melt mixing and solid state mixing.

Melt compounding is the most commonly employed technique for dispersing nanoreinforcements in thermoplastic polymers. Nanoreinforcements were dispersed into the molten polymer, through the mixing action of a single or twin-screw extruder. Twin-screw compounding and ultrasound-assisted twin-screw compounding are discussed later separately. Solid state shear pulverization (SSSP) is another mechanical mixing technique, developed for blending immiscible polymers. Wakabayashi *et al.* [104] have advanced the SSSP process to produce polypropylene (PP) – graphite nanocomposites. In part of the process, both the polymer and the nanoparticle (graphite) were pulverized using a twin-screw pulverizer and the powders were later consolidated using single-screw extrusion. Some other techniques mentioned above involve solid state mixing; they are SSBM, and acoustic mixing. In solid state ball milling, nanoparticles and the polymer

mixture are milled to fine powders and then used as an input for the secondary process. Acoustic mixing is based on the generation of a uniform shear field throughout the mixing chamber for high efficiency mixing. Distortion of the nanoplatelets during the screw mixing processes is of concern as that can reduce their effectiveness.

A chemical approach to prevent agglomeration is to modify the surface (functionalize) of the nanoparticle, which helps in reducing the surface energy, changes their polarity, and prevents sticking [107]. Through functionalization, the nanoparticle surface is covered [108] or attached with ions or molecules (surfactants) that are compatible with a specific polymer. As every polymer has a different chemistry and structure, choosing the right functionalization is important.

Additionally, there are solvent mixing techniques such as sol-gel processing [26], solution mixing [109], sonication, shear mixing, and high speed mixing [110]. These techniques are mainly useful for working with thermosetting resins and low temperature thermoplastics. They are mainly batch wise processing and pose handling and consistency issues for large scale processing.

2.6.1. Twin-screw Compounding

In a twin-screw extruder, the polymer melts between two rotating screws and the housing by undergoing shear deformation. As the nanoplatelets are bound with Van der Waals forces (the availability of a larger surface area on the platelets make these week forces significant), they can be separated by the application of shear forces during mixing. Shearing and mixing of the reinforcements and the polymer melt can be achieved through large L/D ratio's (length to diameter of the mixing screw) and by application of different screw elements. Taking advantage of this, twin-screws have been used for decades in compounding. Since their inception into polymer processing, different types of twin-screw extruders have been developed. Basic differences are based on the shape and direction of screw rotation. There are co-rotating, counter-rotating, and intermeshing screws. In order to increase the efficiency of mixing, segmented

screws with different replaceable elements (e.g. kneading elements) have also been developed. Liu *et al.* [111] have investigated the effect of the type of screw rotation on the dispersion of nanoplatelets in to polyamide matrix. They found that nanocomposites show similar performance irrespective of the type of screw rotation, but using counter-rotating screws showed better dispersion. In their flow comparison CFD analysis for different screw rotations with the same geometry, Shah *et al.* [112] found that the flow velocity in a co-rotating screw is higher at the screw tip. This corresponds to a higher shearing rate and is considered good for mixing.

The melt compounding method is the most convenient and industrially promising process to produce polymer nanocomposites [100]. Masterbatch mixing is a multi-stage approach, where already mixed polymer-nanoreinforcement pellets are melted again and mixed at the same or reduced loading rate. The concept of a masterbatch is not new in the field of polymer processing; they are used commonly for adding specialized additives or dyes during primary processes such as injection molding and extrusion. Masterbatch pellets are prepared using the same or a compatible base resin and the additive at high loading rates. In their study of HDPE-Expanded graphite nanocomposites, Li *et al.* [101] found that nanocomposites from the master-batch process were superior to those obtained by melt processing. Having the secondary mixing helped in improving the performance of the nanocomposites through increased dispersion.

2.6.2. Ultrasound-assisted Compounding

In case of the ultrasound-assisted extrusion, along with twin-screw mixing, additional energy is applied in the form of ultrasound waves. The application of ultrasound waves for mixing is relatively well-known in the field of chemistry. Ultrasound energy is used for making thermodynamically unstable emulsions [113] and as an initiator for polymerization reactions [114]. In the past few years, researchers exploring for new techniques to improve nanoparticle dispersion have combined ultrasound with twin-screw extrusion [102, 115-117]. Ultrasound

energy applied to the polymer–nanoparticle mixture will lead to cavitation, due to the development of a high temperature zone locally. As the bubbles grow, they help in breaking and separating the nanoparticles into the polymer matrix.

2.6.3. Dispersion of Graphene

Dispersing single layer graphene into a polymer has intrigued researchers for quite some time [118]. Wang *et al.* [70] studied the wettability and adhesion energy of graphene, graphene oxide, and graphite with respect to solvents with different polarity (water, ethylene glycol, etc.). They found graphene is difficult to wet and exhibits lower adhesion energy compared to graphite and graphene oxide. In order to improve the adhesion and reactivity of graphene for certain applications, functionalization of graphene has been studied [119-123]. Graphene sheets can be functionalized on both surfaces. Functionalized graphene is especially useful for bio-sensing applications. Nair *et al.* [120] have studied the effect of fluorination on graphene sheets, the resulting fluorographene is an insulator, with similar thermal and mechanical behavior as that of graphene.

Solvent dispersion of graphene gained much attention through successful dispersion of graphene in organic solvent N-Methyl-2-pyrrolidone (NMP) [124-126]. Hernandez *et al*. [124] studied the effectiveness of different solvents in exfoliation of graphene through sonication. Khan *et al.* [127] proposed a method for the size selection of the dispersed graphene. Istrate *et al.* [128] have exfoliated graphene in NMP and used the filtered powder for the preparation of polymer nanocomposites. However, due to the high boiling point of NMP and its corrosive nature, it is difficult to work with. Buzaglo *et al.* [129] showed that graphene can be dispersed in water at high concentrations (0.7 mg/ml) by using surfactants (Triton X-100) and a combination of low power and high power sonication. As graphene is hydrophobic, application of a dispersant with hydrophobic and hydrophilic ends will help in stabilizing the dispersion in an aqueous solvent.

Strong π-π interaction between the benzene ring in the surfactant (Triton X-100) and the aromatic structure of graphene sheets aid in the dispersion. Interaction between graphene and aromatic compounds is well documented in the literature [130, 131]. Aqueous dispersed graphene obtained through a size selective approach (selecting uniform diameter graphene through centrifuge) appears to be a promising direction for the preparation of polymer nanocomposites. Nevertheless, the cost and complexity of the approach may limit this route for commercial applications.

In their work, Wang *et al.* [70] found that the wettability and work of adhesion of graphene is higher with Ethylene Glycol (EG) compared to water. Furthermore, Konios *et al.* [132] observed that reduced graphene oxide can be well dispersed in Ethylene Glycol, due to the presence of oxygen-containing functional groups. Ethylene Glycol being one of the raw materials for the polymerization of PET makes solution dispersion a reasonable route for the development of nanocomposites.

2.7. PET Nanocomposites

As stated earlier, PET nanocomposites are being pursued with the intention of improving their properties and expanding to new applications. Currently, other nanomaterials are already used and dispersed in the polymerization of PET. For example, carbon black nanoparticles of average diameter 400 nm, shown in Figure 6, are used (at 6 ppm or 0.0006%) for improving the heat absorption capacity of PET. Carbon black dispersion achieved through *in-situ* polymerization, offers the energy savings even at this low 6 ppm loading. Investigating nanocomposite preparation through the *in-situ* approach, at a more significant weight fraction can help in understanding the effectiveness of this approach.

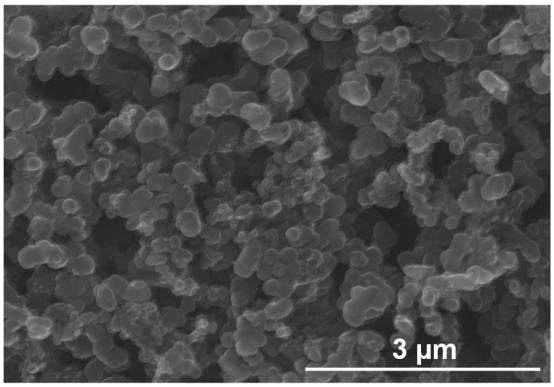

Figure 6: SEM micrograph of carbon black nanoparticles used for reheat performance of PET.

PET nanocomposites using different reinforcements were studied previously. A brief review of the prior work on PET nanocomposites and various mixing approaches used for dispersion are presented in Table 4.

Table 4: List of PET Nanocomposites studies reported.

Sl. No	Mixing Technique	Nanoparticle	Properties Studied	Reference
1	Melt blending	Carbon black	Thermal	[133]
2	Melt blending	MMT	Thermal and Permeability	[134]
3	Melt blending	MMT	Viscosity and Molecular weight	[135]
4	Mechanical mixing and Extrusion blending	MMT, TiO_2, SiO_2	Mechanical	[136]
5	*in-situ* Polymerization	MWNT's	Mechanical	[137]
6	Melt Compounding	SWNT's	Mechanical	[138]
7	-	CNF's	Mechanical	[139]
8	Master batch approach	Alumina	Crystallization	[140, 141]
9	*in-situ* polymerization	C_{12}PPh – MMT	Mechanical	[142]

10	*in-situ* polymerization	Attapulgite (AT)	Mechanical	[143]
11	Melt Blending	ZrP and ZrPP	Mechanical	[144]
12	Melt Compounding and Compression Molding	Graphene	Electrical	[145]
13	Melt Compounding and Compression Molding	Exfoliated Graphite	Electrical, Thermal and Dynamic Mechanical	[146]
14	Melt Compounding	Silica	Surface roughness and Optical	[28]
15	*in-situ* polymerization	Layered Double Hydroxide (LDH)	Thermal	[147]
16	*in-situ* polymerization	MMT	Mechanical	[148]
17	*in-situ* polymerization	$BaSO_4$	-	[149]
18	*in-situ* polymerization	MWNT's, (pristine, acid, diamine treated)	Mechanical and Rheological	[150]
19	*in-situ* polymerization	Antimoney doped TiO_2	Thermal	[151]
20	*in-situ* polymerization	Boehmite (AlOOH)	Thermal and Fire stability	[27]
21	*in-situ* polymerization	Fibrous Silica	Thermal	[152]
22	*in-situ* polymerization	SiO_2	Thermal	[153]
23	Solution Mixing	SiO_2 – PS	Water absorption and Thermal	[109]
24	Sol-Gel processing	SiO_2	Crystallization, Fire retardation	[26]
25	*in-situ* polymerization (Polycondensation)	MMT	-	[154]
26	*in-situ* polymerization	MMT	-	[155]
27	*in-situ* polymerization	MMT	Crystallization Kinetics	[29]
28	Melt-compounding	MWNT's	Mechanical and Thermal	[156]
29	Melt-Extrusion, Compression molded	MMT	Thermal	[157]

30	Melt-blending	MMT	Barrier, Mechanical and Thermal	[24]
31	Melt-blending	MMT	Thermal Stability	[99]
32	Solution Mixing	MMT	Thermal	[158]
33	Melt-intercalation	MMT, Grafted Styrene	Impact Behavior	[159]
34	Melt-compounded, Injection molded	$BaSO_4$	Crystallization Kinetics, Thermal	[160]
35	*in-situ* polymerization	POSS	Mechanical, Rheological, Thermal	[161]
36	Melt-compounding and *in-situ* polymerization	POSS	Mechanical, Thermal	[162]
37	Melt-compounding and in-situ polymerization	POSS	Mechanical, Thermal	[163]
38	Melt-compounding	MMT	Permeability	[164]
39	*in-situ* Polycondensation	GO-catalyst	Electrical, Thermal	[165]
40	Melt-compounding	Graphene platelets	Barrier	[166]
41	Melt-compounding	xGnP, MWCNT	Crystallization	[167]
42	Melt-compounding	Clay	Mechanical, Thermal	[168]
43	Melt-compounding	GNP and GIC	Electrical, Thermal and Flexural	[169]
44	*in-situ* Polymerization	EG	Electrical	[37]
45	Solution dispersion and Melt-compounding	EG	Mechanical	[128]

High melting temperature and melt viscosity of PET make melt-compounding a relevant technique for the preparation of nanocomposites. Envisioned in 2007, our group was the first to make PET-graphene nanocomposites. Through our work and now others, the addition of graphene has already been shown to improve the mechanical, barrier, thermal, and conductive properties. However, there is further scope for improving the dispersion of graphene and understanding the strengthening mechanisms at high loadings. This can lead to new applications

such as strain monitoring, electromagnetic shielding, lightning strike protection, and reduced moisture absorption [63]. Graphene combined with thermoplastic polymers add flexibility to the choice of processing methods, expanding the range of applications. The development of hybrid nanocomposites with multiple nanoreinforcements or polymer blends (PET-PP/GNP nanocomposites [38, 170]) may also be a promising approach.

CHAPTER III

EXPERIMENTAL DETAILS

3.1. Materials

3.1.1. Poly(ethylene terephthalate)

Commercially available poly(ethylene terephthalate) (PET) of molecular weight M_w – 84100 g/mol (0.81 dl/g intrinsic viscosity (I.V.)) from Leading Synthetics, Australia (oZpet™ GG-2180 non-fast reheat heat resin) was used in this work. As received PET pellets are semi-crystalline, verified using differential scanning calorimetry (DSC). PET is hygroscopic; the presence of moisture in the polymer melt will lead to a loss of molecular weight through chain scission (hydrolysis of ester bonds). Therefore, PET was dried for 4-6 hours at 170°C before each process, to minimize polymer degradation.

3.1.2. Graphene Nanoplatelets

Commercially available graphene nanoplatelets (GNPs) of two different average surface areas, obtained from XG Sciences Inc., USA, were used in this study. Graphene nanoplatelets (GNPs) with an average diameter of 5 μm, thickness around 6 to 8 nm and an average surface area of 120-150 m^2/g, (xGnP®-M-5 grade) [34], were used in the preparation of nanocomposites. In addition, nanoplatelets with an average diameter of 2 μm, average surface area of 750 m^2/g (xGnP®-C-750 grade) [171] were used only for the *in-situ* polymerization studies. Nanoplatelets were received in dry agglomerated powder form. Each agglomerated platelet consists of several

nanoplatelets, as seen from Figure 7(b). Also from the SEM micrograph, it was observed that the nanoplatelets are not uniform across the length and have zig-zag edges. Chemical structure of the nanoplatelets is shown in Figure 8. Nanoplatelets comprise of 99.5% carbon with very low oxygen and hydrogen, present in the form of carboxyl and hydroxyl groups on the edges formed due to the exposure of raw carbon during the fracture of platelets. These nanoplatelets were prepared based on the procedure developed by Fukushima [52], where acid intercalated graphite flakes were expanded through microwave processing.

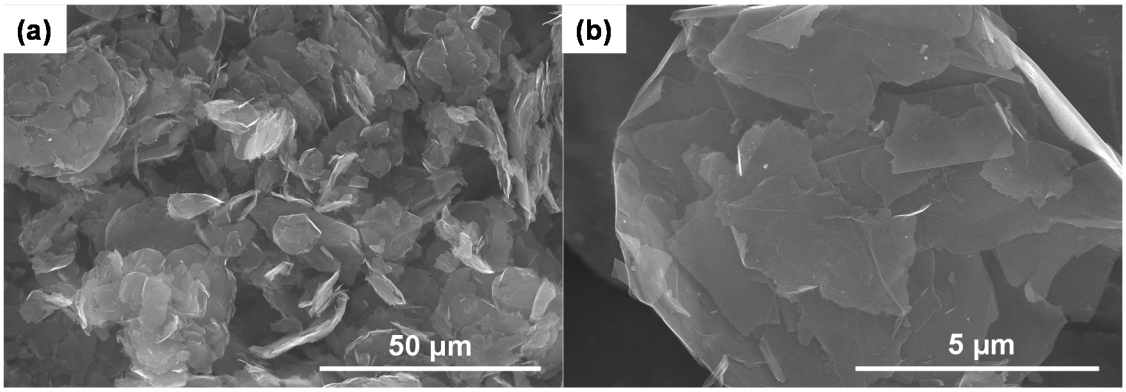

Figure 7: (a) SEM micrograph of the graphene nanoplatelets (xGnP®-M-5), (b) the presence of multiple nanoplatelets in the agglomerate [172].

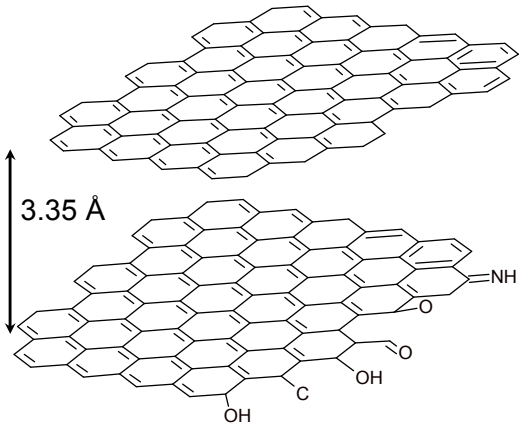

Figure 8: Chemical structure of xGnP [173].

3.2. Preparation of PET-GNP Nanocomposites

With the intention of dispersing graphene nanoplatelets in to the PET matrix without forming agglomerates, a two-step approach was considered here. In the first step, PET-Graphene masterbatches were compounded through twin-screw and ultrasound-assisted twin-screw processing. In the second step, nanocomposite masterbatches were injection molded to different final nanoplatelet loading fractions and their microstructural, mechanical and thermal characteristics were investigated.

3.3. Masterbatch Processing

In the current investigation, PET-graphene masterbatches were processed using two different techniques. Details on the processing equipment and compounding are presented below. Compounded material was pelletized for further processing; size and dimensions of the pelletized masterbatch are presented in Table 5.

Table 5: Properties of PET and masterbatch pellets.

Pellet Type	Height (mm)	Major Diameter (mm)	Minor Diameter (mm)	Weight (g)
PET	2.35	3.42	2.64	0.02
Twin-screw processed	3.17	2.46	2.15	0.015
Ultrasonic Processed	1.9	1.09	0.96	0.002

3.3.1. Twin-screw Compounding

In the current work, graphene nanoplatelets (GNPs) and PET resin were compounded into PET-xGnP masterbatch pellets using a Krauss Maffei ZE-25 UTX laboratory extruder (co-rotating) at Ovation Polymers, Medina, OH (ExTima™ technology). Two different sets of masterbatch

pellets at 2%, 5%, 10% and 15% weight fraction were compounded using this process. In each set, 5.4 kgs (12 lbs) of masterbatch was prepared for each of the weight fractions.

3.3.2. Ultrasound-assisted Twin-screw Compounding

PET-graphene nanoplatelets were processed using the ultrasound-assisted twin-screw extrusion system developed at the University of Akron [116]. PET pellets were dried overnight in oven at 80^{o}C to remove moisture and then compounded with graphene nanoplatelets at 5% weight fraction. PET and graphene nanoplatelets were compounded using a co-rotating twin-screw micro-compounder (PRISM USALAB16) equipped with an ultrasound horn (Branson Ultrasonics Corp., USA) operating at 40 kHz. The ultrasound horn was positioned in the barrel region at a distance of 14.5 cm from the die entrance. A schematic of the combined system is shown in Figure 9. Vertical position of the horn tip was adjusted such that it is in contact with the polymer melt. A flow rate of 0.9 kg/hr (2 lbs/hr) was maintained throughout the process, with a set screw speed of 200 RPM. The residence time in the ultrasound treatment zone was 9.2 s.

Combined with the baseline composite masterbatch, a total of four sets of masterbatches were prepared including different ultrasound amplitudes: no ultrasound (0 USM), 3.5 μm (3.5 USM), 5 μm (5 USM), and 7.5 μm (7.5 USM). Further, to understand the effect of ultrasound treatment on PET alone, pure PET (no reinforcement) was also processed under the same conditions.

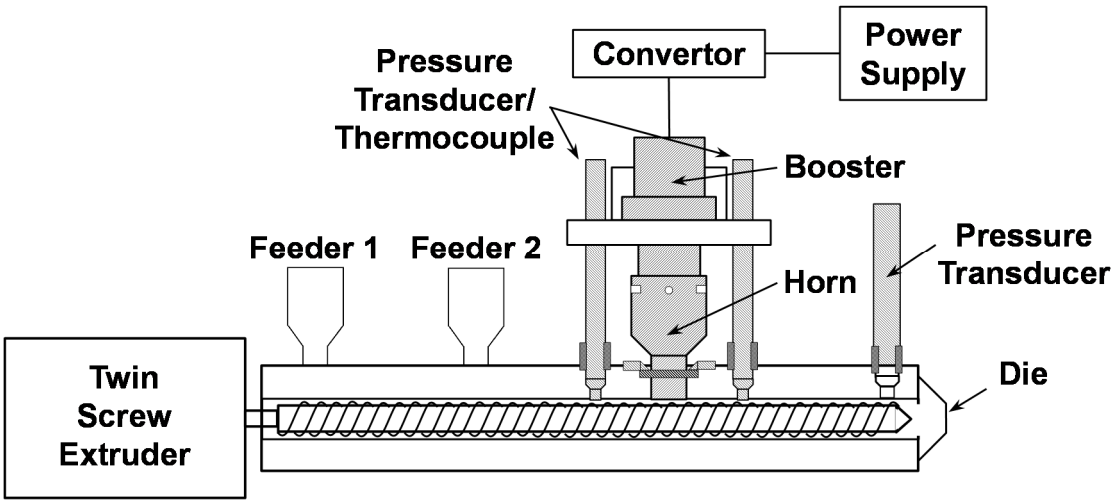

Figure 9: Schematic of the Ultrasound assisted twin-screw extrusion system used [116].

3.4. *In-situ* Polymerization

In-situ polymerization is another commonly employed approach for the preparation of polymer nanocomposites. In general, *in-situ* polymerization consists of two steps. The first step is intercalating nanoscale reinforcements in the solution phase using compatible polymer precursors or solvents. In the second step, polymerization is undertaken using the nanoplatelet intercalated solution. Dispersing the nanoplatelets in to a chemically compatible and low viscosity material is considered to be more efficient compared to direct mixing with high viscous polymer melt.

In this work, Ethylene Glycol (EG), one of the raw materials for the polymerization of polyethylene terephthalate was used as the solvent for dispersing graphene nanoplatelets. Ethylene glycol of reagent grade, with 99% purity obtained from Sigma Aldrich Corp. was used in this work. Graphene nanoplatelets were added to EG at 1 mg/ml concentration (0.1% weight fraction) and sonicated using a 40 kHz bath sonicator, CPX8800H model by Branson Ultrasonics Corp., USA. EG-GNP solutions were sonicated for 106 hours to ensure a homogenous dispersion, as depicted in Figure 10. During the sonication process, solution beakers were

covered with aluminum foil to prevent exposure to atmospheric oxygen. Dispersions were prepared using both low (120 m^2/g) and high (750 m^2/g) surface area graphene nanoplatelets.

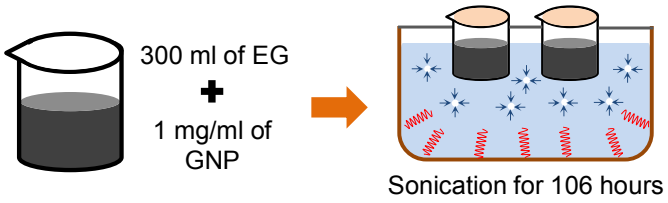

Figure 10: Ethylene glycol-graphene nanoplatelets dispersion preparation process.

In-situ polymerization of graphene nanoplatelets dispersed ethylene glycol and dimethyl terephthalate was attempted using a 1 kg polymerization reactor, available at Auriga Polymers Inc., USA. PET polymerization takes place through a two-step reaction. The first step is called the ester interchange reaction, where the monomer is formed. In the latter step, the polymer is formed through a condensation reaction. Experimental setups used along with the undergoing reaction at each step are detailed in the following paragraphs.

3.4.1. Ester Interchange Step

A schematic of the reactor and methanol collection setup is show in Figure 11. Dimethyl terephthalate (DMT), available from Auriga Polymers Inc. was used for the polymerization. EG with dispersed GNPs and the powdered DMT were charged in to the reactor under nitrogen purge at a 2.3:1 moles ratio, with excess of EG. The catalysts for ester interchange reaction, Manganese acetate ($Mn(CH_3COO)_2$), and for condensation reaction Antimony trioxide (Sb_2O_3), were added to the batch at 82 ppm and 300 ppm respectively, and heated to 175°C under constant stirring. As the batch temperature reached about 170°C, methanol collection began indicating that the EI reaction has started and then the nitrogen purge was closed. There onwards the batch temperature was increased in steps of 15°C till it reached 235°C. As the reaction progressed, the inside temperature of the gooseneck increased from room temperature to above 60°C. Once the

methanol collected reached the theoretical yield, 300 ml in this case, and the gooseneck temperature dropped to below 60°C, the ester interchange was considered finished. The gooseneck was removed and Polyphosphoric acid (H_3PO_4) was added at 38 ppm to the batch to terminate the EI reaction. PET monomer formation through the ester interchange between DMT and EG is illustrated in Figure 12. The entire EI reaction took around 3 hours to finish.

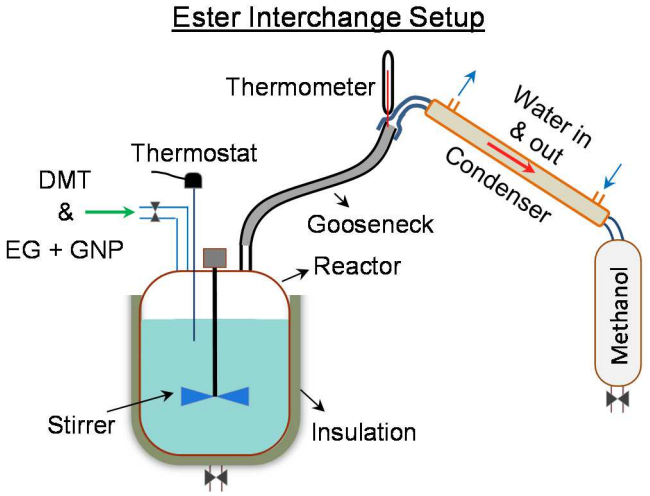

Figure 11: Schematic of the reactor setup for the ester interchange step.

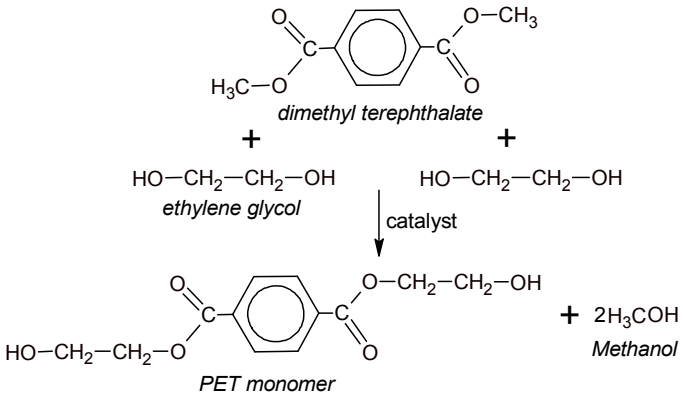

Figure 12: Ester interchange reaction between DMT and EG to form the PET monomer.

3.4.2. Polycondensation step

The reactor and excess EG collection condenser setup used for the condensation step is shown in Figure 13. During the condensation step, the reactor temperature was increased to 285^{o}C and kept under vacuum (30 in Hg) until PET of desired viscosity was achieved. Isophthalic acid ($C_6H_4(COH)_2$) and stabilized cobalt were added at 20 grams and 65 ppm respectively to the batch at the beginning of the condensation reaction. Isophthalic acid will limit the crystallinity of PET, therefore making it easy to process. Cobalt was added to control the color of final PET. As the condensation reaction progresses, the molecular weight of PET increases and EG will be released, as shown in Figure 14. Excess EG was collected in to a round flask and solidified using dry ice to prevent flowing into the vacuum pump. Change in the viscosity of the batch with increasing PET chain length will affect the stirring current. As the reaction progressed, the stirrer current was monitored for change in amperes at 15 minute intervals. The reaction was stopped by cutting the vacuum when there was no change in the stirrer current for two consecutive readings. At this stage, the polymer melt obtained was extruded from the opening at the bottom of the reactor in to an ice water bath and pelletized using a strand chopper.

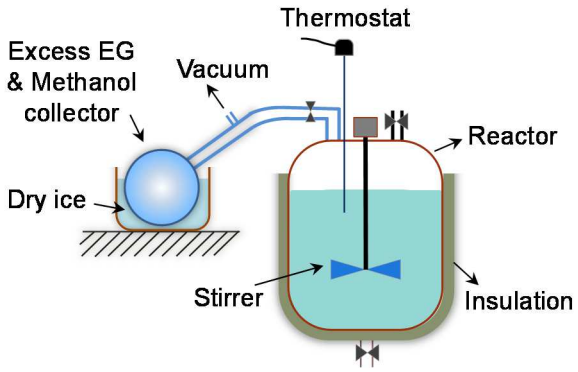

Figure 13: Schematic of the setup used for polycondensation.

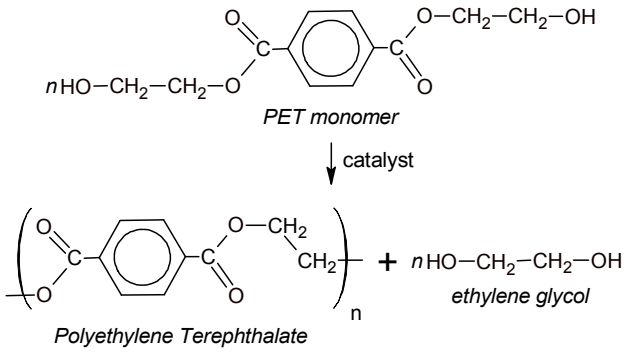

Figure 14: Formation of PET polymer chain from monomer.

Including a control batch (no graphene nanoplatelets), a total of three batch polymerizations were accomplished and the reaction times for each material are listed in Table 6. The quantity of the polymer pellets yield varied because of issues related to the extrusion process.

Table 6: Reaction times and methanol yield for respective polymerization batches.

Material	E.I. Duration (min)	Methanol Yield (ml)	P.C. Duration (min)	Polymer Yield (g)
PET	180	310	135	160
PET + 0.1% GNP (750 m^2/g)	188	310	105	380
PET + 0.1% GNP (120 m^2/g)	192	324	112	190

3.5. Injection Molding of Nanocomposites

With the objective of testing amorphous nanocomposites, injection molding was selected in this study. Three different injection molding presses (oil cooled, water cooled and a micro injection molder) were used in this work. PET-graphene nanoplatelet masterbatches obtained from the compounding process were used for molding nanocomposites at different loading fractions. The laboratory injection molding unit (oil cooled) available from Ovation Polymers, was used for molding nanocomposites at 2%, 5%, 10% and 15% GNP weight fractions from masterbatches (compounded pellets were injection molded with no dilution of graphene concentration using pure PET). Tensile bars were molded with barrel temperatures in the range of 260^{o}C to 280^{o}C. A standard tensile bar mold, following ASTM D 638 type I specifications, was used.

Signs of crystallization (an opaque core) were observed in the injection molded PET, due to the slow rate of cooling. Therefore, further experimentation was performed on an injection unit designed for PET. This machine was manufactured by Husky Injection Molding Systems, Inc., Canada and is a relatively smaller scale unit used for prototyping in industry. Injection molding was performed offsite at a Niagara Bottling LLC facility in Ontario, CA. The HyPET 90 RS45/38 injection molding system has a 90 ton clamping force and is equipped with a screw of 38 mm diameter and a chilled water cooled mold. This allows processing of PET at higher cooling rates (low cooling time) to retain the amorphous microstructure.

In order to keep the injection molding of the nanocomposite close to that of the process used for PET in industry, a custom mold was developed. The tube specimen prepared using the custom mold, shown in Figure 15, is designed for ease of mechanical testing. Care was taken in the design of the mold to have a large gauge length with uniform cross-section. This mold makes parts with a relevant size and processing window (injection pressures and cycle time) typical to industrial scale parts.

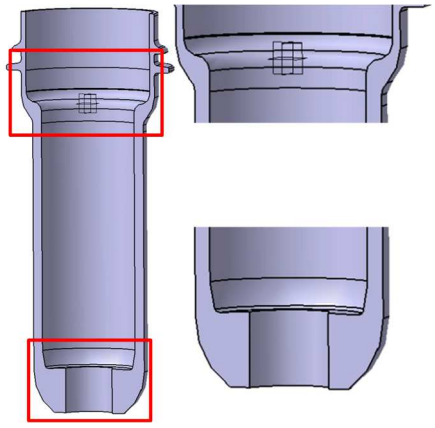

Figure 15: Cross-sectional views of the injection molding compatible tensile specimen, design features that allow gripping during the test are highlighted.

Using the nanocomposite pellets obtained from the aforementioned methods, samples for mechanical testing were injection molded at different GNP concentrations. Aimed at testing nanocomposites with low GNP weight fractions, the masterbatch was diluted by mixing with PET and injection molded into nanocomposites with as low as 0.5% weight fraction. Final weight fractions of the nanocomposites were verified by measuring the percentage of pellets in the images collected from feed throat, as shown in Figure 16. Using the pellets dimensions listed in Table 5, the actual weight fractions were calculated. Nanocomposites from each process run were collected for characterization studies, after the process was stabilized. Stabilization occurs when injection pressures and cycle time are steady for more than 10 min.

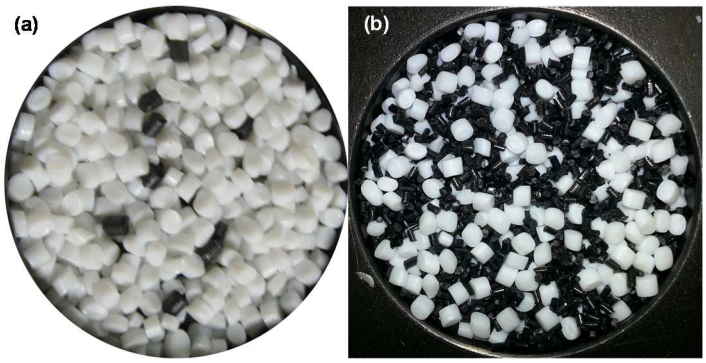

Figure 16: PET and masterbatch pellets mixture from feed throat (a) 0.6% loading from Set B processing [174]and (b) for 0 USM ultrasound treated batch.

Details on the injection molded nanocomposite weight fractions and the respective masterbatch used are presented in Table 7. They are grouped into different sets for the purpose of comparison.

Table 7: Details of the PET nanocomposite samples obtained from injection molding.

Set	Mixing Approach	Cooling Medium	Masterbatch Weight Fraction	Final Weight Fractions	Sample Type
A	Twin-screw mixing	Oil	2%, 5% , 10%, & 15%	2%, 5% , 10%, & 15%	ASTM bar
B	Twin-screw mixing	Water	10%	0.6% & 1.2%	Tube
C	Twin-screw Mixing	Water	2%	0.5%	Tube
C	Twin-screw Mixing	Water	15%	2%	Tube
U	Ultrasonic assisted Twin-screw mixing	Water	5%	2%	Tube

Process Optimization

Polymer processing through injection molding is dependent on several variables including: barrel temperatures, injection pressure, hold and back pressures, fill time, and cooling time. Balancing

all these variables is necessary to have a part free of crystallinity and defects such as voids. At the start of each process run, the barrel was flushed with baseline material to remove the residual material from previous tests. This allows starting the processing with known conditions and optimizing them as the PET-masterbatch mixture occupies the barrel. Normally this will take up to 200 shots, with two samples for each shot.

Table 8: Comparison of process pressures between PET and nanocomposites from ultrasound treated masterbatches.

Description	Nanocomposite Weight Fraction	Fill Pressure (PSI)	Hold Pressure (PSI)	Back Pressure (PSI)
PET	-	604	580	150
0 USM	2%	459	580	150
3.5 USM	2%	472	580	150
5 USM	2%	480	580	150
7.5 USM	2%	482	580	145

The addition of graphene nanoplatelets affects the melt viscosity of PET, this will reflect on the fill pressures. It was observed that the maximum fill pressure decreased when processing the ultrasound masterbatch (as shown in Table 8); while the hold pressure was the same. The hold pressure is important for keeping the mold closed as the material solidifies. Another important process variable is back pressure, this helps in homogenizing the material and removing voids from the melt [175]. Effectiveness of the process and mixing of PET and the masterbatch inside the barrel can be checked through visual inspection for samples with lower GNP weight fraction; dark spots, marks, and flow streaks shown in Figure 17, observed during the initial injection cycles.

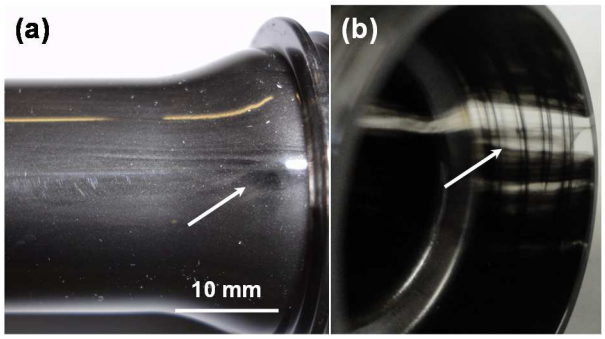

Figure 17: Visual signs for poor mixing as observed for 0.5% GNP nanocomposites.

3.5.1. Micro Injection Molding

In the process of dispersing graphene nanoplatelets in to PET, PET along with GNPs was exposed to ultrasound and twin-screw mixing. With the purpose of understanding the effect of ultrasound treatment on PET mechanical properties and evaluating the improvement from graphene dispersion through ultrasound without dilution, tensile samples were prepared using a micro injection molding system developed by Xplore Instruments BV, Netherlands. A 5.5 cc capacity micro injection molding unit in combination with a 5 cc micro compounding unit, shown in Figure 18 was used for the preparation of tensile bars, shown in Figure 19(b). The micro-compounder unit equipped with a co-rotating twin screw was used to melt the pellets and provide a homogenous melt mixture. Using the transfer device shown in Figure 18(b), the polymer or the nanocomposite melt was transferred from the compounder on to the injection molder. On the injection molder, material was injected into the conical mold by a plunger connected to high pressure air (at 13.8 bar). The micro-injection system provides control of the mold temperature, injection pressure, hold pressure, injection time, and hold time.

A dual dog bone mold was designed according to the ASTM D 638 Type V specimen L/D ratio for the gauge section, with a fill volume of 2.1 cc. During the compounding process, material was heated to 270^{o}C and homogenized by opening the recirculation valve for 1 min, after which the melt was collected into the transfer device. Tensile bars were made using an aluminum mold

at room temperature. The relatively large volume of the aluminum mold acts as a heat sink and allowed for cooling of the polymer melt during injection. The injection process parameters used for making PET and nanocomposite tensile bars are listed in Table 9.

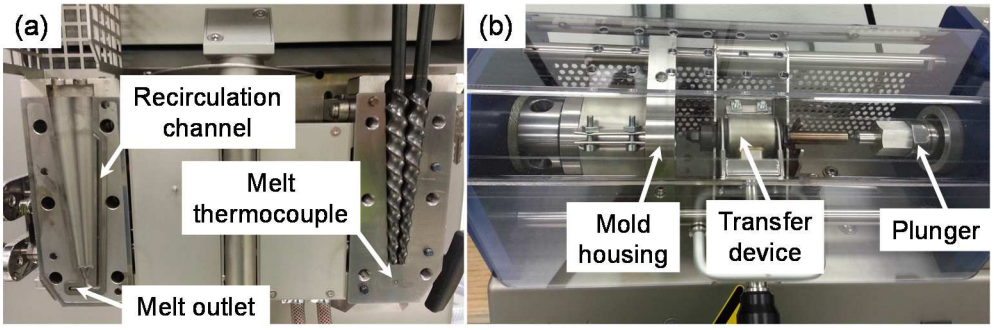

Figure 18: (a) Micro compounder with co-rotating twin screw and (b) Micro injection molding system and transfer device.

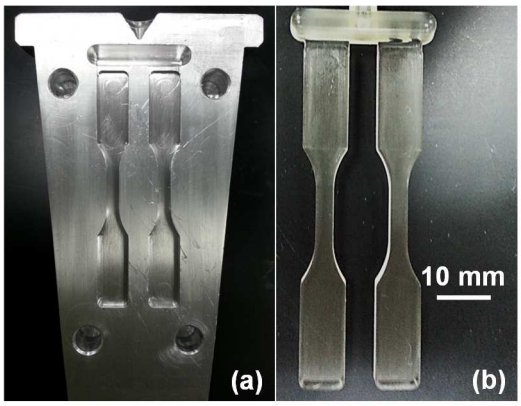

Figure 19: (a) Dual dog bone mold used for making tensile samples and (b) molded PET tensile bars.

Table 9: Process parameters for tensile bars made using the micro-injection molding system.

Mold Temperature	Injection Pressure	Injection Time	Hold Pressure	Hold Time
25°C	5 bar	1 sec	6 bar	3 sec

In total, five different material sets: PET control, ultrasound treated PET, nanocomposites pellets with 5% GNP weight fraction from twin-screw mixing, ultrasound assisted twin-screw mixing, and materials from *in-situ* polymerization, were processed using the micro compounding system and tensile bars were obtained for mechanical testing. In the case of nanocomposites, different mixing time periods were also investigated to understand the effect of mixing time on the nanocomposite properties. Nanocomposites tensile bars with different graphene weight fractions were also obtained using the micro-injection molding system. All the materials were dried in small quantities (30 grams) at 170°C for 2 hours in an oven before processing to avoid degradation due to the presence of moisture or a drop in viscosity from over drying.

3.6. Characterization of Nanocomposites

3.6.1. Density Measurement

Comparison of the densities between the injection molded nanocomposites will help in identifying the difference in the samples due to process defects (e.g., voids). Relative densities can be determined based on Archimedes' principle, using the following equation:

$$\rho = \frac{m}{m - \overline{m}} \times \rho_o \tag{1}$$

Where, m is the mass of the sample in air, $\overline{m}$ is the mass of the sample in liquid medium, and ρ_o is the density of the medium used (water).

Amorphous PET has a density of 1335 kg/m^3 [48]. PET a semi-crystalline polymer, exhibits a range of densities based on crystallinity [176]. The theoretical density of the amorphous nanocomposite can be calculated using the relative density of PET (1335 kg/m^3) and GNPs (2200 kg/m^3). Crystallinity of the control (PET) and nanocomposite samples can be evaluated using the equation given below.

$$X_c = \left(\frac{\rho_c}{\rho_{sample}} \right) \times \frac{\left(\rho_{sample} - \rho_a \right)}{\left(\rho_c - \rho_a \right)} \quad (2)$$

Where, X_c is the crystallinity of the sample, ρ_a is the density for amorphous PET, ρ_a is the density for crystalline PET (1455 kg/m^3 [48]), and ρ_{sample} is the density of the composite.

3.6.2. Molecular Weight Analysis

PET is known to undergo chain scission under high shear at melt temperatures. Further, the effects of ultrasound treatment on PET have not been previously investigated. Therefore, to evaluate the change in molecular weight of the ultrasound treated PET and PET nanocomposite, Gel Permeation Chromatography (GPC) was performed. Hexafluoroisopropanol (HFIP) was used as the solvent for dissolving PET at room temperature. For the composite pellets, the nanoplatelets were filtered out after the polymer was dissolved. GPC measurements were performed at Auriga Polymers. Polymer dissolved in the solvent (5 mg/ml) was pumped at a constant flow rate through a GPC column with specific pore sizes. The time taken by the polymer molecules in a swollen state to pass through the column (retention time) is based on the size of the molecules. While the polymer solution passes through the column, the elution volume for the different fractions (same molecular weight), identified using a refractive index detector, was recorded. Comparing this elution volume against Polystyrene standards of known molecular weight, the average molecular weight for PET samples was obtained.

3.6.3. Intrinsic Viscosity Measurement

Intrinsic viscosity (I.V.) of PET and ultrasound treated PET pellets was measured at the Auriga Polymer facility, using their proprietary solvents that were calibrated with respect to the solvents recommended in ASTM D4603 standard. After dissolving the polymer pellets in solvent, that solution was passed through a glass capillary viscometer and the flow time for the solution as it drops from the higher to lower calibration mark (as shown in Figure 20) was recorded. The ratio

of the average flow times for solution to the solvent gave the relative viscosity (η_r) of the polymer. Intrinsic viscosity of the polymer was calculated using the following equations [177]:

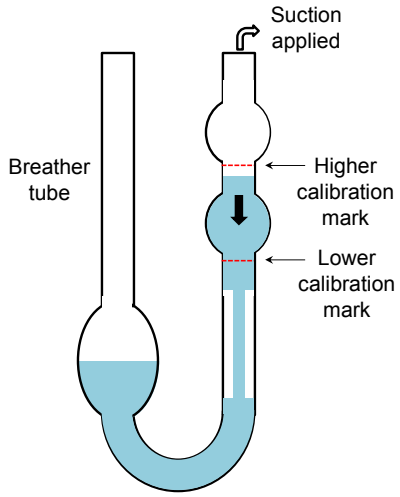

Figure 20: Schematic of the capillary viscometer.

$$\eta_r = t/t_o \tag{3}$$

$$\eta = 0.25(\eta_r - 1 + 3\ln\eta_r)/C \tag{4}$$

Where, η_r is the relative viscosity, t is the average solution flow time (s), t_o is the average solvent flow time (s), η is the intrinsic viscosity (dL/g), and C is the polymer solution concentration (g/dL).

Using the intrinsic viscosity (I.V.) data obtained by the abovementioned procedure and weight average molecular weight data from the GPC technique, Mark-Houwink parameters for relating PET I.V. to M_w were refined and used to calculate the viscosities for ultrasound treated nanocomposites.

$$[\eta] = KM^a \tag{5}$$

Where, η is polymer intrinsic viscosity (dL/g), M is the average molecular weight (g/mol), 'K' and 'a' are Mark-Houwink constants. While using weight average molecular weight, 'K' and 'a' are stated as 0.00047 and 0.68 [178].

3.6.4. Mechanical Properties

Nanocomposite samples with two different geometries were obtained from the injection molding process: tensile bars and tensile tubes. Both the geometries, tensile bars and tubes were tested using a universal materials tester[§] at a cross-head speed of 5 mm/min, following the ASTM D 638 standard. A non-contact Laser Extensometer[**] was used for recording strain. The laser extensometer records the displacement based on the reflections from self-reflective tape, used to mark the gauge length on the test samples (as shown in Figure 21 (a)). Strain values from the laser extensometer and load from the load cell were simultaneously recorded at an interval of 100 ms. For the purpose of testing the nanocomposite tubes, a custom fixture (shown in Figure 21 (b and c)) was used [19]. A minimum of 5 samples were tested for each process condition.

[§] Universal testing machine models 5582 and 8802, from Instron.
[**] Laser Extensometer model LE – 05, from Electronic Instrument Research.

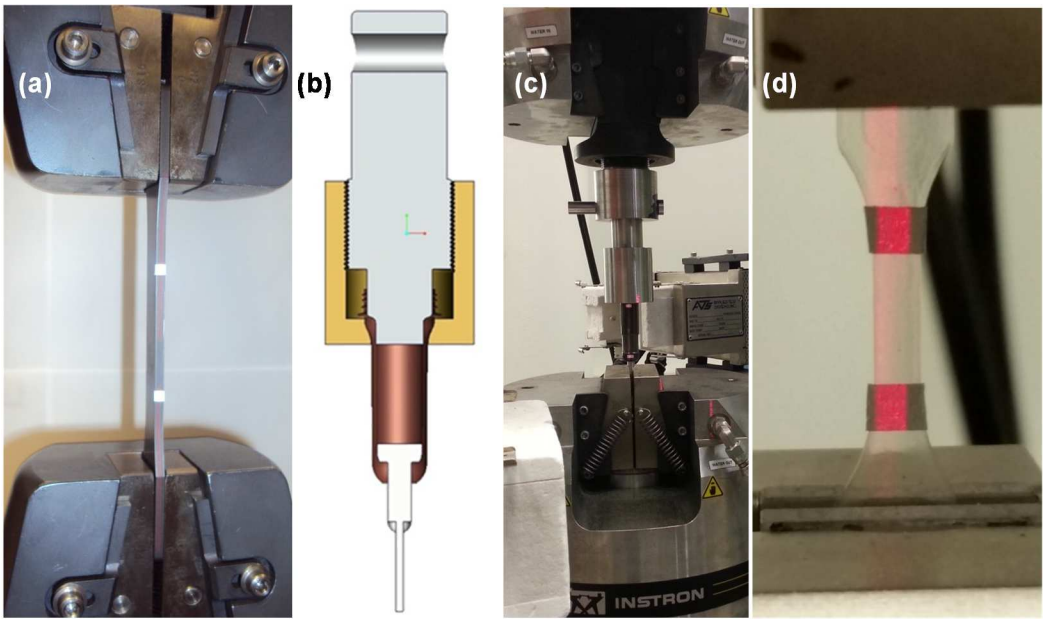

Figure 21: (a) Testing of nanocomposite tensile bar, (b) tube testing fixture, (c) tube testing and (d) testing of tensile bar from micro injection molding.

3.6.5. Thermal Analysis

Differential Scanning Calorimetry (DSC) of the PET and nanocomposite samples was performed to understand the effect of graphene on thermal properties (glass transition, crystallization and melt temperatures) of PET. Thermographs of nanocomposites were acquired using a differential scanning calorimeter[††]. Nanocomposite samples were heated from ambient temperature to 300°C at 10°C/min and held at 300°C for 1 min (first heating cycle), then cooled to 25°C at 10°C/min and held at 25°C for 1 min (first cooling cycle) and finally reheated to 300°C at 10°C/min (second heating cycle) under a nitrogen atmosphere. Ultrasound treated PET pellets were also analyzed for change in thermal properties.

From the first heating cycle, melting parameters (temperature, heat of fusion) and heat of crystallization were obtained for determining the crystallinity (X_c). Melt crystallization

[††]Q-2000 DSC from TA Instruments.

temperature (T_c) and on-set temperature (T_{on}) were obtained from the first cooling cycle, to determine the crystallization half-time ($t_{1/2}$). Crystallinity can be calculated using the below equation:

$$X_c = \left[\frac{\Delta H_f - \Delta H_{cc}}{\Delta H_c^o} \right] \times \left(\frac{1}{1 - w_f} \right) \times 100 \quad (6)$$

Where, ΔH_f is the heat of fusion, ΔH_{cc} is the heat of crystallization (cold crystallization), ΔH_c^o is the heat of fusion for 100% crystalline polymer, for PET – 140.1 J/g [179], and w_f is the weight fraction of the reinforcement phase in the nanocomposites.

Crystallization half-time was determined using the following equation:

$$t_{1/2} = \frac{(T_{on} - T_c)}{X} \quad (7)$$

Where, T_{on} is the crystallization on-set temperature, T_c is the crystallization temperature, and X is the rate of cooling (here, 10°C/min).

3.6.6. Rheological Properties

Polymer flow behavior is known to be affected by the addition of reinforcements (micro or nano) [180-182]. Studying the flow properties of the nanocomposites is useful for their processing.

Melt rheology was studied to understand the effect of graphene on the flow properties of PET. Rheographs for nanocomposite pellets were acquired using a rotational Rheometer[‡‡], equipped with a 25 mm diameter parallel plate geometry and electronically controlled heating. Samples were dried in an oven at 170°C for 12 hours to eliminate moisture. PET and nanocomposite pellets placed between parallel plates were melt-pressed to 1 mm thickness (as shown in Figure 22) at 260°C, under N_2 atmosphere. The linear viscoelastic region (region where material response is independent of the deformation amplitude) of the samples was determined by running

[‡‡] AR-2000ex Rheometer from TA Instruments

a strain sweep at a 1 Hz frequency. Dynamic frequency sweeps from 100 rad/s to 0.1 rad/s were acquired for all the samples at 1% strain rate, with in the linear viscoelastic region for PET.

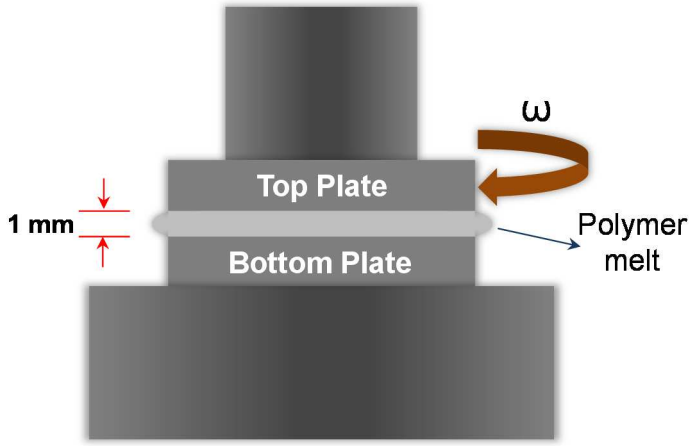

Figure 22: Schematic of the parallel plate geometry and polymer melt.

Dispersion of nanoparticles into the polymer matrix increases polymer chain entanglements through polymer-polymer and polymer-reinforcement interactions [180]. An increase in entanglements stiffens the polymer and exhibits a solid like (rigid) deformation behavior, which is independent of the test frequency. Transition of the nanocomposite to a rigid behavior occurs at a critical weight fraction (percolation threshold), when a connecting network of the reinforcement is formed. Dynamic frequency sweeps of moduli provides information from both the polymer and reinforcement phase. Where the high frequency moduli are dominated by the polymer matrix and the low frequency response of the material is dominated by the reinforcement. Therefore, the percolation volume fraction can be obtained based on the low frequency moduli of the nanocomposite. The average aspect ratio of the reinforcement at the percolation volume fraction can be determined using the following equation.

$$A_f = \frac{3\phi_{sphere}}{2\phi_{per}} \tag{8}$$

Where, ϕ_{sphere} is the percolation volume fraction for randomly packed overlapping spheres (0.30, [183]) and ϕ_{per} is the percolation volume fraction for nanocomposite.

3.6.7. Raman Spectroscopy

Raman spectroscopy is the most widely used technique for characterizing the quality of graphene. For nanocomposites, several studies have reported the application of Raman spectroscopy for characterizing the interaction between a polymer-graphene system and the quality of graphene. A characteristic Raman spectrum of single layer graphene will have peaks near 1580 cm^{-1} (G-band) corresponding to the C─C stretching of sp^2 carbon materials and near 2680 cm^{-1} (G'-band), is the corresponding higher order mode [184]. The presence of defects in graphene can give rise to a different Raman peak near 1350 cm^{-1} (D-band), which is useful in analyzing the quality of graphene. In case of multi-layer graphene, number of layers up to n=7 for multi-layer graphene can be estimated based on the intensity of G-band (~1580 cm^{-1}) and the shape of 2D-band or G'-band (~2680 cm^{-1}) can be used to identify up to n=4 layers [185]. In the current work, Raman spectroscopy was used to evaluate the dispersion of graphene nanoplatelets and also to ascertain the π-π interactions between graphene layers and the phenyl ring in the PET molecular chain. Interaction of PET phenyl ring with graphene is found to show a shift in the Raman band related to C─C stretching (1617 cm^{-1} [186]) of the phenyl ring [187].

Raman spectrum for PET and PET-GNP nanocomposites were collected using a 532 nm (green light) laser excitation, at 2 mW laser power, with a 20 μm spot size[§§]. Change in the C─C (1617 cm^{-1}) band position was evaluated by doing an individual peak fit (Gaussian fit) on the spectra collected for each GNP weight fraction.

[§§] WITec Instruments Corp., Germany.

3.7. Microstructure Analysis

Imaging nanocomposites is imperative to understand the role of nanoparticles in improving polymer properties. Nanoreinforcements are considered advantageous because of the large extent of interactions possible with the polymer matrix. Thus, it is necessary to visualize the extent of interactions, which depend on the level of dispersion. In addition, the actual microstructural information is beneficial to model the behavior of nanocomposites and help in engineering materials. Electron microscopy [188, 189] and X-Ray diffraction are the most common techniques used for studying dispersion. Both of these techniques are often used in support of each other.

3.7.1. Scanning Electron Microscopy

Graphene nanoplatelets inside the PET matrix were imaged by scanning electron microscopy[***]. SEM micrographs of the fracture surfaces of the PET, and PET-GNP nanocomposites were obtained. PET control and the nanocomposites with lower graphene content (up to 2%) were Au/Pt coated for 1 minute, using a Balzers Union MED 010 coater.

3.7.2. Ultrasound Imaging

Nanocomposite tensile bars were imaged with ultrasound to evaluate the presence of process defects (e.g. voids). Ultrasound 'Bulk Scans' for the nanocomposites were acquired using an acoustic microscope[†††]. Scanning was done at an ultrasound frequency of 30 MHz, with 0.5" focal length and a spot size of 122 μm. During the scanning process a liquid medium (water in the current study) was used between the probe and sample, to maximize the ultrasound transmission. Ultrasound micrographs were recorded at a pixel pitch of 84 μm.

[***] Hitachi S-4800 scanning electron microscope.
[†††] D9500™ C-SAM® acoustic microscope, from Sonoscan Inc.

3.7.3. Transmission Electron Microscopy

To analyze the exfoliation of graphene nanoplatelets, transmission electron microscopy was performed. Nanocomposite thin sections (thickness of 70 nm) for 5% and 15% GNP weight fraction tensile bars were microtomed[‡‡‡] and imaged under a transmission electron microscope[§§§] at an operating voltage of 200 kV. The difference in electron densities between PET and GNP provided the contrast in transmission electron micrographs. Due to the higher electron density of graphene nanoplatelets compared to PET, they can be recognized as the darker regions in the micrographs. Nanoplatelet parameters, thickness and length (diameter) were obtained, by measuring the number of pixels[****] after calibrating the transmission electron micrographs.

Transmission electron micrographs provide 2D dimensions of the nanoplatelets. However, this information alone is not sufficient to quantify their distribution in the polymer matrix. Basu *et al*. [190] has come up with a parameter called 'interparticle distance (λ_d)' to quantify the exfoliation of platelets, based on the information from TEM micrographs. Developed based on the stereological relations for relating the information from a 2D slice to 3D, interparticle distance is the average distance measured between particles in a straight line. Using the binarized TEM micrographs, the interparticle distance was determined based on Equation 9. Interfacial area per unit volume $(S_v)_{P\text{-}G}$ can be obtained by measuring the combined perimeter of the nanoplatelets present per unit area of the micrograph.

$$\lambda_d = \frac{4(1-V_V)}{(S_V)_{P-G}} \tag{9}$$

$$S_V = 4L_A/\pi \tag{10}$$

[‡‡‡] Using Reichert-Jung Ultracut E microtome.
[§§§] JEM-2100 Transmission electron microscope, from JEOL, Ltd..
[****] ImageJ, open source software available through U.S. National Institute of Health, Maryland (http://imagej.nih.gov/ij/).

Where, V_V is the volume fraction of the nanoplatelets, $(S_v)_{P\text{-}G}$ is the polymer-nanoplatelet interfacial area per unit volume of specimen, and L_A is the total perimeter of the platelets per unit area of the 2D micrograph.

Considering the nanoplatelets are disk shaped, with known thickness (t) and aspect ratio (A_f) dispersed in the polymer, theoretical interparticle distance can be estimated using the following equation, which is obtained using Equations 9 & 10.

$$t = \lambda_d V_V \left(A_f + 2\right) / \left[2\left(1 - V_V\right) A_f\right] \tag{11}$$

Where, V_V is the volume fraction of the nanoplatelets, A_f is the nanoplatelet aspect ratio, t is the nanoplatelet thickness, and λ_d is the interparticle distance.

3.7.4. X-Ray Diffraction

X-ray diffraction helps in understanding the dispersion state of nanoplatelets within the polymer matrix, by measuring the spacing between them. Single layer graphene has a two-dimensional (2D) hexagonal lattice. Graphene nanoplatelets with a 3D structure similar to graphite, exhibit "Graphene-2H" characteristic reflections corresponding to the (002) and (004) planes (26.6° and 54.7° 2θ for Cu K_α X-rays). PET with a triclinic crystal structure, primarily exhibits reflections corresponding to the (010), $(1\bar{1}0)$, (100), and $(\bar{1}05)$ (17.5°, 22.5°, 25.6°, and 42.6° 2θ for Cu K_α X-rays) planes [48]. Amorphous PET exhibits a broad halo at about 20° 2θ.

Diffraction patterns of the nanocomposites were collected using a 2D detector and micro diffraction[††††] and a 0.5 mm collimator in reflectance for crystallinity measurements. Cu K_α X-ray radiation (λ = 1.54184 Å) was used with a scan time of 60 sec. Percent crystallinity can be determined based on the amorphous and crystalline fractions, using the relation shown in Equation 11.

[††††] Bruker D8 Discover micro-X-ray diffraction system equipped with a General area Diffraction Detection System (GADDS) and Hi-Star 2D area detector.

$$X_c\% = \frac{A_c}{A_a + A_c} \times 100\% \tag{12}$$

Where, A_c is the crystalline contribution and A_a is the amorphous contribution.

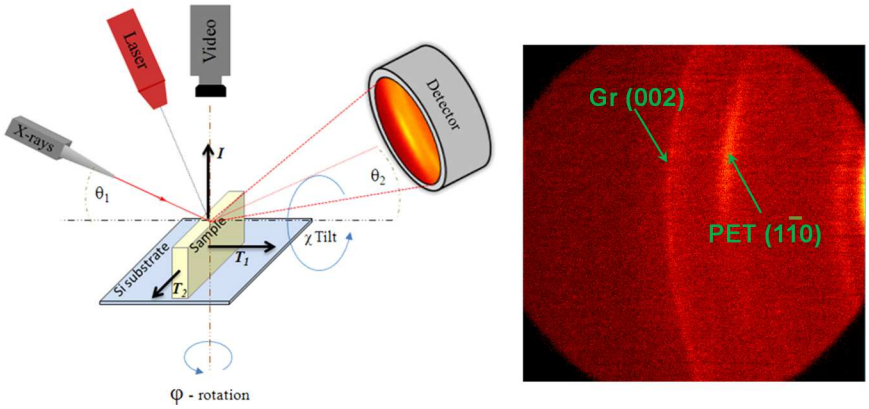

Figure 23: Sample geometry w.r.t. the instrument geometry, 2-D XRD frame.

Sample geometry (I – injection flow direction, T_1 – longer dimension of the cross-section, T_2 – thickness) with respect to the instrument geometry is shown in Figure 23. A 2-D diffraction frame showing the partial diffraction rings for PET and graphene, indicating the presence of preferential orientation is shown in Figure 23. Location of the nanocomposite samples used for diffraction and tomography are shown in Figure 24.

Figure 24: Location of samples collected for nano-tomography and diffraction analysis.

3.7.5. X-Ray Tomography

Electron microscopy provides only two-dimensional microstructure information of the sample from a small area. In case of TEM the sample size is only 500 µm×500 µm in area and 70 nm in thickness. Electron microscopy combined with focused ion beam (FIB) can be useful in attaining microstructure information along the third direction. Nevertheless, X-rays have certain

advantages over electrons, in imaging materials. Simplicity with sample preparation, choice of ambient or *in-situ* environments, and less induced damage to the material [191] are the major advantages. X-ray tomography is a non-destructive imaging technique that allows regenerating the 3D structural details of materials.

Tomography is the process of collecting cross-sectional information either in transmission or reflection mode, from an illuminated object. Material and geometry information is recorded (radiograph) based on the transmitted intensity of the X-rays, as illustrated in Figure 25. This transmitted intensity can be related to the material information based on the material's X-ray absorption coefficient and density, as seen from Equation 12. Radiographs are reconstructed into cross-sectional slices (tomographs) using Fourier transform based algorithms. Developments in the field of X-ray and detector optics have allowed focusing the beam on a much smaller area, thereby attaining nanoscale resolution.

$$I = I_o e^{-\mu_m \rho x} \tag{13}$$

Where, I is the transmitted X-ray intensity, I_o is the initial X-ray intensity, μ_m is mass attenuation coefficient of the material, ρ is the material density, and x is the material thickness.

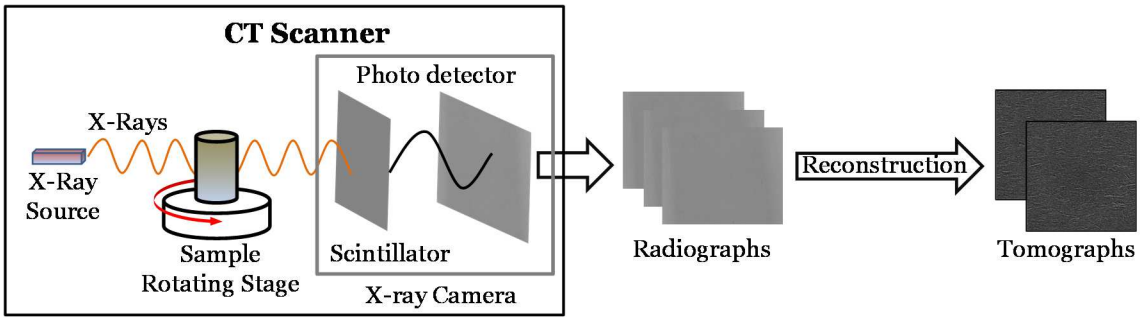

Figure 25: Schematic showing the components of a CT scanner and the process of X-ray computed tomography.

In the current work, X-ray nanotomography was attempted on two different samples (nanocomposite tensile bar and tensile tube) with the objective of understanding nanoplatelet distribution in three-dimensions. Nanotomography of the sample collected from 15% tensile bar was performed on a SkyScan 2011 nano-CT instrument at 272 nm/pixel resolution. For the tensile tube sample of 2% weight fraction (ultrasound processed), wedge sections from the inner and outer surfaces were scanned on an Xradia 800 Ultra 3D X-ray Microscope at 65 nm/pixel resolution. Reconstructed tomographs were visualized using 3D visualization software‡‡‡‡.

3.8. Micromechanical Modeling of Nanocomposites

Continuous fiber composites are often designed or assessed based on a simple empirical formula, referred to as the "Rule of Mixtures". In the case of nanoreinforcements, the Rule of Mixtures poorly predicts the final properties. Along with the fact that these are not continuous fiber reinforcements, the differences are influenced by the low volume fractions, significant disparity of properties between the matrix and reinforcement, and aspect ratio. For nanocomposites, the spatial interaction between the nanoplatelets and matrix is important in determining their elastic behavior. High aspect ratios of the nanoplatelets combined with interactions at the matrix-reinforcement interface complicate nanocomposite property estimation. Therefore, traditional

‡‡‡‡Amira – a licensed product of Mercury Computer Systems.

micromechanical models have been modified to estimate the mechanical properties for nanoparticles [192].

With the objective of understanding the effectiveness of graphene nanoplatelets as reinforcement, micromechanical models such as the Halpin-Tsai and the Hui-Shia models were used to determine the theoretical elastic mechanical performance of the PET-GNP nanocomposites. These models were simplified micromechanical relations of continuum based Mori-Tanaka and Hill's methods for predicting composite properties [43, 44]. Both these models were designed for unidirectional composites. Aspect ratio of the nanoplatelets dispersed into the polymer can be determined from the transmission electron micrographs. In the Halpin-Tsai model, the longitudinal modulus (E_{11}) of the composite is predicted using the following equations:

$$\frac{E_{11}}{E_m} = \frac{1 + 2A_f \eta \phi}{1 - \eta \phi} \tag{14}$$

$$\eta = \frac{E_r - 1}{E_r + 2A_f} \tag{15}$$

Where A_f is the aspect ratio of the nano-reinforcement (D/t), ϕ is the volume fraction of the reinforcement, E_r is the ratio of reinforcement modulus to matrix modulus (E_m).

In case of Hui-Shia model, modulus predictions are made using the below given equations:

$$E_L = E_m \left[1 - \frac{\phi}{\xi} \right]^{-1} \tag{16}$$

$$E_T = E_m \left[1 - \frac{\phi}{4} \left(\frac{1}{\xi} + \frac{3}{\xi + \Lambda} \right) \right]^{-1} \tag{17}$$

$$\xi = \phi + \frac{E_m}{E_f - E_m} + 3(1 - \phi) \left[\frac{(1 - g)\alpha^2 - g/2}{\alpha^2 - 1} \right] \tag{18}$$

$$\Lambda = (1-\phi)\left[\frac{3(\alpha^2+0.25)g - 2\alpha^2}{\alpha^2-1}\right] \tag{19}$$

$$g = \begin{cases} \dfrac{\alpha}{(\alpha^2-1)^{3/2}}\left[\alpha\sqrt{\alpha^2-1} - \cosh^{-1}\alpha\right] \rightarrow \alpha \geq 1 \\ \dfrac{\alpha}{(1-\alpha^2)^{3/2}}\left[-\alpha\sqrt{1-\alpha^2} + \cosh^{-1}\alpha\right] \rightarrow \alpha \leq 1 \end{cases} \tag{20}$$

Where, ϕ is the volume fraction of the reinforcement, α is the inverse aspect ratio (t/D), E_m is the Young's modulus of matrix (PET), and E_f is the Young's modulus of reinforcement phase (graphene nanoplatelets).

CHAPTER IV

RESULTS

With the objective of improving the properties of PET, graphene nanoplatelets were compounded with PET and injection molded into nanocomposites of specific loading rates. Nanocomposites obtained from this process were evaluated for their mechanical, thermal, and rheological properties to understand the effectiveness of graphene nanoplatelets.

4.1. Average Molecular Weight

The average molecular weight was obtained from Gel Permeation Chromatography (GPC), for the following samples: control PET, ultrasound treated PET, ultrasound treated nanocomposite masterbatch (5% GNP), and twin-screw compounded masterbatch with 5% GNP weight fraction. Comparing masterbatches with similar GNP weight fraction can be helpful in understanding changes that occurred due to the presence of graphene.

Based on the weight average molecular weight (M_w) shown in Figure 26, the following observations were made. First, the average molecular weight changes with twin-screw processing, irrespective of ultrasound treatment. A decrease in the molecular weight through ultrasound treatment alone is less significant compared to the drop from twin-screw compounding.

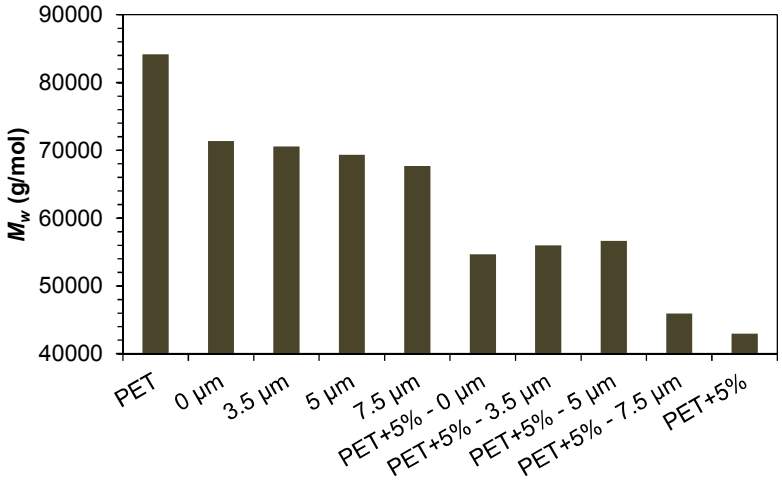

Figure 26: Weight average molecular weight of PET and PET nanocomposite pellets.

In addition to the above observations, it is also noticed that the drop in molecular weight increased with the presence of graphene. From the molecular weight measurements, ultrasound treated samples have shown a polydispersity index (ratio of weight average to number average molecular weight) of 1.8 and 1.9 for nanocomposites with 5% GNP.

4.2. Intrinsic Viscosity

Intrinsic Viscosity (I.V.) is the most commonly denoted number in reference to discussions comparing properties of poly(ethylene terephthalate). Therefore, the intrinsic viscosity of PET and ultrasound treated PET samples, shown in Figure 27, were obtained by capillary viscometer using polymer dissolved solvents.

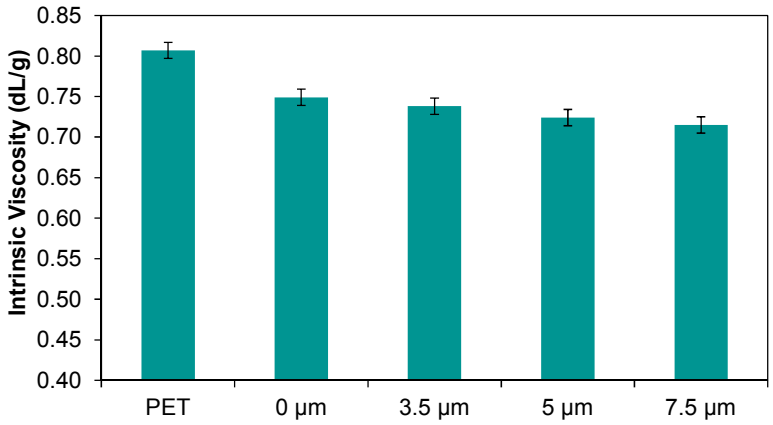

Figure 27: Intrinsic viscosity measured for PET and ultrasound treated PET.

Correlating the experimentally obtained viscosities with the viscosities calculated by means of the weight average molecular weight, using Equation 5, Mark-Houwink parameters *'K'* and *'a'* were optimized to the following values 0.00047 and 0.658 respectively. Using the new constants, intrinsic viscosity for the nanocomposite samples was obtained. Calculated viscosity values for both PET and PET nanocomposite samples are presented in Figure 28.

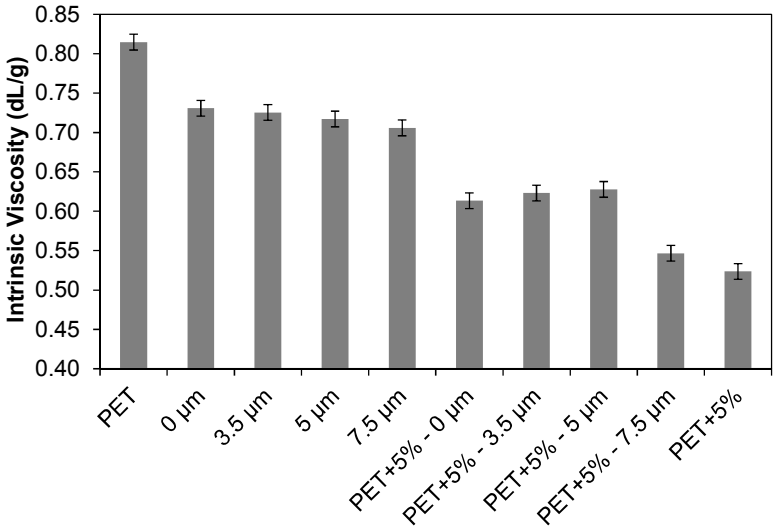

Figure 28: Intrinsic viscosity compared for PET and PET nanocomposites.

Intrinsic viscosities for the *in-situ* polymerized PET and nanocomposite pellets, collected experimentally are shown in Figure 29. All of them show viscosities in the range of 0.6 dL/g.

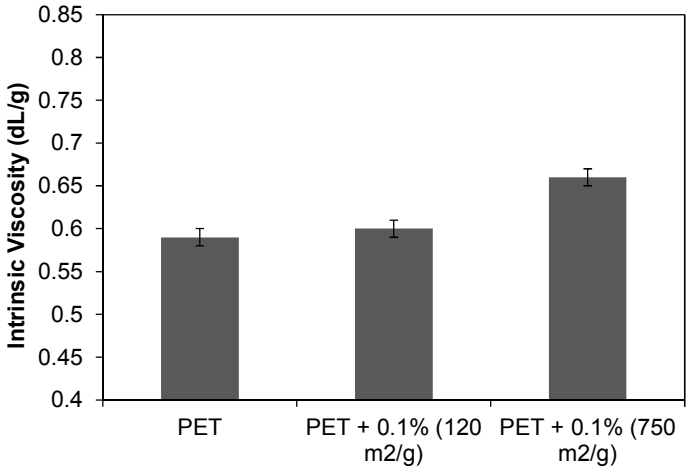

Figure 29: Viscosity of the pellets obtained from *in-situ* polymerization.

4.3. Mechanical Behavior

4.3.1. Nanocomposites Tensile Bars (Oil Cooled)

Stress-strain curves for the tensile bar samples were presented in Figure 30. Young's modulus was obtained from the initial region of the stress-strain curve. Young's modulus and strength data for the nanocomposite tensile bars (Set-A) are presented in Figure 31. A decrease in strength of the nanocomposites when compared with the control PET was observed. Further, nanocomposites had a brittle failure with a loss in elongation, compared with the control PET sample.

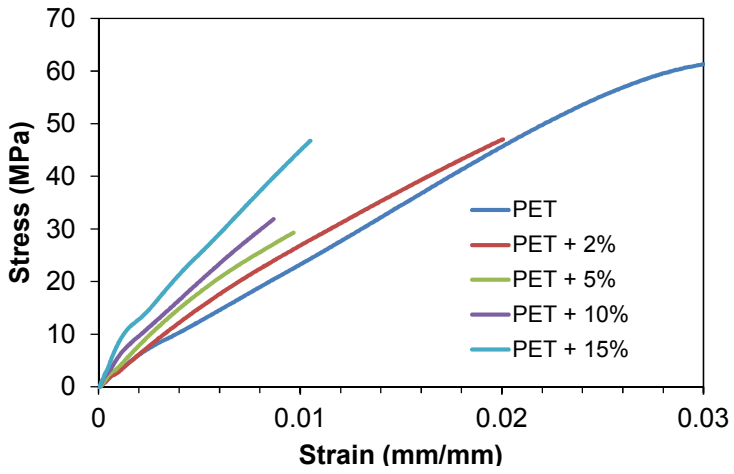

Figure 30: Engineering stress-strain curves for PET and PET-GNP nanocomposites [193].

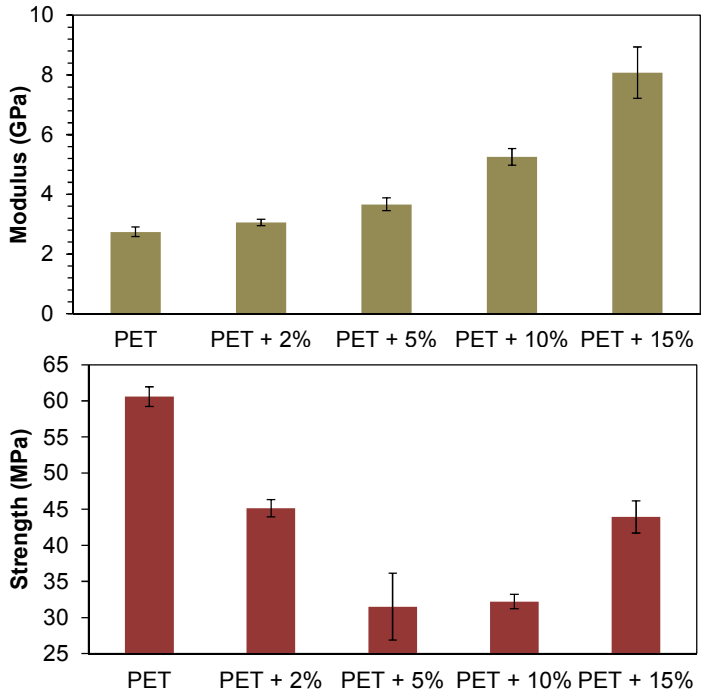

Figure 31: Young's modulus and tensile strength of the nanocomposite tensile bars.

4.3.2. Nanocomposite Tensile Tubes

Using a custom fixture, PET and nanocomposite tensile tubes were tested for their mechanical properties. Young's modulus and the tensile strength of PET and nanocomposites were shown in

Figure 33. The PET modulus from the tensile tube was less than the tensile bar samples (difference of 0.2 GPa), as the tensile bars exhibited thermal crystallinity due to slower cooling (19%). The modulus of the nanocomposties increased with increasing GNP content. However, the strength of the nanocomposites remained the same as PET, except in the case of a 2% sample. Stress-strain curves for PET tensile bar (2% GNP) and nanocomposite tensile tubes of low GNP weight fractions (0.6% and 1.2% GNP) are compared in Figure 34. This plot shows that the nanocomposites are tougher (area under the stress-strain curve) than PET. Figure 32 presents mechanically tested PET and nanocomposite samples (tensile bar and tube), for comparing their failure types. The Young's modulus for the 2% nanocomposite was identical from the two different injection molding processes used (3.1 GPa). However, nanocomposite tubes with 2% GNP loading deviated in the type of failure with respect to lower weight fractions. At 2% GNP loading, nanocomposites exhibited only 1% strain which is significantly lower compared to failure strain for 1.2% GNP loading (400%).

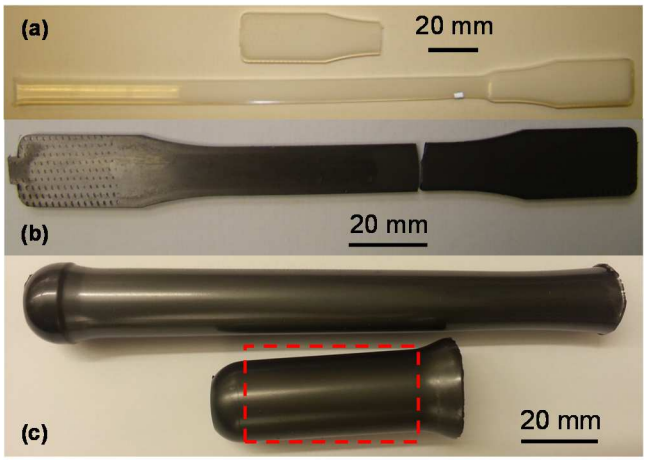

Figure 32: (a) PET tensile bar, (b) PET-15% GNP tensile bar after testing, and (c) PET-GNP tensile tubes stretched (common failure) and brittle failure (unusual failure for 2% sample, failure in general happened with in the marked region).

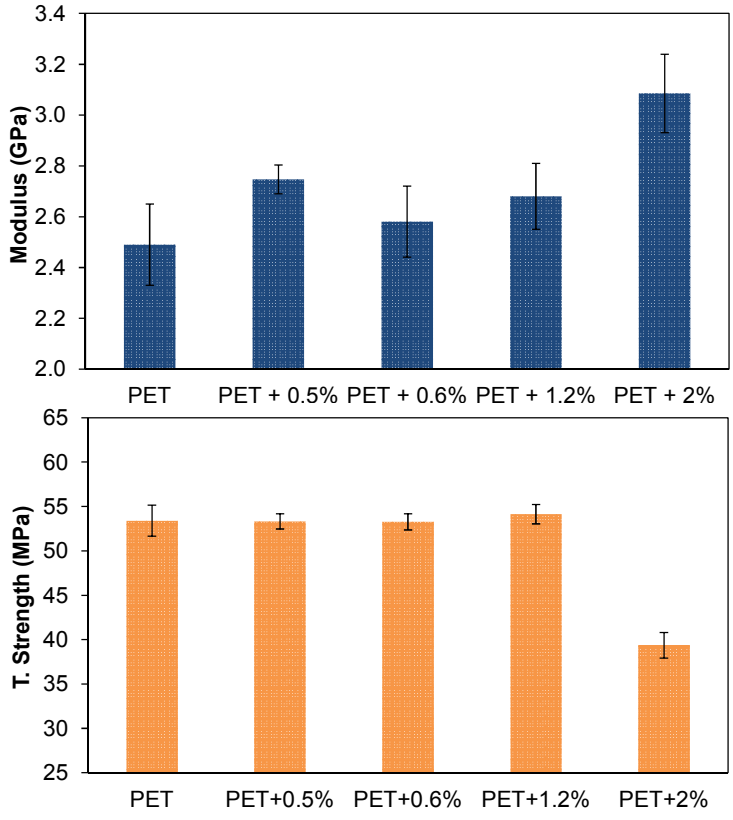

Figure 33: Modulus and tensile strength of PET and nanocomposite tensile tubes.

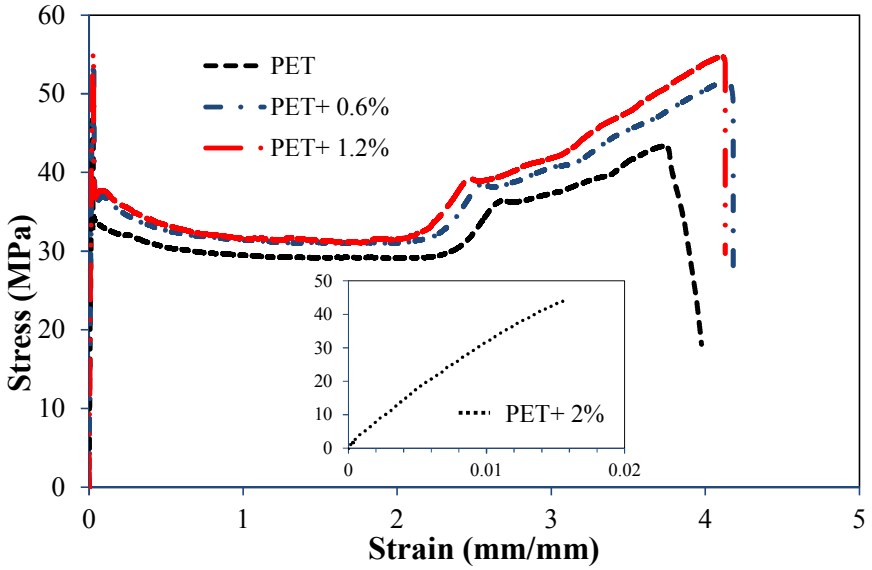

Figure 34: Engineering stress-strain curves of nanocomposite tensile tubes compared with tensile bar (shown in the insert).

4.3.3. Ultrasound treated PET

Tensile bars of PET and ultrasound treated PET obtained from the micro injection molding process were tested for their mechanical properties. Figure 35 compares the Young's modulus and strength data for ultrasound treated PET with control PET. It was observed that the ultrasound treatment of PET did not have a significant effect on its modulus and strength. However, the ultimate tensile strength (tensile strength at breaking) for the ultrasound treated PET increased significantly (by 24%), as shown in Figure 36.

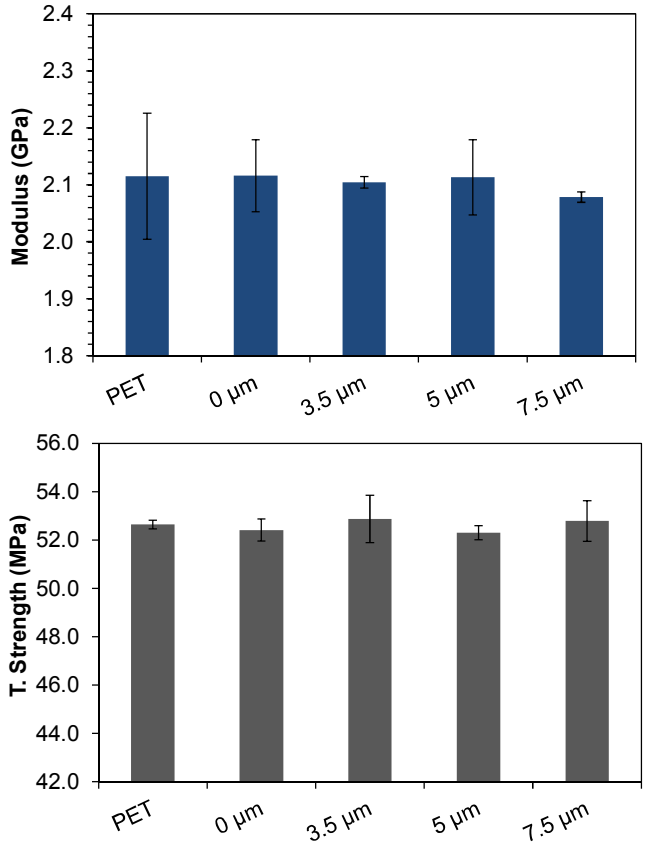

Figure 35: Young's modulus and tensile strength of ultrasound treated PET (horizontal axis - ultrasound amplitude) compared with PET control.

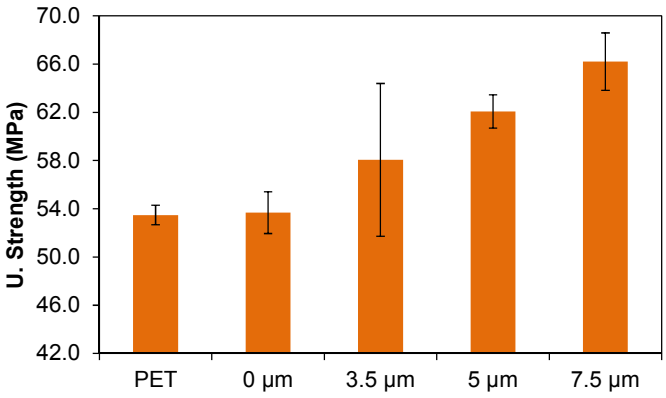

Figure 36: Ultimate tensile strength of ultrasound treated PET (horizontal axis – ultrasound amplitude) compared with PET control.

4.3.4. Ultrasound treated Nanocomposites

Using the ultrasound treated masterbatch pellets; nanocomposite tensile tubes at 2% GNP loading were prepared and tested for comparison with nanocomposites from twin-screw compounding. Nanocomposites prepared from compounded pellets treated with different ultrasound amplitudes show improvement in Young's modulus and tensile strength. Improvement in modulus for nanocomposites with 3.5 μm ultrasound amplitude was higher (2.7 GPa – 12% improvement) compared with other ultrasound treatments, as seen from Figure 37. Nevertheless, the increase in modulus for ultrasound treated 2% nanocomposites is lower compared with the twin-screw compounded nanocomposites at 2% GNP (3.1 GPa – 24% improvement). Ultrasound treated nanocomposites displayed yielding behavior similar to PET, but with only 3% maximum improvement in strength.

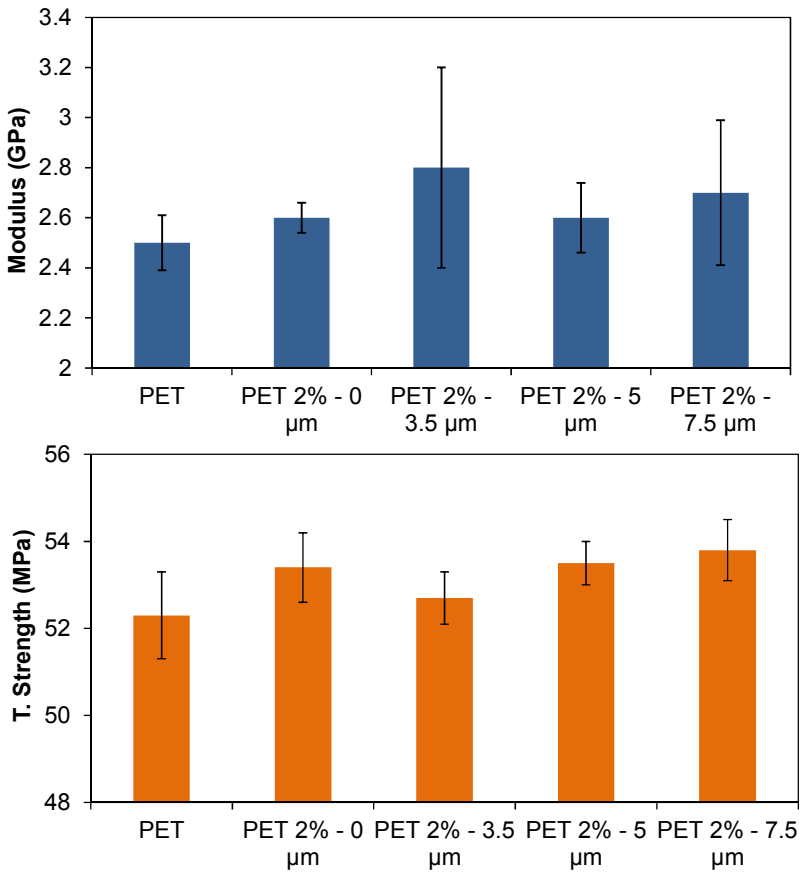

Figure 37: Modulus and strength of ultrasound processed nanocomposites with 2% GNP.

Nanocomposites prepared through dilution of ultrasound treated masterbatch did not provide conclusive evidence to understand the change in mechanical properties. Therefore, tensile bars with 5% GNP weight fraction were obtained from micro injection molding system, using the ultrasound treated masterbatch pellets (with no dilution of GNP weight fraction). The Young's modulus and the tensile strength of the 5% GNP nanocomposite tensile bars were compared with control PET and tensile bars prepared using 5% pellets from twin-screw compounding process, in Figure 38. While the strength data indicate a recovery in tensile strength with increase in ultrasound amplitude, the modulus data points out that the improvement from ultrasound treatment is not significant compared to the regular twin-screw mixing.

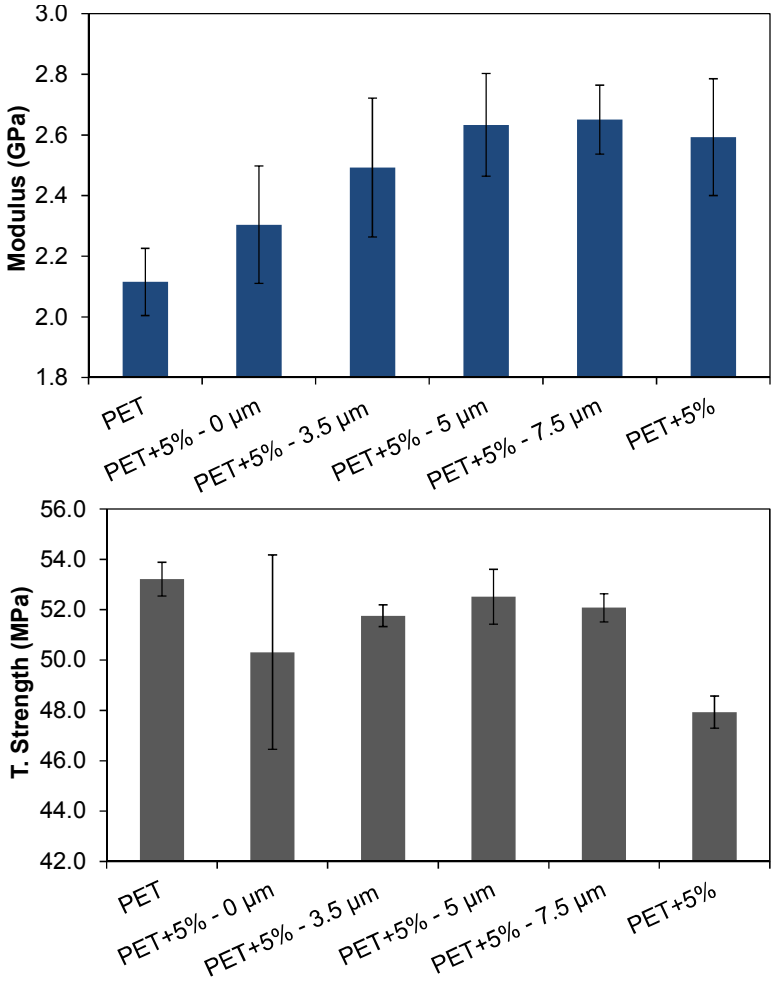

Figure 38: Modulus and strength of ultrasound treated nanocomposites (at 5% GNP) compared with PET control and twin-screw compounded nanocomposite.

4.3.5. Nanocomposites from *in-situ* Polymerization

Tensile bars of PET control and nanocomposites with 0.1% GNP weight fraction obtained from the polymerization process were tested for their mechanical properties. Figure 39 compares the Young's modulus and strength data for PET and nanocomposites with 0.1% GNP of different surface areas. While there is no significant difference in the modulus of the nanocomposites, strength exhibited two different trends. Ultimate strength of the nanocomposites shows significant (minimum 16%) improvement over the PET control. On the contrary, tensile strength of the nanocomposites decreased slightly (by 5%) over PET.

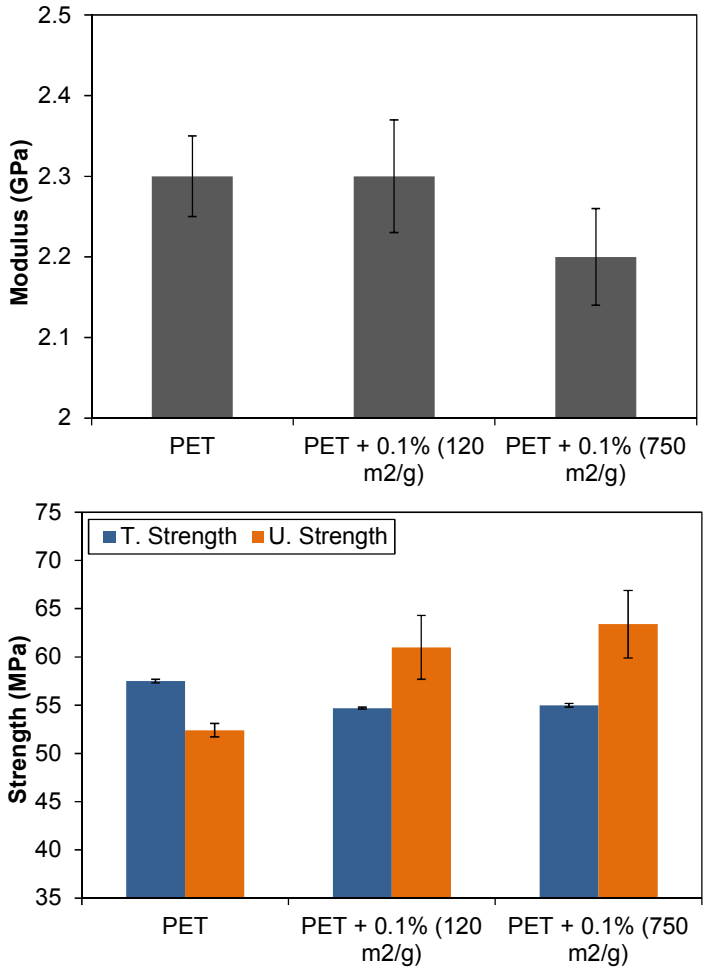

Figure 39: Young's modulus and strength data for *in-situ* polymerized PET and nanocomposites.

4.4. Density Measurements

Densities for the nanocomposites were measured using Archimedes' principle. The densities of the nanocomposites were different from the theoretical values estimated based on amorphous PET and graphene. Comparison of densities between the molded PET tensile bars and tensile tubes, indicate that the tensile bars were semi-crystalline (19% crystallinity, based on Equation 2). Density measurements from the nanocomposite samples deviate from theoretical values (based on the Rule of Mixtures). In order to make a better comparison on the strength of nanocomposites,

densities were collected for samples before testing and used to estimate their specific strength, presented below.

Table 10: Specific strength for nanocomposite tensile bars (oil cooled).

Sample Type	Tensile Strength (MPa)	Density (kg/m^3)	Specific Strength (kN.m/kg)
PET	64.8	1355	47.9
PET - 2%	50.3	1359	37
PET - 5%	33.9	1376	24.6
PET - 10%	31.7	1392	22.8
PET - 15%	43.0	1426	30.2

Table 11: Specific strength for nanocomposite tensile tubes.

Sample Type	Tensile Strength (MPa)	Density (kg/m^3)	Specific Strength (kN.m/kg)
PET	53.4	1335	40
PET + 0.6%	53.28	1331	40
PET + 1.2%	54.14	1336	40.5
PET + 2%	39.4	1344	29.3

Table 12: Specific strength of nanocomposite tubes from ultrasound masterbatch.

Sample Type	Tensile Strength (MPa)	Density (kg/m^3)	Specific Strength (kN.m/kg)
PET	52.3	1336	39.2
0 USM	53.4	1336	40.0
3.5 USM	52.7	1340	39.3
5 USM	53.5	1338	40.0
7.5 USM	53.8	1345	40.0

Specific strength values presented above show no significant loss or improvement in strength of PET with GNPs, except for the nanocomposite tensile tubes with 2% GNP weight fraction.

4.5. Scanning Electron Microscopy

Comparing stress-strain curves of the nanocomposites with PET shows that the failure strain (elongation) of the nanocomposite tensile bars decreased. To understand the type and reasons for the failure of nanocomposites, scanning electron micrographs were collected. Fracture surface micrographs show the presence of micro voids, as seen in Figure 40. Moisture present in the pellets can give rise to voids during their processing. Therefore, the increase in the stress concentration near the voids contributed in lowering the strength of the nanocomposite tensile bars. Initiation of the crack from the void, as seen from the fracture surface micrographs (Figure 40b), confirms this observation.

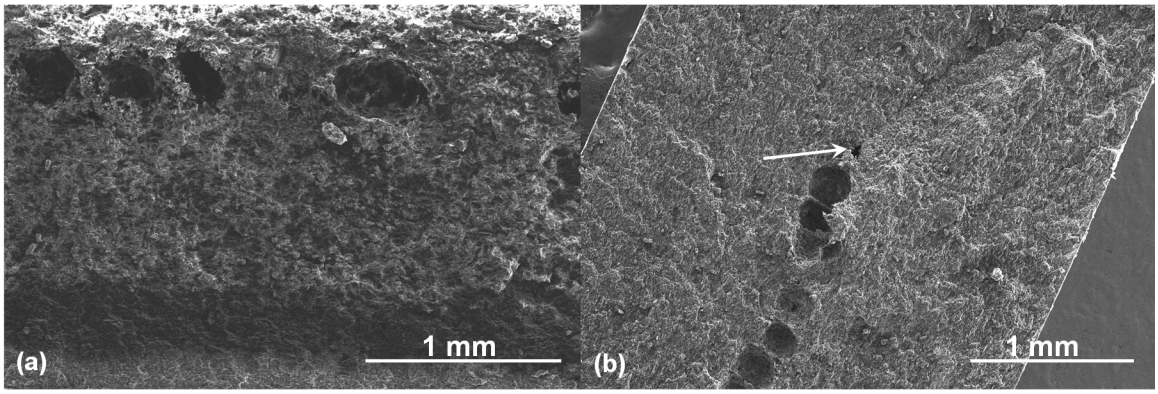

Figure 40: Voids observed on the fracture surface (a) 5% and (b) 10% wt. (arrow pointing at crack initiation point).

Similar observations were made from the micrographs of the fracture surface of nanocomposite tensile tubes with 2% GNP weight fraction. Nanocomposite tensile tube showed signs of "ductile fracture", as shown in Figure 41. Voids observed in this set of samples are very small < 10 μm in size, pointed with arrows in Figure 41 (a). Localized ductile deformation of the polymer matrix

through fibril stretching, surrounding the micro voids can increase the local stress concentration. This increase in the stress concentration can initiate cracks, which lead to the brittle fracture of the nanocomposite.

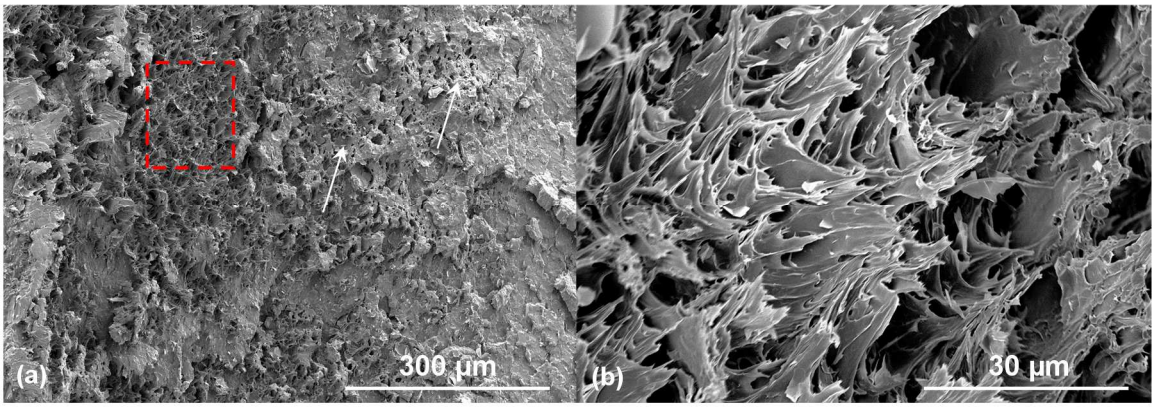

Figure 41: (a) Fracture surface of 2% nanocomposite tensile tube, highlighted region show signs of "ductile fracture" and (b) failure of the micro fibril formed from elongation (from the highlighted area).

At higher magnification, graphene nanoplatelets were observed on the fracture surfaces. Nanoplatelets, as pointed out in the SEM micrographs shown in Figure 42, are projecting out of plane to indicate they were exposed during the failure and were part of load sharing. At higher nanoplatelets content (15%), the microstructure of the nanocomposite is different from others with more local fractures. One difficulty with the nanocomposite is the ability to make clear amorphous samples. Having clear PET tensile bars helps eliminate defects caused by poor processing, such as voids. Since these nanocomposites are dark the voids must generally wait to be visually observed by destructive methods.

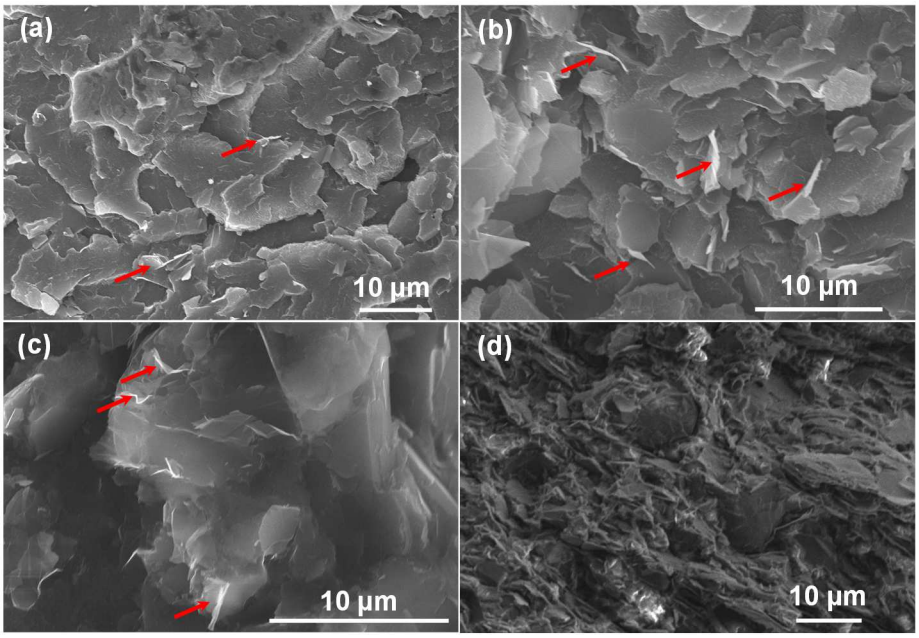

Figure 42: SEM micrographs of the nanocomposite tensile bar failure surfaces (a) 2%, (b) 5%, (c) 10%, and (d) 15% weight fractions [172].

4.6. Ultrasound Imaging

A nondestructive alternative to imaging voids is ultrasound imaging. Ultrasound micrographs of the tensile bars from the ultrasound "Bulk Scan" are shown in Figure 43. These micrographs show the presence of voids along the length of the tensile bar. Based on the micrographs, it was inferred that the voids are a result of processing. Further, densities of the ultrasound imaged samples were compared with the mechanical tests to confirm that the deviation in the densities is due to the presence of voids.

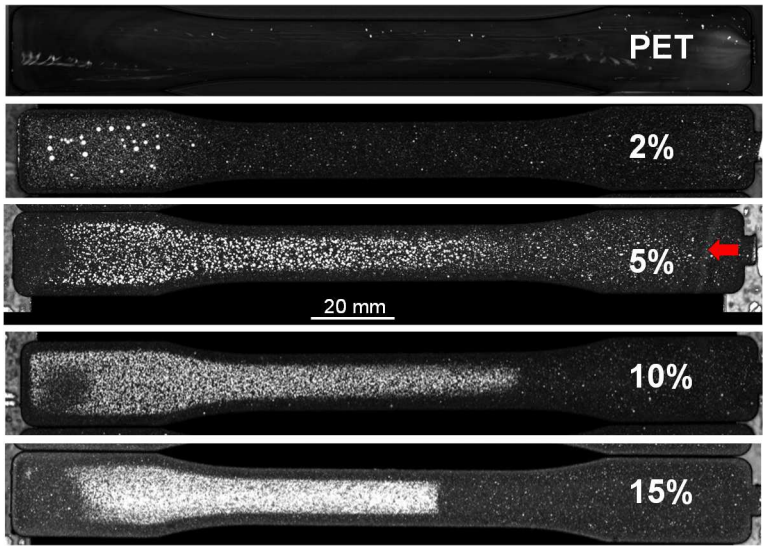

Figure 43: Ultrasound micrographs of PET and PET nanocomposite tensile bars (arrow indicates the injection flow direction).

4.7. Thermal Analysis

4.7.1. Nanocomposites from Twin Screw Compounding

The melt and crystallization behavior of the nanocomposites were analyzed through DSC measurements. Figure 44 presents the glass transition (T_g) and melting temperatures (T_m) from the second heating cycle, and crystallization temperature (T_c) from the first cooling cycle, plotted with respect to the GNP weight fractions for twin-screw compounded pellets. While the melting temperature shifted to higher values with increasing GNPs, the glass transition showed a decreased trend except for at 15% weight fraction. A decrease in the glass transition temperature (Figure 44) can be due to the agglomeration of nanoplatelets inside the PET matrix. Agglomerated platelets can act as plasticizers and affect the glass-transition temperature.

Both crystallization and melt temperatures increased with increasing GNP content. The melting temperature of PET is dependent on the crystal shape and size [194]. As seen from Figure 44, the addition of GNPs increases the melting temperature. This can be due to the formation of larger

and more perfect crystals indicated by the higher (10°C to 18°C) crystallization temperature [195] and expected with the presence of nucleation sites (nanoplatelets) [167]. While the change in melting temperature is small, the crystallization temperature increased with increasing GNP content. Increases in the crystallization temperature are due to a nucleation effect from the presence of GNPs which become stronger with the increasing GNP weight fraction. The change in crystallization temperature and shape of the exothermic peak with GNP weight fraction can be seen from Figure 46.

Using the crystallization exotherms for nanocomposite pellets, presented in Figure 46, on-set temperatures (T_{on}) were obtained to determine the crystallization half-time ($t_{1/2}$) using Equation 7. It was observed that with an increase in the GNP content, the crystallization half-time (inverse of crystallization rate) increased. A decrease in the crystallization rate indicates that with an increase in the GNP content, PET chain mobility is affected [167]. As a result, the crystallinity of the nanocomposites decreased at higher graphene loadings, as seen from Figure 45.

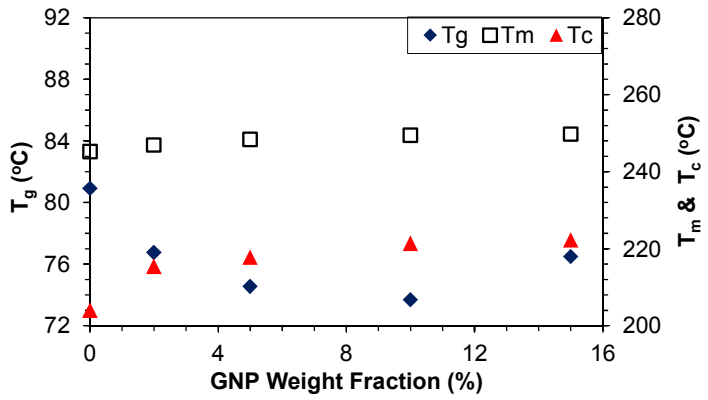

Figure 44: GNP weight fraction vs. glass transition (T_g), melting (T_m) and crystallization temperatures (T_c) (error on temperature measurements – 0.5°C).

The percentage crystallinity presented in Figure 45 (right), for the as received injection molded tensile bars was measured through Differential Scanning Calorimetry (DSC). The crystallinity measured for the injection molded nanocomposites shows a similar trend to the non-isothermal

crystallinity obtained through DSC. This confirms the above observation that an increase in GNP allows early nucleation of PET, but restricts chain mobility.

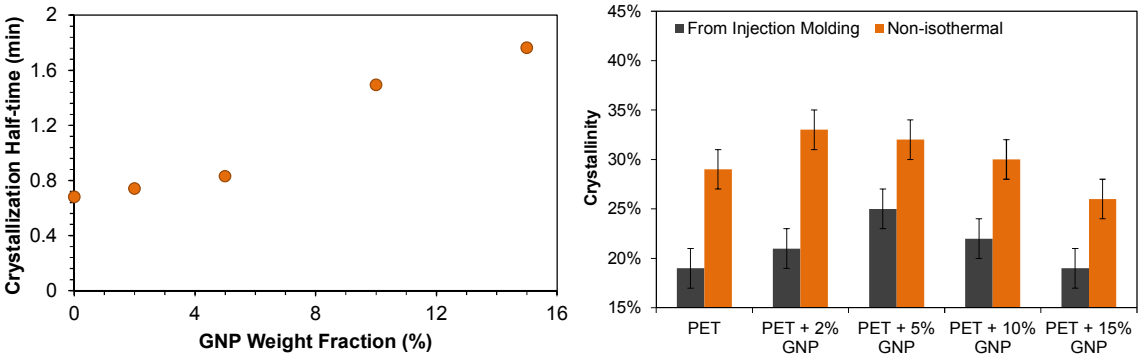

Figure 45: (left) Crystallization half-time (measurement error – 0.05 min) and (right) percent crystallinity of PET nanocomposites.

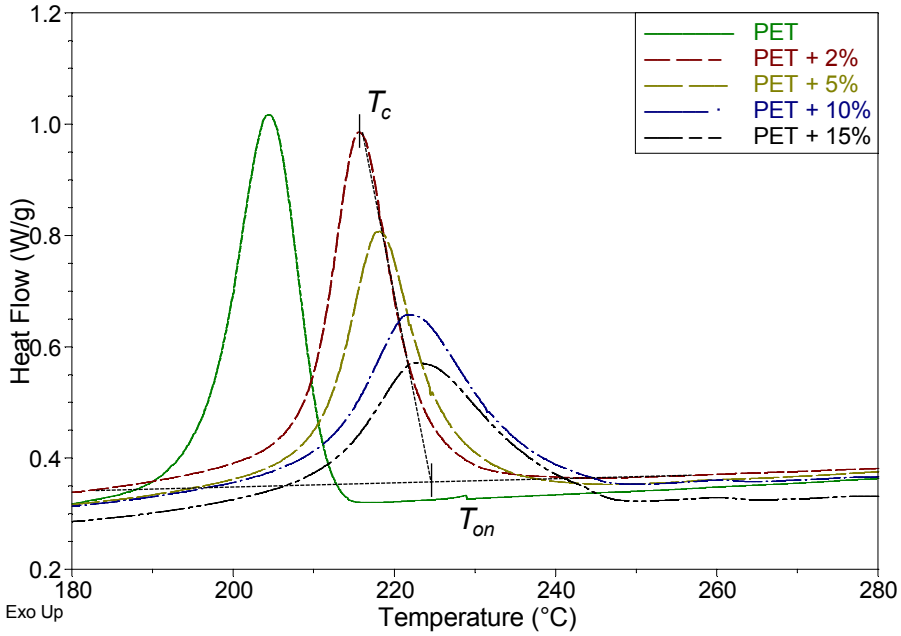

Figure 46: Crystallization exotherms for PET and twin-screw compounded PET nanocomposite pellets.

4.7.2. Ultrasound Treated PET and Nanocomposites

Ultrasound treated PET and PET-5% GNP nanocomposite pellets were analyzed for their change in thermal properties. Glass transition and melting temperatures are presented in Figure 47. The glass transition temperature of PET decreased with the addition of GNPs for the no ultrasound condition (0 USM). Ultrasound treatment was observed to have an effect on the glass transition temperature (T_g) of both PET and PET nanocomposites. For PET, the glass transition followed a decreasing trend except for at the 7.5 µm amplitude. The change in 'T_g' for PET points towards polymer softening with increase in ultrasound amplitude. The glass transition temperature for nanocomposites increased with the ultrasound amplitude. However, the 'T_g' of the nanocomposite was still lower than PET. Crystallization temperatures for PET and PET-5% GNP pellets remained constant regardless of the ultrasound amplitude, at 194°C and 214°C respectively.

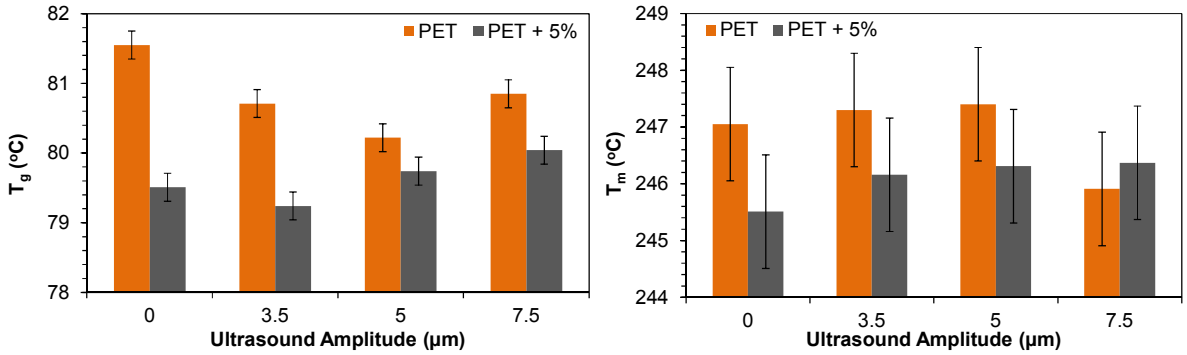

Figure 47: Glass transition and melting temperatures for ultrasound treated PET and PET nanocomposite pellets.

Multiple melting peaks were observed in the melting endotherm for ultrasound treated PET (Figure 48). Multiple melting peaks indicate the presence of different crystals sizes, potentially indicating at a broader molecular weight distribution.

The crystallization half-time ($t_{1/2}$) for PET decreased with ultrasound treatment. With the addition of GNPs the '$t_{1/2}$' increased for all the ultrasound amplitudes, as shown in Figure 49. The increase in the crystallization half-time for the 5 µm amplitude condition nanocomposite was less compared to other ultrasound amplitudes. Non-isothermal crystallinity for the ultrasound treated PET increased with the increase in amplitude, except for the case of 7.5 µm amplitude. Presence of graphene increased the crystallinity, however maximum change in crystallinity was observed only in the case of 7.5 µm amplitude.

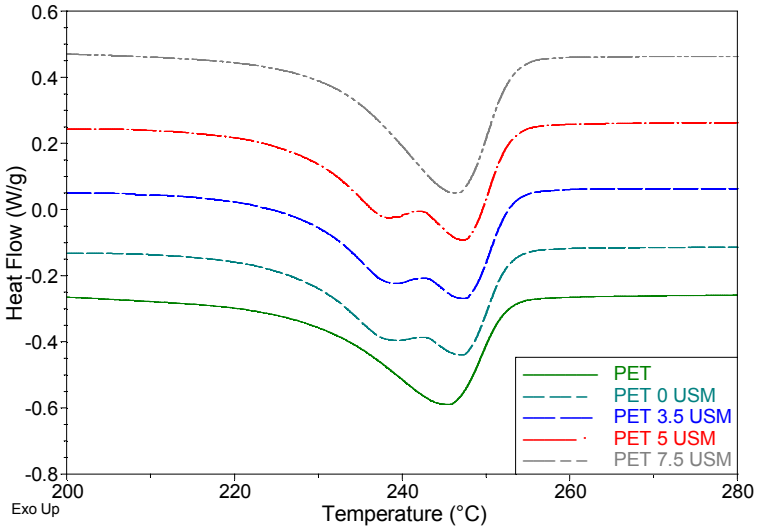

Figure 48: Melting curves (second heat) of the ultrasound treated PET.

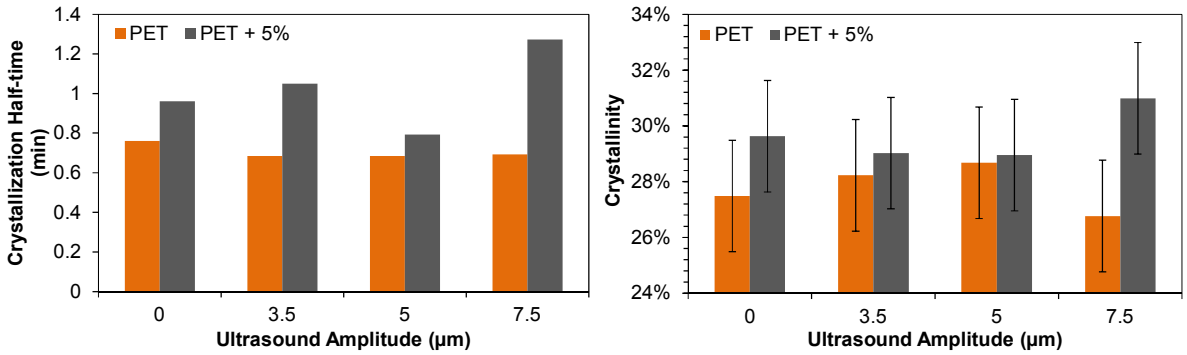

Figure 49: (left) Crystallization half-time (measurement error – 0.05 min) and (right) crystallinity for ultrasound treated PET and PET + 5% GNP pellets.

Tensile bars of ultrasound treated PET and PET nanocomposites obtained from micro injection molding were evaluated for percentage crystallinity. Under similar conditions, ultrasound treated PET samples have 8% crystallinity and ultrasound treated nanocomposites have 11 to 13% crystallinity.

4.7.3. Nanocomposites from *in situ* polymerization

PET control and nanocomposites obtained from *in situ* polymerization were evaluated for their crystallization behavior. At 0.1% loading, graphene nanoplatelets with a higher average surface area (750 m^2/g) had a stronger nucleation effect compared to nanoplatelets with lower average surface area (120 m^2/g). Crystallization temperature and the non-isothermal crystallinity are higher for high surface area graphene, as shown from Figure 50.

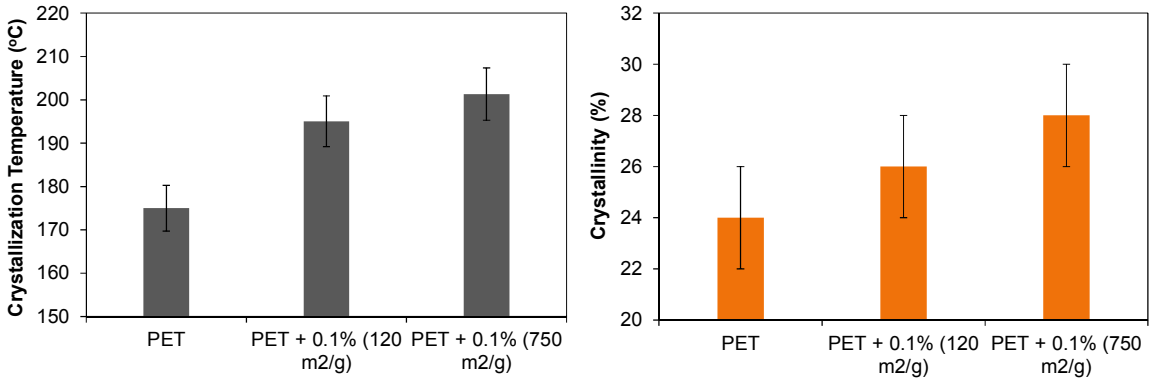

Figure 50: Crystallization temperature and percent crystallinity for *in situ* polymerized samples.

4.8. Dispersion Studies

4.8.1. Melt Rheology

Melt rheology of the nanocomposites was studied to understand the extent of nanoplatelet dispersion in PET. Dynamic frequency sweeps for the nanocomposite pellets from twin-screw compounding along with control PET are presented in Figure 51. The shear storage modulus (G') of PET decreased linearly with frequency. The addition of graphene nanoplatelets to PET improved its modulus (G'). In the case of PET-2% GNP nanocomposite pellets, the modulus (G') transitioned from a linear region (dependent) to a plateau (independent of the angular frequency) below 0.3 rad/s. This transition point for 5% nanocomposite moved up to 64 rad/s frequency. Nanocomposites with 10% and 15% GNP weight fractions, exhibited rigid behavior even when tested at 320°C with a gap of 1.6 mm (melt thickness between parallel plates). The percolation threshold (ϕ_{per}) for twin-screw compounded PET-GNP nanocomposites was determined to be 1.75 %wt. (1.1 %vol.), based on the linear regression of the G' values at 0.1 rad/s for 2% and 5% samples, as illustrated in Figure 52. The nanoplatelet aspect ratio at the percolation threshold was evaluated as 40, based on Equation 8.

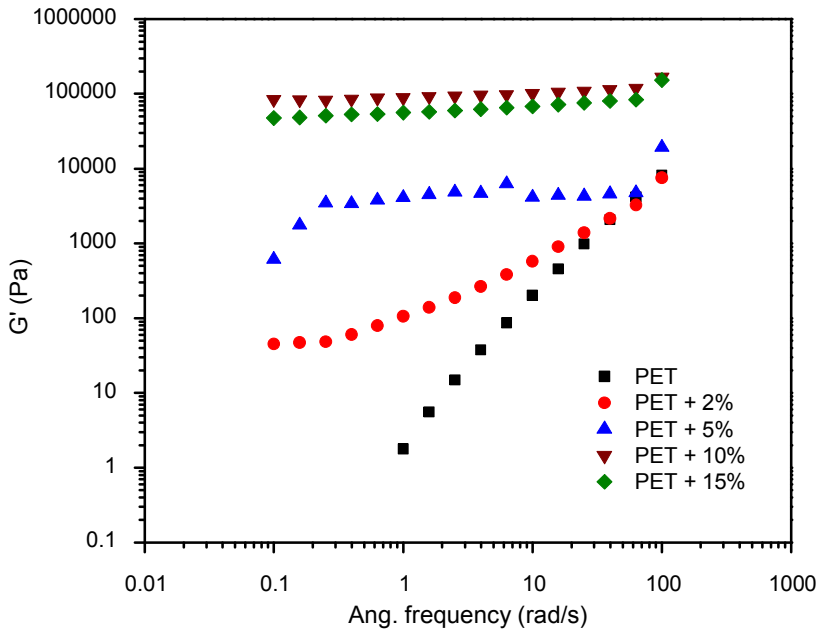

Figure 51: Storage modulus of PET and PET nanocomposites with respect to angular frequency.

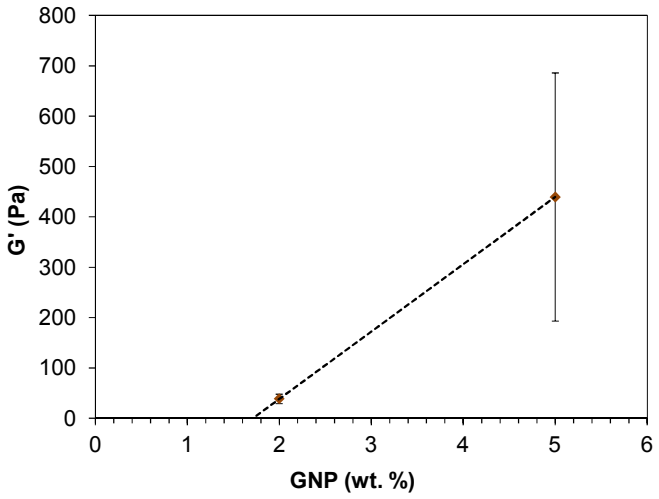

Figure 52: Shear modulus vs. GNP weight fraction and the suggested percolation threshold.

Ultrasound assisted compounding of PET and graphene nanoplatelets showed more linear response compared to twin-screw compounding for the same weight fraction (5%), as seen from

Figure 53. At low frequencies, nanocomposites with a lower ultrasound amplitude exhibited higher storage moduli. This indicates that increasing the ultrasound amplitude has an effect on nanoplatelet dispersion. As the moduli at higher frequencies are an indication of the polymer behavior, a decrease in the moduli compared to the PET control hints at change in the polymer structure. Comparing the ultrasound processed PET with the PET control, as shown in Figure 54, indicates that the shear modulus of PET at higher frequencies increased for lower (3.5 µm and 5 µm) ultrasound amplitudes. Additionally, the modulus at lower frequencies increased for samples without (0 µm) and at 7.5 µm ultrasound amplitude conditions. Based on the data from Figure 53 and Figure 54, the ultrasound amplitude of 5 µm was found to have less effect on PET, while also indicating an improvement in the dispersion of graphene nanoplatelets.

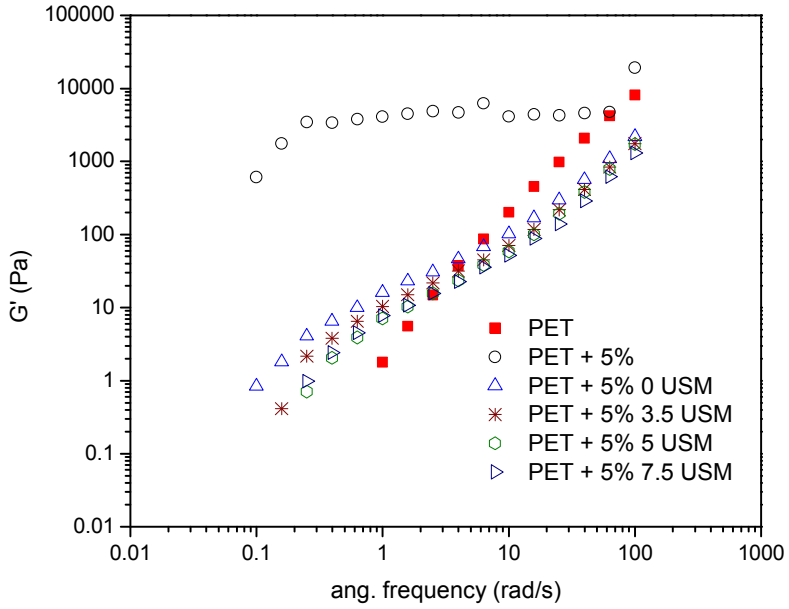

Figure 53: Storage modulus of ultrasound nanocomposites compared with PET and twin-screw nanocomposite.

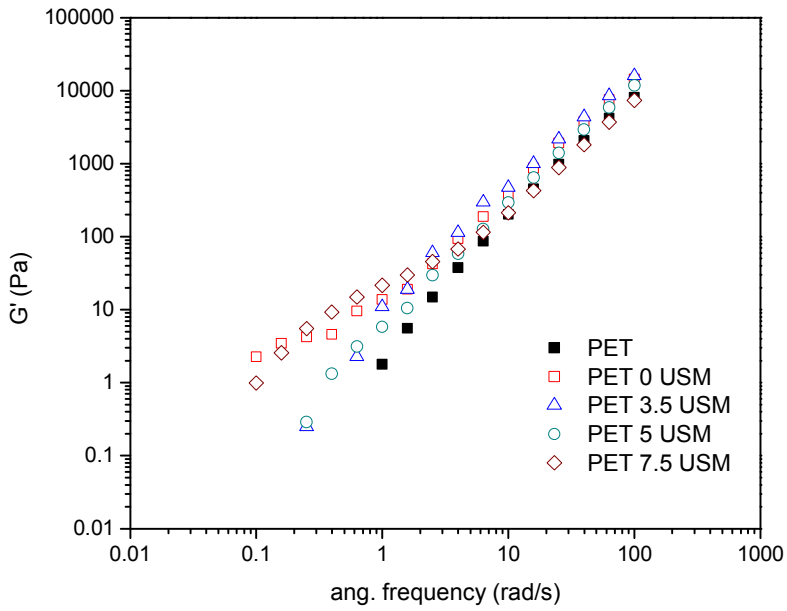

Figure 54: Dynamic sweep of storage moduli for different PET samples.

4.8.2. Transmission Electron Microscopy

Transmission micrographs were collected for nanocomposite tensile bars of 5% and 15% weight fraction. Even though there are few layered graphene (Figure 56), transmission micrographs of the nanocomposites indicate that the graphene nanoplatelets are not completely exfoliated in the PET matrix. Micrographs shown in Figure 55 indicate that the nanoplatelets are distributed in the matrix, with regions of high concentration.

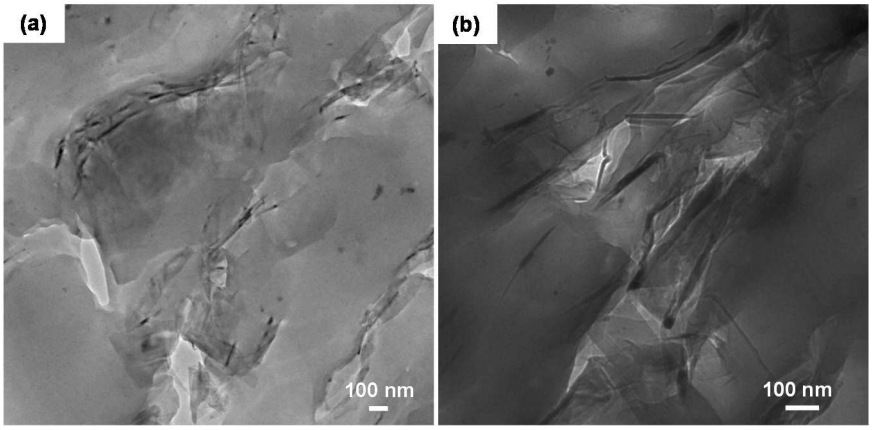

Figure 55: Transmission micrographs of 15% nanocomposite.

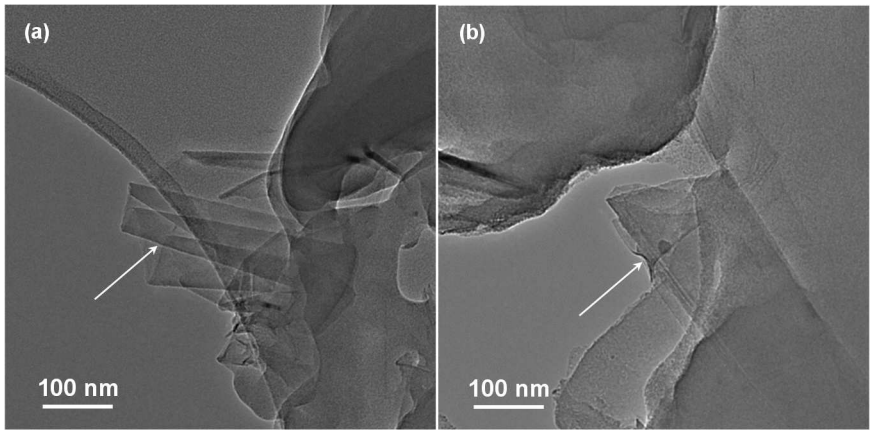

Figure 56: Transmission micrographs of 5% nanocomposite, showing few layer graphene.

Average dimensions (thickness and length) of the nanoplatelets obtained from TEM micrographs were used as input parameters to evaluate micromechanical models. The interparticle distance for graphene nanoplatelets inside the PET matrix was determined using binarized TEM images. Converting the micrographs to binary images allowed separating the nanoplatelets (darker regions) from the polymer matrix, as seen from Figure 57. Interparticle distance for 5% and 15% nanocomposites were determined as 2800 nm and 520 nm respectively, as shown in Figure 58.

This change in the interparticle distance can be because of the increase in concentration of graphene nanoplatelets, which can affect the dispersion. Theoretical interparticle distance for graphene nanoplatelets of known aspect ratio 40 (obtained from rheological measurements), were plotted against the calculated values based on TEM, in Figure 58.

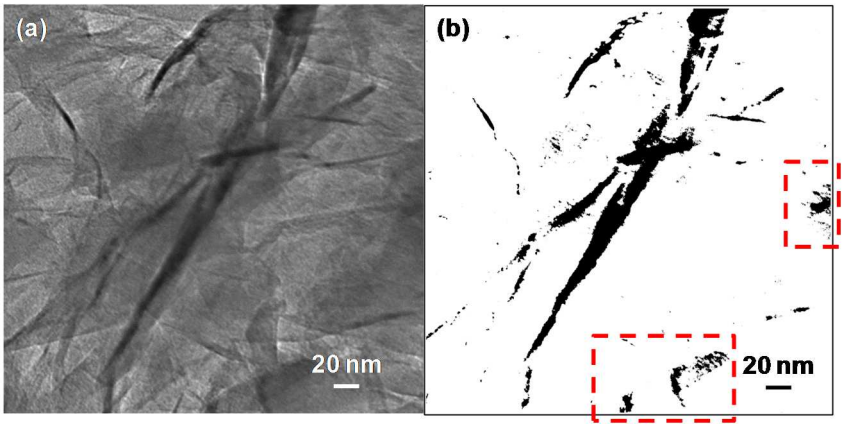

Figure 57: (a) Transmission electron micrograph of 15% PET-GNP nanocomposite and (b) binarized micrograph used for analyzing the interparticle distance (Artifacts, similar to the regions marked were excluded from the analysis).

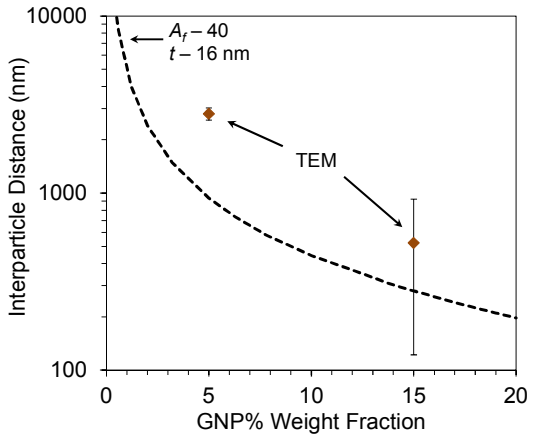

Figure 58: Interparticle distance vs. GNP weight fraction, experimental data compared with theoretical trend (dashed line).

4.8.3. X-ray Diffraction

Diffraction patterns acquired from the graphene nanoplatelets, PET, and PET-GNP nanocomposite tensile bars are shown in Figure 59. Peak broadening observed for the graphene peak at 26.6° 2θ is indicative of the presence of platelets with different *d*-spacing. The intensity of the graphene peak at 26.6° 2θ increased with weight fraction of the nanoplatelets. However, no peak shift was observed as in the case of an exfoliated nanocomposite. PET and nanocomposite tensile bars exhibit a broad amorphous halo around 19.2° 2θ.

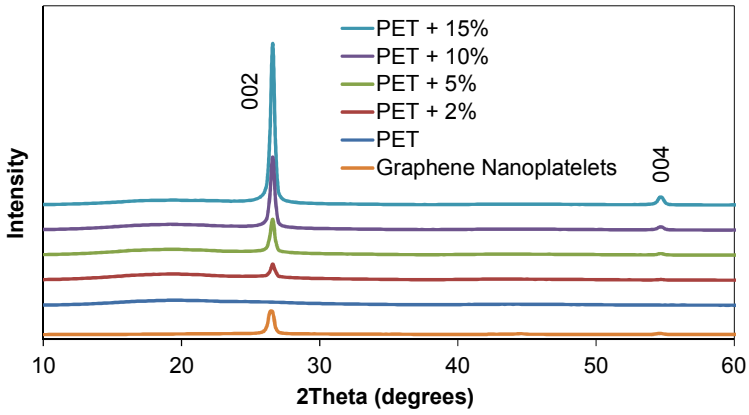

Figure 59: XRD patterns for GNPs, PET and nanocomposite tensile bars [172].

Diffraction scans indicate that the PET tensile bar is amorphous. However, density measurements and visual observations contradict this. Therefore, diffraction scans were collected across the cross-section of the PET tensile bar, to confirm the presence of a crystalline core with an amorphous outer layer. Slower cooling rates during the oil cooled injection molding process result in the formation of a significantly different skin and core microstructure. Data from the diffraction line scan along the thickness are presented in Figure 60. In order to have a better understanding on the microstructure of the nanocomposites, a similar line scan was performed along the thickness of the 15% tensile bar, presented in Figure 61. It was observed that intensity of the graphene peak changes along the thickness of the sample, with higher intensity at the

center. Further, crystallization of PET was also observed towards the core of the sample (blue arrows pointed in Figure 61).

Diffraction analysis on the nanocomposite tensile tubes indicate a completely amorphous microstructure and addition of GNPs did not increase the crystallization of PET. 2D diffraction frames indicate that the GNPs are oriented at the surface due to the injection flow stresses.

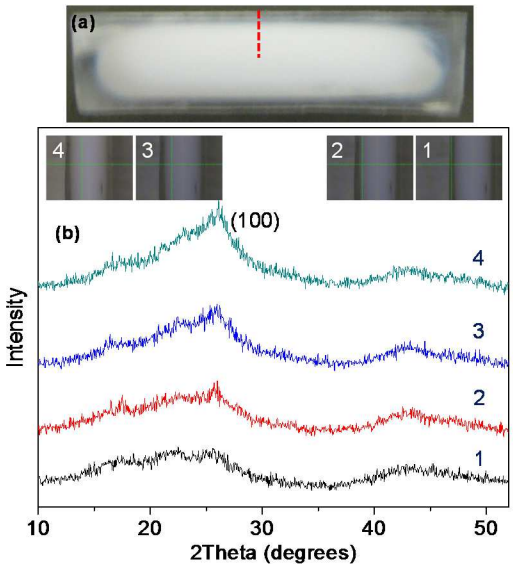

Figure 60: (a) Cross-section of PET tensile bar, (b) diffraction patterns from line scan [17].

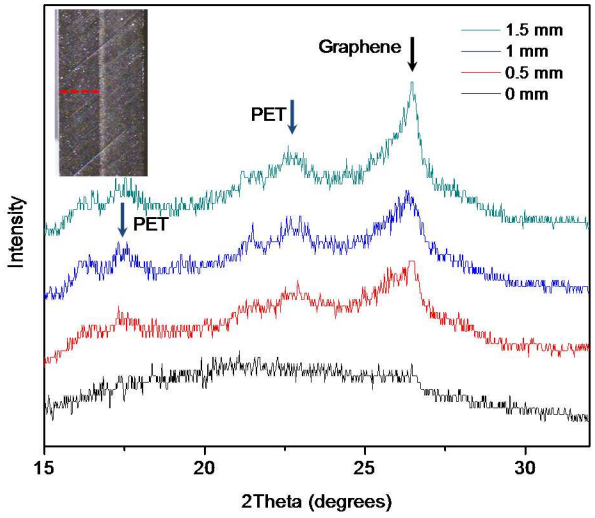

Figure 61: Diffraction patterns along the thickness of the 15% nanocomposite tensile bar (legend – distance from the surface, sample thickness - 3mm).

4.8.4. X-ray Nanotomography

Using the reconstructed tomographs for the sample collected from the 15% nanocomposite tensile bar, the distribution of nanoplatelets inside the PET matrix was visualized as shown in Figure 62. Based on observations from the reconstructed volume, nanoplatelets were found to be oriented along the flow direction about 200 μm in depth from surface (along the Y-axis direction). Nanoplatelets with random orientation and curved platelets as well were observed from this data.

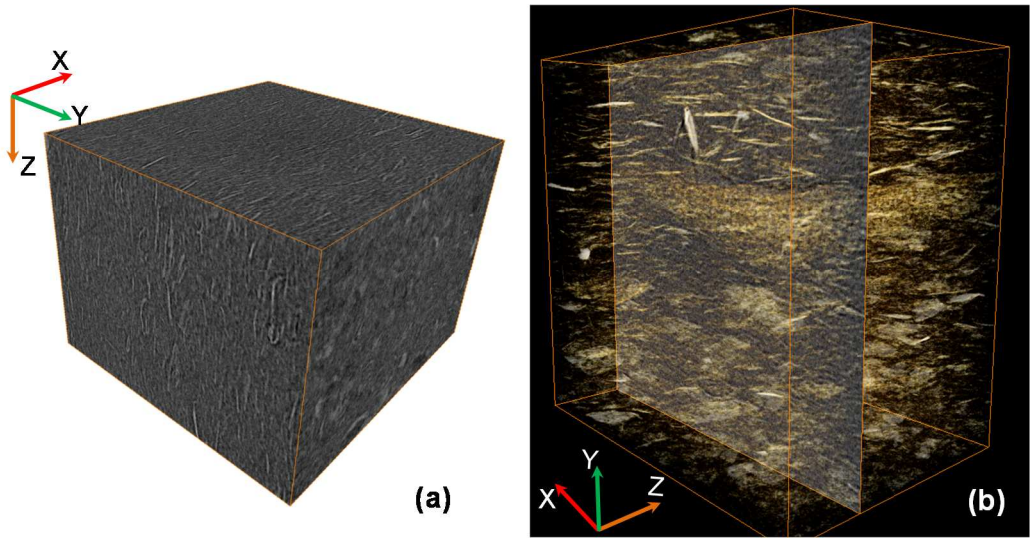

Figure 62: (a) Reconstructed 3D volume of the 15% nanocomposite (bounding box size - 240 µm × 240 µm × 163 µm), (b) nanoplatelets inside the nanocomposite indicate orientation of platelets along the injection flow direction (indicated with 'Z').

3D X-ray microscopy of the samples (wedge shape) collected from the nanocomposite tensile tube has shown that the extent of nanoplatelet orientation was smaller than in the tensile bar. Figure 63 shows the 3D distribution of the nanoplatelets on the inside surface of the tensile tube. As seen from the picture, nanoplatelets are oriented in the flow direction, parallel to the surface only up to 15.6 µm in thickness. For the outside surface, alignment with the flow was limited to a 7.5 µm thickness.

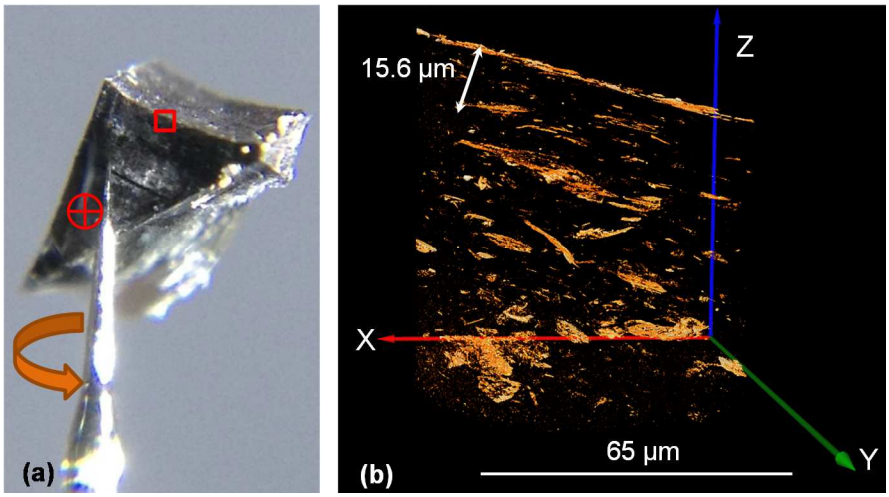

Figure 63: (a) Sample mounted on a rotating pin (cross mark indicates injection flow direction) and (b) distribution of nanoplatelets from the inside edge of a 2% nanocomposite tensile tube.

4.9. Raman Spectroscopy of PET-Graphene

Raman spectrum for PET and PET nanocomposites were collected to analyze the dispersion of graphene nanoplatelets. The Raman spectrums indicate that the nanoplatelets dispersed in to the PET matrix are multi layered. As stated earlier, Raman spectroscopy can also be used to determine the presence of π-π interactions between PET and graphene layers. Figure 64 shows the Raman bands (~1617 cm^{-1}) corresponding to C─C stretching for PET and nanocomposites with increasing GNP content. A change in the band positions determined from peak fits can be observed in Figure 65. This shift in the Raman band (~1617 cm^{-1}) corresponding to C─C stretching in the phenyl ring of PET is an indication of the interaction with graphene. Further, the full width at half maximum for the Raman band corresponding to C═O stretching (~1730 cm^{-1}) was evaluated to understand the effect graphene has on PET chain mobility. Peak broadening for the 1730 cm^{-1} Raman band (C═O stretching), perceived to be an indicator for chain mobility in amorphous PET was not observed here. This can be due to the highly oriented structure at the surface of the tensile bars obtained from injection molding. Even though the surface is

amorphous for these nanocomposites, the highly oriented structure will reduce the probability of having multiple chain rotations thereby limiting the band width [186].

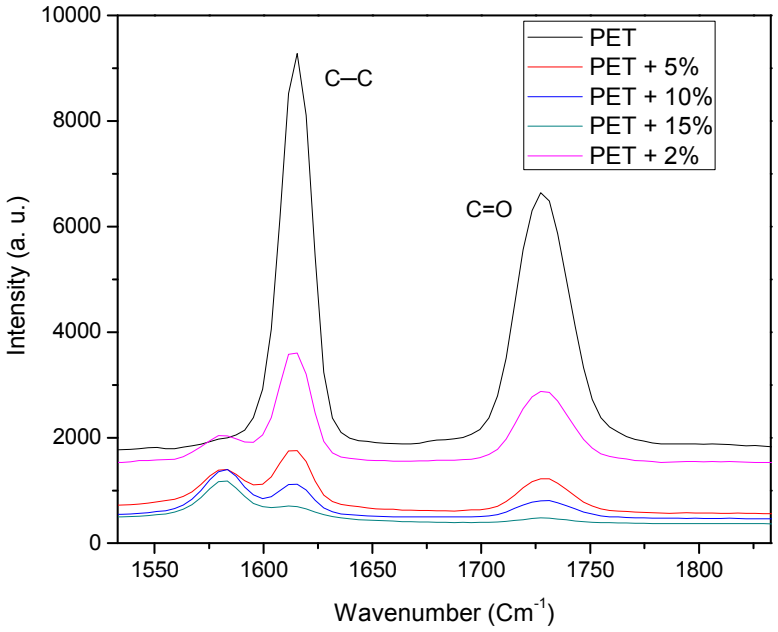

Figure 64: Raman bands corresponding to C─C stretching for PET and PET nanocomposites.

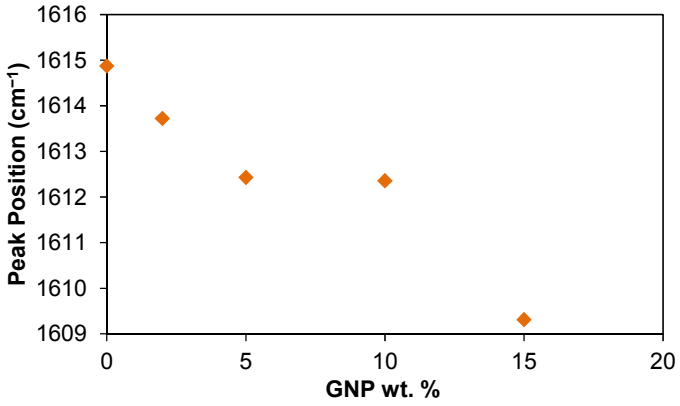

Figure 65: Shift in the Raman band corresponding to C─C stretching with increase in GNP weight fraction.

4.10. Micromechanical Modeling

Single layer graphene is known for its high strength and stiffness. Nevertheless, dispersing graphene nanoplatelets solely into single layer graphene was not realized here. Some fraction of the mixture is likely single layer, but a majority was not. Studies on multi-layer graphene showed that when the number of layers is less than 10, properties are similar to that of a single layer [196]. In the case of nanoplatelets with more than a few layers, its mechanical behavior was found to be similar to a graphite flake [74, 77]. For that reason, the modulus of the graphene nanoplatelet was considered to be 0.795 TPa, similar to highly oriented graphite [74, 77].

Table 13: Properties of GNP and PET used for micromechanical model based predictions.

Graphene Nanoplatelet				PET
Average Length/Diameter (D) nm (min/max)	Average Thickness (t) nm (min/max)	Aspect Ratio (D/t)	Modulus (GPa) Blakslee *et al.*	Modulus (GPa)
300 (28/730)	16 (3/26)	18.75	795	2.7 ± 0.2

Improvement in the properties of a nanocomposite depends on the extent of nanoplatelet dispersion. Based on the measurements from TEM micrographs, graphene nanoplatelets with different length (diameter of the platelets) and thickness were observed. Table 13 shows the average size of the platelets with minimum and maximum values. Predicted moduli of the nanocomposite from Halpin-Tsai and Hui-Shia micromechanical models are plotted against the experimental results, as shown in Figure 66. In order to compare with the moduli from nanocomposite tensile bars, modulus of semi-crystalline PET obtained from PET tensile bars was used as the model input properties. Using the average platelet properties and their standard deviations, modulus limits for the nanocomposites were calculated. Upper and lower limits for the predicted modulus are presented in Figure 66 by means of error bars. Comparison of the

modulus data from with experimental data indicate that Hui-Shia model predictions are close to the experimental values.

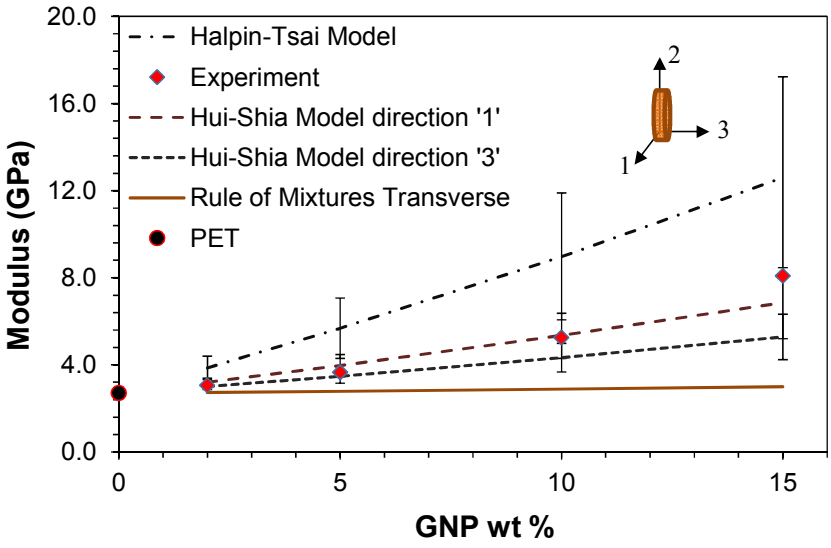

Figure 66: Modulus of PET-Graphene nanocomposites from predictions compared with experimental results [197].

Using the Hui-Shia model for nanoplatelets loaded along the length (i.e. in direction '1 or 2') of the nanoplatelets, the nanocomposite modulus with respect to platelet aspect ratios were plotted as shown in Figure 67. Modulus data for nanoplatelet aspect ratios from TEM measurements (average and the upper limit), melt rheology, and for an ideal dispersion condition (single layer graphene) were plotted. Based on the micromechanical model, it was observed that the predicted properties are more sensitive to nanoplatelets aspect ratio than their properties. For ideal dispersion condition, modulus of graphene single layer 1.02 TPa was used. Modulus of amorphous PET obtained from injection molded tensile tubes was used for the model data shown in Figure 67.

Comparing the experimental modulus with the predicted modulus indicate that the nanocomposites with lower GNP weight fractions have higher aspect ratios. For nanocomposites

(0.5%, 0.6%, and 1.2%) prepared through a dilution of the masterbatch (as mentioned in Table 7), it was observed that masterbatches with low GNP content yielded higher aspect ratios. This can be explained by considering the gentler processing seen when diluting a masterbatch which was done with a single screw rather than a twin screw.

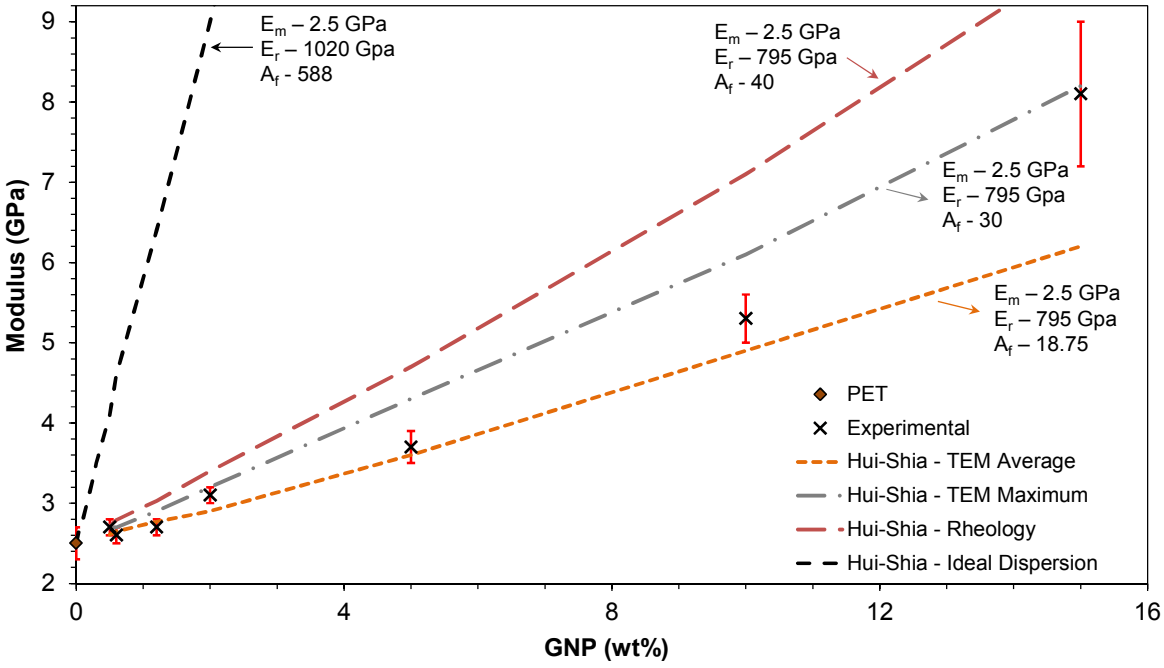

Figure 67: Comparison of nanocomposites experimental behavior with the Hui-Shia model for different nanoplatelet aspect ratios (E_m – modulus of matrix, E_r – modulus of GNP, A_f (aspect ratio) – diameter/thickness).

CHAPTER V

DISCUSSION

Poly(ethylene terephthalate) – graphene nanoplatelet nanocomposites were prepared through injection molding. Masterbatch pellets from conventional and ultrasound-assisted twin-screw compounding were characterized for their mechanical and thermal properties. In this chapter, effect of ultrasound treatment on PET properties, interaction between graphene and PET, mechanics behind the change in properties, effect of compounding and injection molding on composite properties, and the applicability of micromechanical models in evaluating the nanocomposites were discussed.

5.1. Effect of Ultrasound Treatment on PET

Ultrasound-assisted extrusion was used in the current study to disperse graphene nanoplatelets in the PET matrix. With no literature available to understand the effect of ultrasound on PET, ultrasound treated PET was also analyzed here. During ultrasound-assisted extrusion, energy applied (in the form of ultrasound waves) to the polymer can increase the melt temperature locally as a result of acoustic cavitation [114]. Cavitation will not only aid in exfoliating the nanoplatelets, but can also potentially change the polymer. The average molecular weight from the GPC measurements of ultrasound treated PET indicates that the molecular weight decreased with increasing ultrasound amplitude.

However, decrease in the molecular weight was also observed in case of PET from conventional twin-screw process. Based on the data shown in Figure 26, it is understood that the decrease in molecular weight is primarily from the extrusion process (15%), whereas ultrasound treatment has a minimal (5% drop) effect on the molecular weight.

Mechanical testing of the ultrasound treated PET did not show a significant difference in Young's modulus and tensile strength (Figure 35). However, ultrasound treated specimens did show an improvement in ultimate strength (strength at break) and exhibited higher toughness compared to PET control, as seen from Figure 36 and Figure 68.

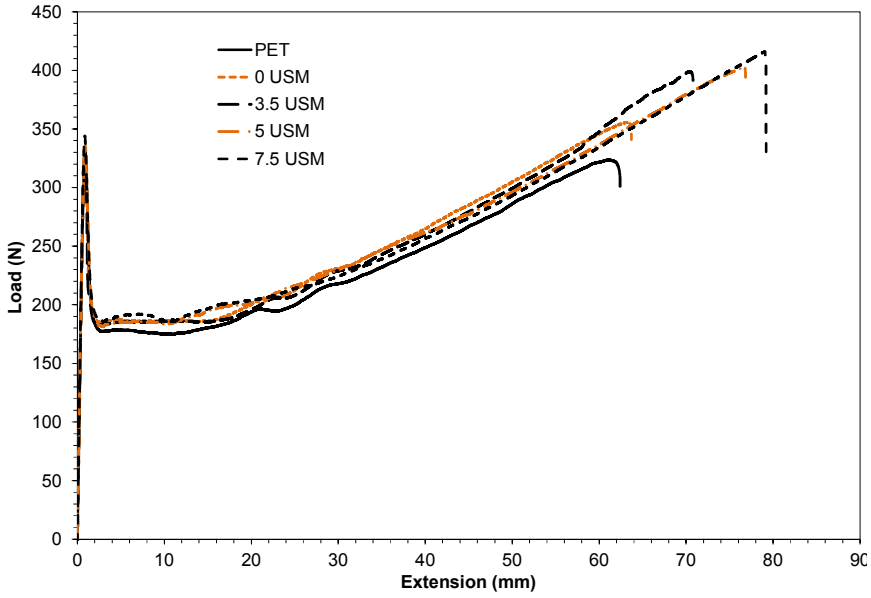

Figure 68: Load extension curves for ultrasound treated PET compared with PET control.

PET degradation involves three different processes. They are: hydrolysis, thermal degradation and oxidation. During the extrusion process, polymer degradation can take place through one or more abovementioned processes and result in chain scission. Some condensation reaction can also occur, which lengthens the chain. An increase in the toughness of PET from ultrasound treatment indicates that ultrasound altered the PET molecular chains. Thermal analysis (DSC and Rheology) of the ultrasound treated PET hints at entanglement through branching of PET.

Entanglement of polymer chains result in an increase in the shear modulus (G′) at lower frequencies as shown in Figure 54. This also explains the increase in the 'T_g' for PET treated at 7.5 μm amplitude. Polymer with lower molecular weight (shorter chain length) exhibits a lower glass transition temperature, when compared with a high molecular weight grade. Then again, presence of entanglements (cross-linking or chain branching) will restrict the chain mobility, therefore increases the glass transition temperature. As the drop in the molecular weight at 7.5 μm amplitude is less significant compared to other amplitudes; increase in the glass transition temperature can be primarily due to the presence of entanglements in PET molecular chain.

Similar observations of an increase in the breaking strength were reported in case of PET polymerized with low levels of branching agent Trimethyl Trimellitate (TMT) [198]. At low levels (< 0.4%) of branching agent there is a significant increase (25%) in the ultimate strength, even without any sign of crosslinking from GPC measurements.

5.2. Wettability and Interaction of Graphene with PET

In the selection of nanoreinforcements, compatibility with the polymer is an important factor. Two polymers are considered compatible (or miscible to form homogenous mixtures) when the difference in their surface energies is small. An increase in the difference in surface energies can lead to phase separation. Likewise, similar surface energies between the polymer and its nanoreinforcement aids in dispersion. PET is slightly polar due to the presence of the C═O bond in the molecular chain. PET's surface energy is 41.1 mJ/m^2 [199]. Graphene's surface energy is 46.7 mJ/m^2 [70]. Through graphene is hydrophobic, it's surface energy is closer to PET than graphene oxide (62.1 mJ/m^2) and graphite (54.8 mJ/m^2) [70]. This places graphene as a more compatible nanoreinforcement for PET. In general, dispersing graphene (as individual sheets) into any polymer matrix is considered difficult as it shows a tendency to agglomerate to minimize its surface energy. Therefore, applying external energy through different mixing techniques is

necessary to disrupt agglomerates and distribute them into the polymer matrix. PET is a highly viscous polymer with a high melting temperature. This drove the selection of twin-screw and ultrasound-assisted twin-screw mixing techniques for the dispersion of graphene nanoplatelets.

PET is chemically inert except for strong alkali solvents. Therefore, PET does not react with pristine graphene. However, graphene (similar to CNTs) is known to have non-covalent interactions with aromatic compounds due to π-π stacking of benzene with graphene [130, 200, 201]. While graphene sheets inside graphite have similar aromatic-aromatic (π-π) interactions, their energy is estimated (~8×10^{11} eV/cm^2 [202]) to be lower than that of a graphene-benzene system (~8.4×10^{14} eV/ cm^2 [200]). Bjork *et al*. [130] found that the magnitude of the π-π interaction increases with increase in the density of hydrogen atoms in the graphene-aromatic molecule system (stronger dipoles). This explains the difference in binding energy for the graphene-benzene interaction compared to a graphene-graphene interaction.

PET is an aromatic polyester with a nearly planar molecular chain configuration [48]. This makes it more favorable for the π-π interaction with graphene nanoplatelets. The presence of the π-π interaction between PET and graphene nanoplatelets is observed as a Raman peak shift, corresponding to C─C stretching in phenyl ring (Figure 65). In addition, graphene nanoplatelets used in this work had a low concentration of polar functional groups such as, hydroxyl, carboxyl and ether on the edges (Figure 8). Polar groups of the nanoplatelets are likely to interact with polar groups of PET [145]. The aforementioned interactions between PET and graphene are advantageous in influencing the properties of the nanocomposite.

5.3. Stress Transfer between PET and Graphene

PET-GNP nanocomposites showed an improvement in Young's modulus (Figure 31). This increase in modulus of the nanocomposites is due to the effective transfer of stresses from PET to GNPs. For such a stiff reinforcement, load transfer between the polymer and reinforcement is

governed by the strength of its interface, which is directly proportional to the thermodynamic work of adhesion (W_a) [46]. Adhesion energy between PET and graphene is 84.6 mJ/m^2, according to the Equation 17 [203]. The total surface energy of graphene is 46.7 mJ/m^2 [70]. The polar and non-polar components of PET's surface energy are 2.7 mJ/m^2 and 38.4 mJ/m^2 [46].

$$W_a = 2\sqrt{\gamma_p^{LW}\gamma_g^{LW}} + 2\sqrt{\gamma_P^{AB}\gamma_g^{AB}} \quad (17)$$

Where, γ^{LW} - Lifshitz-van der Waals (non-polar or dispersion) component of surface energy, γ^{AB} - Lewis acid-base (polar) component of surface energy, for polymer and graphene, and $\gamma = \gamma^{LW} + \gamma^{AB}$.

Jiang *et al*. [204] quantified the interfacial shear strength as 0.46 to 0.69 MPa for a pristine single layer graphene (no polar group interactions) in contact with a PET substrate (other surface of graphene in contact with air). Therefore, interfacial strength for the nanocomposites in the current work is likely to be higher than 0.69 MPa. Aoyama *et al.* [205] found that the interfacial adhesion of PET with clay is stronger than with graphene nanoplatelets. However, they also reported that nanoplatelets disperse well in PET, compared to clay.

An increase in weight fraction of GNPs resulted in a decrease of the interparticle distance, quantified from TEM micrographs as shown in Figure 58. For nanocomposites with 15% loading, the interparticle distance was determined as 520 nm. This is large when compared to the interparticle distance of 200 nm reported for 2% graphene (with higher surface area, 750 m^2/g) [167]. Higher interparticle distance indicates better nanoplatelets dispersion. As nanoplatelets interparticle distance decreases, the number of polymer chains influenced by nanoplatelets will increase (as shown in Figure 69). This increase in the volume of nanoplatelet-affected-polymer results in a stiffer composite. As observed from Figure 70, with an increase in GNP weight

fraction, the modulus of the nanocomposite showed an exponential trend. This behavior clearly depicts that load sharing of GNPs increased with increase in weight fraction.

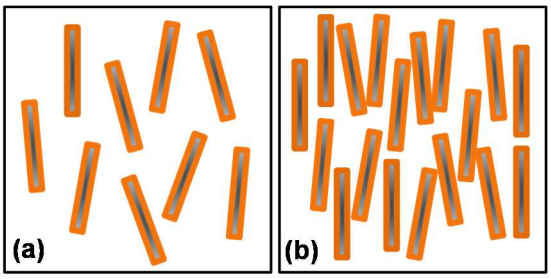

Figure 69: Schematic showing the change in nanoplatelets affected the polymer matrix with a doubling of platelets of same size (orange rectangle shows the affected zone).

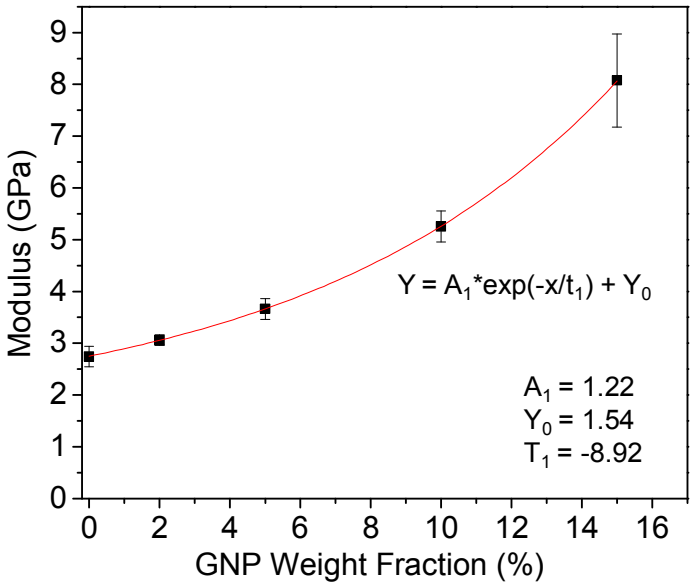

Figure 70: Increase in elastic tensile modulus with respect to GNP weight fraction.

At higher weight fractions of GNPs, the stress-strain curves have shown a more complex yielding behavior (Figure 71). Platelet-platelet interaction is not likely to happen at low weight fractions. Not only is the platelet volume fraction, the platelet surface area at that volume fraction also

important. Higher volume fractions of low surface area platelets are expected to have a similar benefit as lower volume fractions of high surface area platelets. However, eventually, the platelets begin to interact across the matrix and that interaction will impact yielding behavior. Platelet-platelet bonding is much weaker than platelet-matrix bonding. In this study, a more pronounced evidence of this interaction was observed above 10% volume fraction platelets.

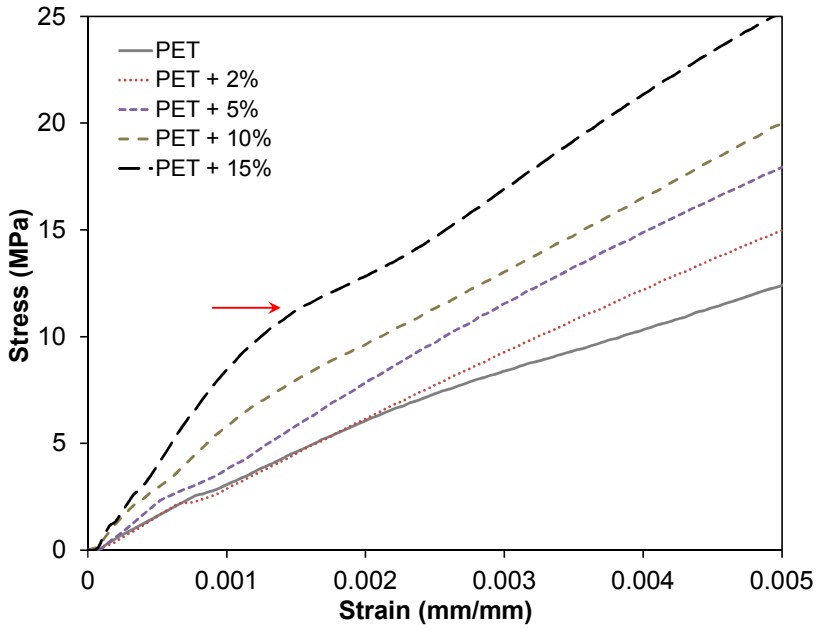

Figure 71: Elastic region of the stress-strain curves for nanocomposite tensile bars.

5.4. Nanocomposites Microstructure and Application of Micromechanical Models

Micromechanical models based on Hui-Shia formulae have closely predicted the nanocomposite properties compared to Halpin-Tsai. In the beginning they were developed to model the properties of semi-crystalline polymers by considering the crystalline domains as a reinforcement phase in an amorphous matrix. These micromechanical models were later adapted to model micro-composites. Key assumptions for the abovementioned models are: uniform interface between the polymer and reinforcement, orientation of the reinforcement along the loading direction, and uniform aspect ratio of the reinforcement. Nevertheless, nanoplatelets dispersed in

the nanocomposites are not completely oriented along the loading axis (injection direction), as observed from nanotomography (Figure 62 and Figure 63b). For instance, in nanocomposite tensile bars GNP orientation due to flow stresses was witnessed only to a 200 μm depth from surface, whereas in the case of tensile tubes this was less (15 μm depth from surface). This shows that the bulk of the nanocomposite has randomly oriented nanoplatelets. Increases in the injection molding speed and the cooling rate resulted in limited nanoplatelet orientation.

During injection molding, polymer melt flowing through the mold channels experiences shear forces. This shearing action is due to the temperature gradient induced by the low temperature mold walls. As the polymer melt starts solidifying (in thickness), increasing shear forces produce a layered structure along the thickness, with highly oriented layers on the outer surface. Some have speculated that this layer would be 0.1 mm thick. The rate of cooling determines the thickness of the oriented layers. Nanotomography allows quantifying the thickness of the skin layers and this is a first of its kind observation of this layer. As observed with the tensile tube, the difference in the oriented layer thickness is likely due to the more effective cooling rate from the curvature of the surface and the mold design. Comparing the tensile tube data with the tensile bar data shows that the thickness of the oriented surface layer is higher in the tensile bar. This is consistent with the slower cooling and injection speed compared to the tensile tube. This difference in the oriented layer thickness can affect the final properties of the nanocomposite.

One of the observations from nanotomography was that the aspect ratio of platelets was not uniform for the nanocomposite. The aspect ratio of the nanoplatelets from rheological measurements and transmission electron microscopy were determined to be 40 and 18.75. Taking these as limits on the aspect ratios, moduli of the nanocomposites were predicted. Comparing the experimental data with predicted modulus trends for different aspect ratios (shown in Figure 67) highlighted that the nanocomposites have different average aspect ratios and this aspect ratio increased with increase in GNP weight fraction.

Graphene nanoplatelets used in this work are of an average diameter (length) of 5 μm. This dimension is much lower than the size of pristine graphene estimated (30 μm) by Gong *et al.* [206] to effectively reinforce poly(methyl methacrylate) (PMMA). Kim *et al*. [181] indicated that graphene with reduced stiffness (drop in modulus from 1000 GPa to 100 GPa) will be less effective in reinforcing glassy polymers (e.g. PET) compared to elastomers. As mentioned earlier, graphene with more than 10 layers can have reduced stiffness. The aforementioned factors reinforce the need to have detailed information on the microstructure of nanocomposites for the application of micromechanical models to predict properties.

5.5. Effect of Graphene Nanoplatelets on PET Properties and Molecular Chain Mobility

The nanocomposite tensile bars from oil cooled molding exhibited around 20% crystallinity. Using a high-speed injection molding system with a faster cooling rate, nanocomposite tensile tubes were prepared with better control on the crystallization of PET during injection molding. Through this process, nanocomposites with GNP weight fractions from 0.5% to 2% were prepared and tested. Comparing the modulus of nanocomposites with 2% GNP (Figure 31 and Figure 33), from both the processes (water cooled and oil cooled injection molding), showed an improved modulus in case of water cooling. For the tensile tubes with 2% GNP, the modulus increased from 2.5 GPa (amorphous modulus of PET) to 3.1 GPa (7% higher than tensile bars). Another important observation was that the presence of voids in the 2% nanocomposite has little effect on its modulus. On the other hand, the presence of voids (from processing) resulted in premature failure and a reduction of strength. As observed from the SEM micrographs of nanocomposite fracture surfaces (Figure 40 and Figure 41), the voids acted as stress concentration points and led to failure. The nanocomposite tensile tubes at low GNP weight fractions exhibited a minimal increase in strength (Figure 33).

Addition of GNPs at low weight fractions (< 2%) showed minimal effect on strength of the PET (Figure 72). This is expected since the weight fraction is low and the matrix will dominate flow behavior typical for yielding. It is also helpful to realize that the lack of chemical linkage (bonding) between PET and GNP reduces the GNP influence on yielding. As discussed in earlier sections, interfacial interactions between PET and GNPs are favorable for initial stress transfer. With increase in strain, interfacial sliding starts between PET and GNPs [204], this precludes GNPs from sharing the failure load. As strength of the material depends on the weakest element, the nanocomposite strength remained similar to PET at low GNP weight fractions.

Stress-strain curves from mechanical testing show that nanocomposites up to 2% GNP weight fraction are tougher than PET (with increased failure strain). As PET failure take place as a result of the through thickness propagation of surface crazes, the presence of graphene nanoplatelets in PET matrix can act against it through crack deflection. Nanoplatelets extending out of the fracture surface, as observed from the SEM micrographs in Figure 42, support the above observation.

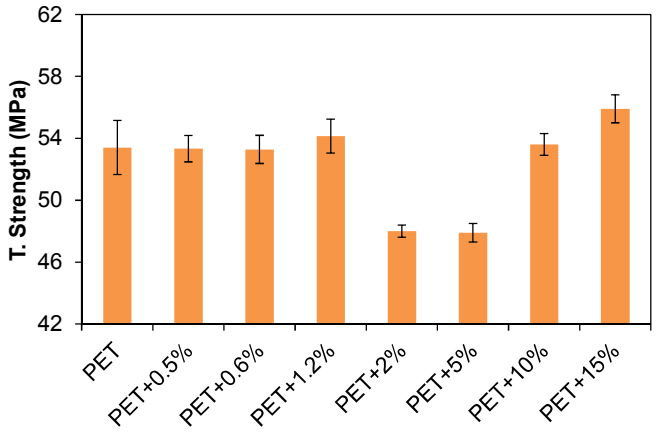

Figure 72: Tensile strength of nanocomposite molded using the twin-screw compounded pellets.

At 2% GNP weight fraction, nanocomposite tensile strength dropped by 10% compared to PET. In addition to the strength drop, a ductile to brittle failure transition was observed for the nanocomposites. Increase in the GNP weight fractions will result in the development of a continuous network (as represented in Figure 69) that changed the deformation behavior of PET. The GNP weight fraction at which this change in failure type and strength loss was observed correlates with the measured percolation limit. It is inferred from rheology and thermal analysis data that the presence of graphene nanoplatelets at higher weight fractions influences the mobility of PET molecular chain. This illustrates that the presence of GNP network affected the yielding behavior of PET, by restricting chain mobility. On the other hand, for nanocomposites with 10% and 15% GNP weight fractions, tensile strength recovery was observed. This can be explained by the increase in the fraction of polymer that interacted with GNPs, as shown in Figure 69.

Using Raman spectroscopy, Aoyama *et al*. [167] has observed that increase in graphene concentration will restrict the mobility of PET chains. Raman spectrum shown in section 4.9 (Figure 64), did not show change in peak width, as the nanocomposites from injection molding exhibited highly oriented amorphous surface layer. Oriented PET chains will limit the number of chain configurations possible, thereby restricting the rotation of C═O isomers and suppressing peak broadening.

Thermal analysis of the nanocomposites showed that the addition of GNPs affected PET crystallization. Graphene nanoplatelets acted as nucleation sites and promoted PET crystallization, as observed with increase in the crystallization temperature. However, increase in the nanoplatelet fraction reduced PET chain mobility (confinement effect) and counteracted the nucleation effect. A combination of these opposing effects led to the increase in crystallization half-time and decreased the amount of crystallinity (Figure 45). As the interparticle distance became smaller with increase in the GNP weight fraction, chain mobility becomes more restricted. This elucidates the change in the failure type of PET nanocomposites, as discussed

earlier for higher GNP weight fractions (above 2%). Aoyama *et al*. [167] has made similar observations with PET and high aspect ratio graphene at less than 2% weight fractions. They found that crystallization half-time decreased till graphene loading less than 2% and started increasing at 2%.

5.6. Effect of Ultrasound Treatment on PET-Graphene Nanocomposites

Comparing the mechanical properties for nanocomposites prepared using twin-screw and ultrasound-assisted compounded batches (presented in Figure 38), aided in identifying the best mixing approach. It was observed that the ultrasound amplitudes of 5 μm and 7.5 μm showed the maximum improvement in terms of modulus. However, this improvement in modulus is not significantly different compared to nanocomposites from twin-screw compounding. This indicates that the ultrasound treatment did not provide an advantage in improving the mechanical properties of nanocomposites. Molecular weight data for 5% graphene nanocomposite pellets from both the process indicate a similar drop in the PET average molecular weight (Figure 26). Additionally, it is observed that the presence of graphene increased the drop in molecular weight from extrusion process. This could be due to the high thermal conductivity of graphene nanoplatelets, which allows faster heating of PET and cause chain damage under regular heating conditions.

Rheology of the ultrasound treated nanocomposites showed similar behavior as observed in ultrasound treated PET (Figure 53 and Figure 54). The decrease in the shear modulus at high frequency is due to the damage of the polymer chains (molecular weight). Increase in the shear moduli at lower frequency could be from an increase in entanglement due to ultrasound treatment and the presence of dispersed graphene. Higher ultrasound amplitudes show lower shear modulus; this suggests a better dispersion of GNPs at higher amplitudes. However, for the 7.5 μm ultrasound amplitude, the drop in molecular weight is higher compared to other amplitudes.

Ultrasound-assisted dispersion of graphene has shown a difference in the thermal properties of the nanocomposites compared to regular twin-screw injection (for the same graphene weight fraction). Evaluating the glass transition temperature, crystallization half-time, and percent crystallinity, shown in Figure 47 and Figure 49, pointed at better graphene dispersion at 7.5 μm ultrasound amplitude over other amplitudes. The crystallization half-time of PET decreases with the decrease in the molecular weight. Thus a decrease in the crystallization half-time was expected for nanocomposites with 7.5 μm amplitude ultrasound treatment. However, increase in the crystallization half-time is possibly because of the improved graphene dispersion at 7.5 μm amplitude. These observations along with the melt rheology data (Figure 53 and Figure 54) suggest that ultrasound amplitude of 7.5 μm is likely to have improved the dispersion of GNPs. However, this improvement in dispersion observed from thermal analysis did not reflect in the mechanical data.

During the ultrasound treated nanocomposites in to tensile bars using the micro injection molding system, the effect of mixing time on the mechanical properties was investigated. Nanocomposite samples were injection molded for each of the following process times: 1 min, 2 min and 3 min. Modulus data, shown in Figure 73, indicate that longer mixing times decreased the nanocomposite modulus. This could be due to the damage of polymer from longer residence times.

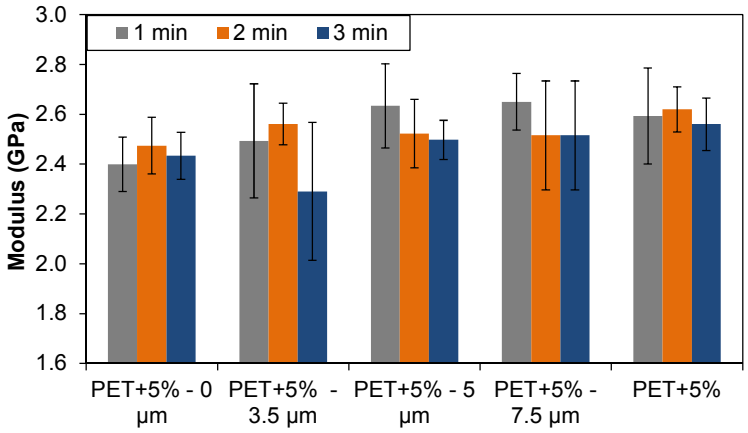

Figure 73: Comparison of Young's modulus for PET-GNP nanocomposites with and without ultrasound treated (legend – micro compounder mixing time).

5.7. Effect of Graphene Surface Area on PET Nanocomposite Properties.

In-situ polymerized PET nanocomposites suggest that the graphene nanoplatelets surface area play a significant role in influencing the crystallization behavior of PET. Coming to the mechanical properties of the nanocomposites, their difference is not significant enough to make a conclusion. Nanoplatelets dispersed through sonication will contain platelets of different dimensions, giving rise to a broad distribution of nanoplatelet aspect ratios, changing the average surface area available. The application of a size selective approach, through centrifugation will help in understanding the effect of the nanoplatelet surface area.

As mentioned earlier, one of the draw back for *in-situ* polymerization is achieving similar molecular weight polymer between different batches. This indicates that polymerization process is not alone sufficient for the producing nanocomposites; application of secondary techniques such as solid state polymerization can help in addressing the disparity in molecular weights.

5.8. Effectiveness of Graphene as Reinforcement

The mechanical behavior of PET is dependent on the type of crystallinity: spherulitic and stretch crystallization. The modulus of a PET crystal was calculated to be 146 GPa [49], based on the deformation of the covalent bonds in PET. One approach in improving the properties of PET is to increase its crystallinity from processing methods. PET film samples obtained through biaxial stretching show 5.4 GPa at 45% crystallinity. Comparing that with the nanocomposites, the modulus for only 10% GNP weight fraction was 5.3 GPa. With a reinforcement that is 5.5 times stiffer than a PET crystal, the improvement with GNP addition is comparable to that of self-reinforced (stretch crystalized) PET. For the same biaxial stretched sample, when tested along the maximum molecular orientation direction showed about a 9.1 GPa modulus. This indicates that inducing orientation to graphene nanoplatelets during the processing of nanocomposites could improve the properties further.

CHAPTER VI

CONCLUSIONS

PET-GNP nanocomposites were demonstrated using injection molding. These nanocomposites were evaluated for dispersion, mechanical, and thermal properties. The following conclusions were deduced:

The Young's modulus of the nanocomposites increased with GNP weight fraction and displayed an exponential trend, while the strength showed minimal improvement.

The improvement in Young's modulus was at a minimum of 8% for 0.5% GNP weight fraction to a maximum of 224% for a 15% GNP weight fraction.

Selection of the molding method played a significant role in influencing the final properties of the nanocomposite. Nanocomposites made from high speed injection molding yielded better properties (improved modulus).

The masterbatch approach proved to be effective in improving the dispersion of nanoplatelets. A masterbatch with lower GNP content yielded better dispersion over higher GNP content masterbatches.

Ultrasound treatment of PET is found to increase its toughness, with minimal effect on molecular weight and no effect on Young's modulus.

Ultrasound-assisted twin-screw compounding was not advantageous for improving the mechanical properties of PET-GNP nanocomposites. They exhibited similar improvement in Young's modulus compared to twin-screw compounding.

The presence of aromatic-aromatic (π-π) interaction between PET and graphene nanoplatelets was demonstrated using Raman spectroscopy.

The addition of graphene nanoplatelets above 2% weight fraction was found to affect the failure strain of PET.

Dispersion analysis on the nanocomposites from twin-screw compounding indicated an average nanoplatelet aspect ratio (l/d ratio) of 18. The interparticle distance for GNPs decreased with increase in their concentration (520 nm for 15% nanocomposite).

PET nanocomposites prepared through injection molding, demonstrated preferential orientation of the graphene nanoplatelets in flow direction up to a maximum depth of 200 μm from the mold surface. The thickness of the oriented layer is dependent on cooling rate.

A comparison of the experimental Young's modulus with the Hui-Shia micromechanical model illustrates that the nanocomposites exhibited different nanoplatelet aspect ratios and are far from a completely exfoliated state.

The addition of GNPs affects the crystallization behavior of PET. The crystallization temperature increased with additional nucleation from graphene. The crystallization half-time ($t_{1/2}$) increased with increasing GNP content.

Rheological percolation for twin-screw compounded pellets was found to be 1.75% weight fraction.

CHAPTER VII

FUTURE WORK

Poly(ethylene terephthalate) – graphene nanocomposites prepared here demonstrated improved Young's modulus. However, enhancement of modulus is still lower compared to the theoretical modulus indicating scope for improvement. The current study has pointed the following approaches to maximize the advantage of graphene as reinforcement; they are: increasing the nanoplatelet effective surface area and increasing the orientation of nanoplatelets along the loading direction. For instance, micromechanical model data (in Figure 73) shows that the aspect ratio (effective surface area) of the nanoplatelet is influential in determining the nanocomposite properties. Nanocomposites obtained by the polymerization of graphene dispersed ethylene glycol, highlight the influence of nanoplatelet surface area on the crystallization behavior of PET (Figure 50), while not improving mechanically. Currently, graphene with different surface areas are available through different manufacturing approaches. Preparing nanocomposites with graphene nanoplatelets of different surface areas can help in understanding the change in properties as a function of surface area.

During the injection molding process, cooling induced stresses in the melt have shown that the nanoplatelets can be aligned with the flow (Figure 62 and Figure 63(b)). Further, it was observed that the extent (depth from surface) of nanoplatelet alignment is influenced by the rate of cooling. Therefore, by studying the change in the oriented layer thickness as a function of cooling rate can

help in designing nanocomposites with improved properties.

Crystallinity of PET is influenced by rate of cooling (thermally) and the amount of stretching (mechanically). Compared to thermally-induced crystallization, strain-induced crystallization is effective in improving mechanical properties of PET [17, 18]. Thermal crystallinity studies presented in this work shows that when graphene weight fraction is less than 2%, the crystallization rate increases. Effect of graphene on strain-induced crystallization behavior of PET has not been understood. Studying the effect of graphene addition and the alignment of PET chains in the presence of graphene will be valuable in expanding their applications.

REFERENCES

[1] D. D. L. Chung, "Composite Material Structure and Processing," in *Composite Materials: Science and Applications*, Second Edition ed London: Springer-Verlag, 2009, p. 1.

[2] J. William D. Callister, *Fundamentals of Materials Science and Engineering*, 5th ed. New York: John Wiley & Sons, Inc., 2001.

[3] P. M. Ajayan, L. S. Schadler, and P. V. Braun, *Nanocomposite Science and Technology*. Weinheim: Wiley-VCG Verlag, 2003.

[4] F. L. Carter, "Chemistry and microstructures: Fabrication at the molecular size level," *Superlattices and Microstructures,* vol. 2, pp. 113-128, 1986.

[5] L. W. Carter, J. G. Hendricks, and D. S. Bolley, "Elastomer reinforced with a modified clay," US Patent 2531396, 1950.

[6] C. Ortiz and M. C. Boyce, "Bioinspired Structural Materials," *Science,* vol. 319, pp. 1053-1054, February 22, 2008 2008.

[7] R. Lakes, "Materials with structural hierarchy," *Nature,* vol. 361, pp. 511-515, 11 February 1993.

[8] A. C. Balazs, T. Emrick, and T. P. Russell, "Nanoparticle Polymer Composites: Where Two Small Worlds Meet," *Science,* vol. 314, pp. 1107-1110, November 17, 2006 2006.

[9] R. A. Vaia and H. D. Wagner, "Framework for nanocomposites," *Materials Today,* vol. 7, pp. 32-37, 2004.

[10] A. Usuki, M. Kawasumi, Y. Kojima, A. Okada, T. Kurauchi, and O. Kamigaito, "Swelling behavior of montmorillonite cation exchanged for w-amino acids by e-caprolactam," *Journal of Materials Research,* vol. 8, pp. 1174-1178, 1992.

[11] R. Gangopadhyay and A. De, "Conducting Polymer Nanocomposites: A Brief Overview," *Chemistry of Materials,* vol. 12, pp. 608-622, 2000/03/01 2000.

[12] S. J. Savage, "Defence applications of nanocomposite materials," Swedish Defence Research Agency, Linkoping2004.

[13] S. Clara, D. Donatella, and C. Sossio, "Food packaging based on polymer nanomaterials," *Progress in Polymer Science,* vol. 36, 2011.

[14] M.-H. Chen, C.-R. Chen, S.-H. Hsu, S.-P. Sun, and W.-F. Su, "Low shrinkage light curable nanocomposite for dental restorative material," *Dental Materials,* vol. 22, pp. 138-145, 2006.

[15] D. R. Paul and L. M. Robeson, "Polymer nanotechnology: Nanocomposites," *Polymer,* vol. 49, pp. 3187-3204, 2008.

[16] S. Ates, "Global PET and Raw Materials Outlook," in *The Packaging Conference*, 2012.

[17] S. Bandla, M. Allahkarami, and J. C. Hanan, "Thermal crystallinity and mechanical behavior of Polyethylene Terephthalate," in *Challenges in Mechanics of Time-Dependent Materials*. vol. 2, ed: Springer, 2014, pp. 141-146.

[18] S. Bandla, M. Allahkarami, and J. C. Hanan, "Out of plane orientation and crystallinity of biaxially stretched Polyethylene terephthalate," *Powder Diffraction,* vol. 29, pp. 123-126, 2014.
[19] S. Bandla, "Evaluation and Stability of PET Resin Mechanical Properties," Master of Science, Mechanical and Aerospace Engineering, Oklahoma State University, 2010.
[20] K. Anoop Anand, U. S. Agarwal, and R. Joseph, "Carbon nanotubes induced crystallization of poly(ethylene terephthalate)," *Polymer,* vol. 47, pp. 3976-3980, 5/17/ 2006.
[21] D. W. Brooks, "Barrier Materials and Technology," in *PET Packaging Technology*, D. W. Brooks and G. A. Giles, Eds., ed: CRC Press, 2002, pp. 98-115.
[22] Y. Ke, C. Long, and Z. Qi, "Crystallization, properties, and crystal and nanoscale morphology of PET–clay nanocomposites," *Journal of Applied Polymer Science,* vol. 71, pp. 1139-1146, 1999.
[23] Y. Imai, S. Nishimura, E. Abe, H. Tateyama, A. Abiko, A. Yamaguchi*, et al.*, "High-Modulus Poly(ethylene terephthalate)/Expandable Fluorine Mica Nanocomposites with a Novel Reactive Compatibilizer," *Chemistry of Materials,* vol. 14, pp. 477-479, 2002/02/01 2002.
[24] M. Frounchi and A. Dourbash, "Oxygen Barrier Properties of Poly(ethylene terephthalate) Nanocomposite Films," *Macromolecular Materials and Engineering,* vol. 294, pp. 68-74, 2009.
[25] H. Ma, J. Zeng, M. L. Realff, S. Kumar, and D. A. Schiraldi, "Processing, structure, and properties of fibers from polyester/carbon nanofiber composites," *Composites Science and Technology,* vol. 63, pp. 1617-1628, 8// 2003.
[26] Q. Ji, X. Wang, Y. Zhang, Q. Kong, and Y. Xia, "Characterization of Poly (ethylene terephthalate)/SiO2 nanocomposites prepared by Sol–Gel method," *Composites Part A: Applied Science and Manufacturing,* vol. 40, pp. 878-882, 2009.
[27] J. Zhang, Q. Ji, P. Zhang, Y. Xia, and Q. Kong, "Thermal stability and flame-retardancy mechanism of poly(ethylene terephthalate)/boehmite nanocomposites," *Polymer Degradation and Stability,* vol. 95, pp. 1211-1218, 2010.
[28] M. Parvinzadeh, S. Moradian, A. Rashidi, and M.-E. Yazdanshenas, "Surface characterization of polyethylene terephthalate/silica nanocomposites," *Applied Surface Science,* vol. 256, pp. 2792-2802, 2010.
[29] T. Wan, L. Chen, Y. C. Chua, and X. Lu, "Crystalline morphology and isothermal crystallization kinetics of poly(ethylene terephthalate)/clay nanocomposites," *Journal of Applied Polymer Science,* vol. 94, pp. 1381-1388, 2004.
[30] A. Ghanbari, M. C. Heuzey, P. J. Carreau, and M. T. Ton-That, "A novel approach to control thermal degradation of PET/organoclay nanocomposites and improve clay exfoliation," *Polymer,* vol. 54, pp. 1361-1369, 2/18/ 2013.
[31] D. Bikiaris, "Can nanoparticles really enhance thermal stability of polymers? Part II: An overview on thermal decomposition of polycondensation polymers," *Thermochimica Acta,* vol. 523, pp. 25-45, 8/20/ 2011.
[32] S. Sathyanarayana and C. Hübner, "Thermoplastic Nanocomposites with Carbon Nanotubes," in *Structural Nanocomposites*, J. Njuguna, Ed., ed: Springer Berlin Heidelberg, 2013, pp. 19-60.
[33] S. Park and R. S. Ruoff, "Chemical methods for the production of graphenes," *Nat Nano,* vol. 4, pp. 217-224, 2009.
[34] "xGnP Graphene Nanoplatelets - Grade M - Technical Data Sheet," X. S. Inc., Ed., ed: XG Sciences Inc., 2013.
[35] C. L. Choy and D. Greig, "The low-temperature thermal conductivity of a semi-crystalline polymer, polyethylene terephthalate," *Journal of Physics C: Solid State Physics,* vol. 8, p. 3121, 1975.

[36] E. Neagu, P. Pissis, and L. Apekis, "Electrical conductivity effects in polyethylene terephthalate films," *Journal of Applied Physics,* vol. 87, pp. 2914-2922, 2000.
[37] S. Paszkiewicz, A. Szymczyk, Z. Špitalský, M. Soccio, J. Mosnáček, T. A. Ezquerra*, et al.*, "Electrical conductivity of poly(ethylene terephthalate)/expanded graphite nanocomposites prepared by in situ polymerization," *Journal of Polymer Science Part B: Polymer Physics,* vol. 50, pp. 1645-1652, 2012.
[38] I. M. Inuwa, A. Hassan, S. A. Samsudin, M. K. M. Haafiz, M. Jawaid, K. Majeed*, et al.*, "Characterization and mechanical properties of exfoliated graphite nanoplatelets reinforced polyethylene terephthalate/polypropylene composites," *Journal of Applied Polymer Science,* pp. n/a-n/a, 2014.
[39] H. Hu, L. Onyebueke, and A. Abatan, "Characterizing and Modeling Mechanical Properties of Nanocomposites-Review and Evaluation," *Journal of Minerals & Materials Characterization & Engineering,* vol. 9, pp. 275-319, 2010.
[40] J. R. Potts, "Preparation, Properties, and Structure-Property Relationships of Graphene-Polymer Nanocomposites," Doctor of Philosophy, Mechanical Engineering, University of Texas at Austin, 2012.
[41] M. W. A. Kuijpers, P. D. Iedema, M. F. Kemmere, and J. T. F. Keurentjes, "The mechanism of cavitation-induced polymer scission; experimental and computational verification," *Polymer,* vol. 45, pp. 6461-6467, 9/3/ 2004.
[42] M. M. Caruso, D. A. Davis, Q. Shen, S. A. Odom, N. R. Sottos, S. R. White*, et al.*, "Mechanically-Induced Chemical Changes in Polymeric Materials," *Chemical Reviews,* vol. 109, pp. 5755-5798, 2009/11/11 2009.
[43] J. C. Halpin and J. L. Kardos, "The Halpin-Tsai equations: A review," *Polymer Engineering & Science,* vol. 16, pp. 344-352, 1976.
[44] C. Y. Hui and D. Shia, "Simple formulae for the effective moduli of unidirectional aligned composites," *Polymer Engineering & Science,* vol. 38, pp. 774-782, 1998.
[45] D. Shia, C. Y. Hui, S. D. Burnside, and E. P. Giannelis, "An interface model for the prediction of Young's modulus of layered silicate-elastomer nanocomposites," *Polymer Composites,* vol. 19, pp. 608-617, 1998.
[46] C. Wan and B. Chen, "Reinforcement and interphase of polymer/graphene oxide nanocomposites," *Journal of Materials Chemistry,* vol. 22, pp. 3637-3646, 2012.
[47] J. Scheirs and T. E. Long, *Modern Polyesters: chemistry and technology of polyesters and copolyesters*: John Wiley and Sons, 2003.
[48] R. de P. Daubeny, C. W. Bunn, and C. J. Brown, "The Crystal Structure of Polyethylene Terephthalate," *Proceedings of the Royal Society of London. Series A. Mathematical and Physical Sciences,* vol. 226, pp. 531-542, 1954.
[49] W. J. Lyons, "Theoretical Values of the Dynamic Stretch Moduli of Fiber□Forming Polymers," *Journal of Applied Physics,* vol. 29, pp. 1429-1433, 1958.
[50] X. L. Jiang, S. J. Luo, K. Sun, and X. D. Chen, "Effects of nucleating agents on crystallization kinetics of PET," *eXPRESS Polymer Letters,* vol. 1, pp. 245-251, 2007.
[51] D. Kim, S. Srivastava, S. Narayanan, and L. A. Archer, "Polymer nanocomposites: polymer and particle dynamics," *Soft Matter,* vol. 8, pp. 10813-10818, 2012.
[52] H. Fukushima, "Graphite Nanoreinforcements in Polymer Nanocomposites," Doctor of Philosophy Dissertation, Chemical Engineering and Materials Science, 2003.
[53] X. Jiang and L. T. Drzal, "Multifunctional high density polyethylene nanocomposites produced by incorporation of exfoliated graphite nanoplatelets 1: Morphology and mechanical properties," *Polymer Composites,* vol. 31, pp. 1091-1098.
[54] K. K. Nanda, A. Maisels, F. E. Kruis, H. Fissan, and S. Stappert, "Higher Surface Energy of Free Nanoparticles," *Physical Review Letters,* vol. 91, p. 106102, 2003.
[55] M. I. Katsnelson, "Graphene: carbon in two dimensions," *Materials Today,* vol. 10, pp. 20-27, 2007.

[56] M. S. Mauter and M. Elimelech, "Environmental Applications of Carbon-Based Nanomaterials," *Environmental Science & Technology,* vol. 42, pp. 5843-5859, 2008/08/01 2008.
[57] H. W. Kroto, J. R. Heath, S. C. O'Brien, R. F. Curl, and R. E. Smalley, "C60: Buckminsterfullerene," *Nature,* vol. 318, pp. 162-163, 1985.
[58] S. Iijima, "Helical microtubules of graphitic carbon," *Nature,* vol. 354, pp. 56-58, 1991.
[59] K. S. Novoselov, A. K. Geim, S. V. Morozov, D. Jiang, Y. Zhang, S. V. Dubonos*, et al.*, "Electric Field Effect in Atomically Thin Carbon Films," *Science,* vol. 306, pp. 666-669, October 22, 2004 2004.
[60] G. Etxebarria, M. Gomez-Uranga, and J. Barrutia, "Tendencies in scientific output on carbon nanotubes and graphene in global centers of excellence for nanotechnology," *Scientometrics,* vol. 91, pp. 253-268, 2012/04/01 2012.
[61] A. K. Geim and K. S. Novoselov, "The rise of graphene," *Nat Mater,* vol. 6, pp. 183-191, 2007.
[62] A. Bondi, "van der Waals Volumes and Radii," *The Journal of Physical Chemistry,* vol. 68, pp. 441-451, 1964/03/01 1964.
[63] K. S. Novoselov, V. I. Falko, L. Colombo, P. R. Gellert, M. G. Schwab, and K. Kim, "A roadmap for graphene," *Nature,* vol. 490, pp. 192-200, 2012.
[64] A. K. Geim, "Graphene prehistory," *Physica Scripta,* vol. 2012, p. 014003, 2012.
[65] T. Kuilla, S. Bhadra, D. Yao, and N. Kim, "Recent advances in graphene based polymer composites," *Progress in Polymer Science,* vol. 35, pp. 1350-1375, 2010.
[66] L. Itzhaki, E. Altus, H. Basch, and S. Hoz, "Harder than Diamond: Determining the Cross-Sectional Area and Young's Modulus of Molecular Rods," *Angewandte Chemie,* vol. 117, pp. 7598-7601, 2005.
[67] C. Lee, X. Wei, J. W. Kysar, and J. Hone, "Measurement of the Elastic Properties and Intrinsic Strength of Monolayer Graphene," *Science,* vol. 321, pp. 385-388, 2008.
[68] K. V. Zakharchenko, M. I. Katsnelson, and A. Fasolino, "Finite Temperature Lattice Properties of Graphene beyond the Quasiharmonic Approximation," *Physical Review Letters,* vol. 102, p. 046808, 01/29/ 2009.
[69] A. A. Balandin, "Thermal properties of graphene and nanostructured carbon materials," *Nat Mater,* vol. 10, pp. 569-581, 2011.
[70] S. Wang, Y. Zhang, N. Abidi, and L. Cabrales, "Wettability and Surface Free Energy of Graphene Films," *Langmuir,* vol. 25, pp. 11078-11081, 2009/09/15 2009.
[71] R. R. Nair, P. Blake, A. N. Grigorenko, K. S. Novoselov, T. J. Booth, T. Stauber*, et al.*, "Fine Structure Constant Defines Visual Transparency of Graphene," *Science,* vol. 320, p. 1308, June 6, 2008 2008.
[72] S. Ghosh, W. Bao, D. L. Nika, S. Subrina, E. P. Pokatilov, C. N. Lau*, et al.*, "Dimensional crossover of thermal transport in few-layer graphene," *Nat Mater,* vol. 9, pp. 555-558, 2010.
[73] Y. Y. Zhang and Y. T. Gu, "Mechanical properties of graphene: Effects of layer number, temperature and isotope," *Computational Materials Science,* vol. 71, pp. 197-200, 2013.
[74] S. K. Georgantzinos, G. I. Giannopoulos, and N. K. Anifantis, "Numerical investigation of elastic mechanical properties of graphene structures," *Materials & Design,* vol. 31, pp. 4646-4654, 2010.
[75] A. R. Golkarian and M. Jabbarzadeh, "The density effect of van der Waals forces on the elastic modules in graphite layers," *Computational Materials Science,* vol. 74, pp. 138-142, 2013.
[76] L. Gong, R. J. Young, I. A. Kinloch, I. Riaz, R. Jalil, and K. S. Novoselov, "Optimizing the Reinforcement of Polymer-Based Nanocomposites by Graphene," *ACS Nano,* vol. 6, pp. 2086-2095, 2012/03/27 2012.

[77] O. L. Blakslee, D. G. Proctor, E. J. Seldin, G. B. Spence, and T. Weng, "Elastic Constants of Compression-Annealed Pyrolytic Graphite," *Journal of Applied Physics,* vol. 41, pp. 3373-3382, 1970.
[78] C. Mattevi, H. Kim, and M. Chhowalla, "A review of chemical vapour deposition of graphene on copper," *Journal of Materials Chemistry,* vol. 21, pp. 3324-3334, 2011.
[79] Y. Zhu, S. Murali, W. Cai, X. Li, J. W. Suk, J. R. Potts*, et al.*, "Graphene and Graphene Oxide: Synthesis, Properties, and Applications," *Advanced Materials,* vol. 22, pp. 3906-3924, 2010.
[80] M. Terrones, "Materials science: Nanotubes unzipped," *Nature,* vol. 458, pp. 845-846, 2009.
[81] L. J. Cote, R. Cruz-Silva, and J. Huang, "Flash Reduction and Patterning of Graphite Oxide and Its Polymer Composite," *Journal of the American Chemical Society,* vol. 131, pp. 11027-11032, 2009/08/12 2009.
[82] X. Li, W. Cai, J. An, S. Kim, J. Nah, D. Yang*, et al.*, "Large-Area Synthesis of High-Quality and Uniform Graphene Films on Copper Foils," *Science,* vol. 324, pp. 1312-1314, June 5, 2009 2009.
[83] S. Stankovich, D. A. Dikin, R. D. Piner, K. A. Kohlhaas, A. Kleinhammes, Y. Jia*, et al.*, "Synthesis of graphene-based nanosheets via chemical reduction of exfoliated graphite oxide," *Carbon,* vol. 45, pp. 1558-1565, 2007.
[84] X. Li, X. Wang, L. Zhang, S. Lee, and H. Dai, "Chemically Derived, Ultrasmooth Graphene Nanoribbon Semiconductors," *Science,* vol. 319, pp. 1229-1232, February 29, 2008 2008.
[85] A. T. S. Wee, "Graphene: The Game Changer?," *ACS Nano,* vol. 6, pp. 5739-5741, 2012/07/24 2012.
[86] L. T. Drzal, "Graphene Nanoplatelets: A Multifunctional Nanomaterial for Polymers, Composites and Energy Generation and Storage Applications," presented at the Nanotech 2012, Santa Clara, CA, 2012.
[87] R. J. Young, I. A. Kinloch, L. Gong, and K. S. Novoselov, "The mechanics of graphene nanocomposites: A review," *Composites Science and Technology,* vol. 72, pp. 1459-1476, 2012.
[88] J. J. Winnink, "Searching for structural shifts in science: Graphene R&D before and after Novoselov et al. (2004)," Leiden University, Leiden, Netherlands2012.
[89] P. I. Team, "An Analysis of Worldwide Patent Filings Relating to Graphene," Intellectual Property Office, Newport, UK2011.
[90] M. Taghioskoui, "Trends in graphene research," *Materials Today,* vol. 12, pp. 34-37, 2009.
[91] (2011, 5/5/2013). *Commercialization of Graphene*. Available: http://nextbigfuture.com/2011/04/commercialization-of-graphene.html
[92] A. K. Kaushik, "Deformation Mechanisms in Polymer-Clay Nanocomposites," Doctor of Philosophy Dissertation, Mechanical Engineering, University of Michigan, Ann Arbor, 2010.
[93] S. J. Mun, Y. M. Jung, J.-C. Kim, and J.-H. Chang, "Poly(ethylene terephthalate) nanocomposite fibers with functionalized multiwalled carbon nanotubes via <I>in-situ</I> polymerization," *Journal of Applied Polymer Science,* vol. 109, pp. 638-646, 2008.
[94] A. S. Patole, S. P. Patole, H. Kang, J.-B. Yoo, T.-H. Kim, and J.-H. Ahn, "A facile approach to the fabrication of graphene/polystyrene nanocomposite by in situ microemulsion polymerization," *Journal of Colloid and Interface Science,* vol. 350, pp. 530-537, 2010.
[95] P. Lekakou, P. Wilson, D. Craggs, Y. C. Chau, A. A. Salifu, Y. L. Chen*, et al.*, "Electrospinning of Polymer Nanocomposites," in *ICCM-17*, Edinburgh, Scotland, 2009.

[96] S. Bandla, R. P. Winarski, and J. Hanan, "Nanotomography of Polymer Nanocomposite Nanofibers," in *Imaging Methods for Novel Materials and Challenging Applications*. vol. 3, H. Jin, C. Sciammarella, C. Furlong, and S. Yoshida, Eds., ed: Springer, 2013, pp. 193-198.
[97] T. A. Osswald, L.-S. Turng, and P. Gramann, *Injection Molding Handbook*, 2 ed. Cincinnati: Hanser Gardner Publications, Inc., 2008.
[98] R. Krishnamoorti, "Strategies for Dispersing Nanoparticles in Polymers," *MRS Bulletin,* vol. 32, pp. 341-347, 2007.
[99] M. C. Costache, M. J. Heidecker, E. Manias, and C. A. Wilkie, "Preparation and characterization of poly(ethylene terephthalate)/clay nanocomposites by melt blending using thermally stable surfactants," *Polymers for Advanced Technologies,* vol. 17, pp. 764-771, 2006.
[100] U. Gurmendi, J. I. Eguiazabal, and J. Nazabal, "Structure and Properties of Nanocomposites with a Poly(ethylene terephthalate) Matrix," *Macromolecular Materials and Engineering,* vol. 292, pp. 169-175, 2007.
[101] Y. C. Li and G. H. Chen, "HDPE/expanded graphite nanocomposites prepared via masterbatch process," *Polymer Engineering & Science,* vol. 47, pp. 882-888, 2007.
[102] A. I. Isayev, R. Kumar, and T. M. Lewis, "Ultrasound assisted twin screw extrusion of polymer–nanocomposites containing carbon nanotubes," *Polymer,* vol. 50, pp. 250-260, 2009.
[103] C. Mahesha, "Investigation of Structure and Properties of Novel Multi-Layer Clay Nanocomposite Films Produced Controllably by Continuous Chaotic Advection Blending," Doctor of Philosophy, Materials Science and Engineering, Clemson University, 2007.
[104] K. Wakabayashi, C. Pierre, D. A. Dikin, R. S. Ruoff, T. Ramanathan, L. C. Brinson*, et al.*, "Polymer−Graphite Nanocomposites: Effective Dispersion and Major Property Enhancement via Solid-State Shear Pulverization," *Macromolecules,* vol. 41, pp. 1905-1908, 2008.
[105] X. Jiang and L. T. Drzal, "Reduction in percolation threshold of injection molded high-density polyethylene/exfoliated graphene nanoplatelets composites by solid state ball milling and solid state shear pulverization," *Journal of Applied Polymer Science,* vol. 124, pp. 525-535, 2012.
[106] D. Z. Chen, S. Lao, J. H. Koo, M. Londa, and Z. Alabdullatif, "Powder Processing and Properties Characterization of Polyamide 11-Graphene Nanocomposites for Selective Laser Sintering," in *21st Annual International Solid Freeform Fabrication Symposium*, Austin, TX, 2010.
[107] S. Anandhan and S. Bandyopadhyay, "Polymer Nanocomposites: From Synthesis to Applications," in *Nanocomposites and Polymer with Analytical Methods*, J. Cuppoletti, Ed., ed: InTech, 2001.
[108] X. Jiang and L. T. Drzal, "Improving electrical conductivity and mechanical properties of high density polyethylene through incorporation of paraffin wax coated exfoliated graphene nanoplatelets and multi-wall carbon nano-tubes," *Composites Part A: Applied Science and Manufacturing,* vol. 42, pp. 1840-1849, 2011.
[109] T. Wu and Y. Ke, "The absorption and thermal behaviors of PET–SiO2 nanocomposite films," *Polymer Degradation and Stability,* vol. 91, pp. 2205-2212, 2006.
[110] T.-D. Ngo, "Understanding the effect of adding nanoclays into epoxies," Doctor of Philosophy, Mechanical and Industrial Engineering, Concordia University, 2007.
[111] W. Liu, I. Do, H. Fukushima, and L. T. Drzal, "Influence of Processing on Morphology, Electrical Conductivity and Flexural Properties of Exfoliated Graphite Nanoplatelets-Polyamide Nanocomposites," *Carbon Letters,* vol. 11, pp. 279-284, 2010.

[112] A. Shah and M. Gupta, "Comparison of the flow in co-rotating and counter-rotating twin-screw extruders," in *ANTEC-2004*, Chicago, 2004, pp. 443-447.
[113] O. Behrend, K. Ax, and H. Schubert, "Influence of continuous phase viscosity on emulsification by ultrasound," *Ultrasonics Sonochemistry,* vol. 7, pp. 77-85, 2000.
[114] K. S. Suslick and G. J. Price, "APPLICATIONS OF ULTRASOUND TO MATERIALS CHEMISTRY," *Annual Review of Materials Science,* vol. 29, pp. 295-326, 1999/08/01 1999.
[115] K. Jungsoon, K. Moojoon, and H. Kanglyeol, "New ultrasonic dispersion method for nanoparticles using cylindrical piezoelectric transducer," in *Ultrasonics Symposium (IUS), 2010 IEEE*, 2010, pp. 2072-2075.
[116] T. M. Lewis and A. I. Isayev, "Continous High Power Ultrasonic Extrusion of PEEK - CNT Nanocomposites," in *ANTEC - 2013*, Cincinnati, OH, 2013, p. 6.
[117] J. Zhong and A. I. Isayev, "Preparation and Properties of Polyetherimide (PEI)/Graphite Composites with Ultrasound Assisted Extrusion," in *ANTEC-2013*, Cincinnati, OH, 2013, p. 8.
[118] T. Kuilla, S. Bhadra, D. Yao, N. H. Kim, S. Bose, and J. H. Lee, "Recent advances in graphene based polymer composites," *Progress in Polymer Science,* vol. 35, pp. 1350-1375, 2010.
[119] K. P. Loh, Q. Bao, P. K. Ang, and J. Yang, "The chemistry of graphene," *Journal of Materials Chemistry,* vol. 20, pp. 2277-2289, 2010.
[120] R. R. Nair, W. Ren, R. Jalil, I. Riaz, V. G. Kravets, L. Britnell*, et al.*, "Fluorographene: A Two-Dimensional Counterpart of Teflon," *Small,* vol. 6, pp. 2877-2884, 2010.
[121] D. C. Elias, R. R. Nair, T. M. G. Mohiuddin, S. V. Morozov, P. Blake, M. P. Halsall*, et al.*, "Control of Graphene's Properties by Reversible Hydrogenation: Evidence for Graphane," *Science,* vol. 323, pp. 610-613, January 30, 2009 2009.
[122] D. Li, M. B. Muller, S. Gilje, R. B. Kaner, and G. G. Wallace, "Processable aqueous dispersions of graphene nanosheets," *Nat Nano,* vol. 3, pp. 101-105, 2008.
[123] T. Ramanathan, A. Abdala, S. Stankovich, D. Dikin, M. Herrera-Alonso, R. Piner*, et al.*, "Functionalized graphene sheets for polymer nanocomposites," *Nature nanotechnology,* vol. 3, pp. 327-358, 2008.
[124] Y. Hernandez, V. Nicolosi, M. Lotya, F. M. Blighe, Z. Sun, S. De*, et al.*, "High-yield production of graphene by liquid-phase exfoliation of graphite," *Nat Nano,* vol. 3, pp. 563-568, 09//print 2008.
[125] U. Khan, A. O'Neill, M. Lotya, S. De, and J. N. Coleman, "High-Concentration Solvent Exfoliation of Graphene," *Small,* vol. 6, pp. 864-871, 2010.
[126] U. Khan, H. Porwal, A. O'Neill, K. Nawaz, P. May, and J. N. Coleman, "Solvent-Exfoliated Graphene at Extremely High Concentration," *Langmuir,* vol. 27, pp. 9077-9082, 2011/08/02 2011.
[127] U. Khan, A. O'Neill, H. Porwal, P. May, K. Nawaz, and J. N. Coleman, "Size selection of dispersed, exfoliated graphene flakes by controlled centrifugation," *Carbon,* vol. 50, pp. 470-475, 2// 2012.
[128] O. M. Istrate, K. R. Paton, U. Khan, A. O'Neill, A. P. Bell, and J. N. Coleman, "Reinforcement in melt-processed polymer–graphene composites at extremely low graphene loading level," *Carbon,* vol. 78, pp. 243-249, 11// 2014.
[129] M. Buzaglo, M. Shtein, S. Kober, R. Lovrincic, A. Vilan, and O. Regev, "Critical parameters in exfoliating graphite into graphene," *Physical Chemistry Chemical Physics,* vol. 15, pp. 4428-4435, 2013.
[130] J. Björk, F. Hanke, C.-A. Palma, P. Samori, M. Cecchini, and M. Persson, "Adsorption of Aromatic and Anti-Aromatic Systems on Graphene through π−π Stacking," *The Journal of Physical Chemistry Letters,* vol. 1, pp. 3407-3412, 2010/12/02 2010.

[131] S. D. Chakarova-Käck, E. Schröder, B. I. Lundqvist, and D. C. Langreth, "Application of van der Waals Density Functional to an Extended System: Adsorption of Benzene and Naphthalene on Graphite," *Physical Review Letters,* vol. 96, p. 146107, 04/14/ 2006.
[132] D. Konios, M. M. Stylianakis, E. Stratakis, and E. Kymakis, "Dispersion behaviour of graphene oxide and reduced graphene oxide," *Journal of Colloid and Interface Science,* vol. 430, pp. 108-112, 9/15/ 2014.
[133] Y. Liu, Zhizhongsu, X. Li, W. Guo, Q. Li, and C. Wu, "Effect of Dispersion of Carbon Black on Electrical and Thermal Properties of Poly(Ethylene Terephthalate)/Carbon Black Composites," *Journal of Macromolecular Science, Part B,* vol. 48, pp. 146-156, 2009/01/02 2008.
[134] M. D. Sanchez-Garcia, E. Gimenez, and J. M. Lagaron, "Novel PET Nanocomposites of Interest in Food Packaging Applications and Comparative Barrier Performance With Biopolyester Nanocomposites," *Journal of Plastic Film and Sheeting,* vol. 23, pp. 133-148, April 1, 2007 2007.
[135] X. Xu, Y. Ding, Z. Qian, F. Wang, B. Wen, H. Zhou*, et al.*, "Degradation of poly(ethylene terephthalate)/clay nanocomposites during melt extrusion: Effect of clay catalysis and chain extension," *Polymer Degradation and Stability,* vol. 94, pp. 113-123, 2009.
[136] L. V. Todorov and J. C. Viana, "Characterization of PET nanocomposites produced by different melt-based production methods," *Journal of Applied Polymer Science,* vol. 106, pp. 1659-1669, 2007.
[137] S. J. Mun, Y. M. Jung, J.-C. Kim, and J.-H. Chang, "Poly(ethylene terephthalate) nanocomposite fibers with functionalized multiwalled carbon nanotubes via in-situ polymerization," *Journal of Applied Polymer Science,* vol. 109, pp. 638-646, 2008.
[138] A. Anand K, U. S. Agarwal, and R. Joseph, "Carbon nanotubes-reinforced PET nanocomposite by melt-compounding," *Journal of Applied Polymer Science,* vol. 104, pp. 3090-3095, 2007.
[139] R. D. Averett, M. L. Realff, and K. I. Jacob, "The effects of fatigue and residual strain on the mechanical behavior of poly(ethylene terephthalate) unreinforced and nanocomposite fibers," *Composites Part A: Applied Science and Manufacturing,* vol. 40, pp. 709-723, 2009.
[140] P. Bhimaraj, H. Yang, R. W. Siegel, and L. S. Schadler, "Crystal nucleation and growth in poly(ethylene terephthalate)/alumina-nanoparticle composites," *Journal of Applied Polymer Science,* vol. 106, pp. 4233-4240, 2007.
[141] H. Yang, P. Bhimaraj, L. Yang, R. W. Siegel, and L. S. Schadler, "Crystal growth in alumina/poly(ethylene terephthalate) nanocomposite films," *Journal of Polymer Science Part B: Polymer Physics,* vol. 45, pp. 747-757, 2007.
[142] J.-H. Chang, S. J. Kim, Y. L. Joo, and S. Im, "Poly(ethylene terephthalate) nanocomposites by in situ interlayer polymerization: the thermo-mechanical properties and morphology of the hybrid fibers," *Polymer,* vol. 45, pp. 919-926, 2004.
[143] X. Yao, X. Tian, X. Zhang, K. Zheng, J. Zheng, H. Zhang*, et al.*, "Poly(ethylene terephthalate)/attapulgite nanocomposites: Preparation, structure, and properties," *Journal of Applied Polymer Science,* vol. 110, pp. 140-146, 2008.
[144] L. S. Brandão, L. C. Mendes, M. E. Medeiros, L. Sirelli, and M. L. Dias, "Thermal and mechanical properties of poly(ethylene terephthalate)/lamellar zirconium phosphate nanocomposites," *Journal of Applied Polymer Science,* vol. 102, pp. 3868-3876, 2006.
[145] H.-B. Zhang, W.-G. Zheng, Q. Yan, Y. Yang, J.-W. Wang, Z.-H. Lu*, et al.*, "Electrically conductive polyethylene terephthalate/graphene nanocomposites prepared by melt compounding," *Polymer,* vol. 51, pp. 1191-1196, 2010.

[146] M. Li and Y. G. Jeong, "Poly(ethylene terephthalate)/exfoliated graphite nanocomposites with improved thermal stability, mechanical and electrical properties," *Composites Part A: Applied Science and Manufacturing,* vol. 42, pp. 560-566, 2011.
[147] M. Herrero, S. Martínez-Gallegos, F. M. Labajos, and V. Rives, "Layered double hydroxide/polyethylene terephthalate nanocomposites. Influence of the intercalated LDH anion and the type of polymerization heating method," *Journal of Solid State Chemistry,* vol. 184, pp. 2862-2869, 2011.
[148] G.-H. Guan, C.-C. Li, and D. Zhang, "Spinning and properties of poly(ethylene terephthalate)/organomontmorillonite nanocomposite fibers," *Journal of Applied Polymer Science,* vol. 95, pp. 1443-1447, 2005.
[149] M.-H. Qu, Y.-Z. Wang, C. Wang, X.-G. Ge, D.-Y. Wang, and Q. Zhou, "A novel method for preparing poly(ethylene terephthalate)/BaSO4 nanocomposites," *European Polymer Journal,* vol. 41, pp. 2569-2574, 2005.
[150] S. H. Jin, Y.-B. Park, and K. H. Yoon, "Rheological and mechanical properties of surface modified multi-walled carbon nanotube-filled PET composite," *Composites Science and Technology,* vol. 67, pp. 3434-3441, 2007.
[151] X. Chen, C. Li, W. Shao, and J. He, "Preparation and properties of poly(ethylene terephthalate)/ATO nanocomposites," *Journal of Applied Polymer Science,* vol. 105, pp. 2783-2790, 2007.
[152] X. Yuan, C. Li, G. Guan, Y. Xiao, and D. Zhang, "Thermal degradation investigation of poly(ethylene terephthalate)/fibrous silicate nanocomposites," *Polymer Degradation and Stability,* vol. 93, pp. 466-475, 2008.
[153] J.-P. He, H.-M. Li, X.-Y. Wang, and Y. Gao, "In situ preparation of poly(ethylene terephthalate)–SiO2 nanocomposites," *European Polymer Journal,* vol. 42, pp. 1128-1134, 2006.
[154] D. Pospiech, A. Korwitz, H. Komber, D. Voigt, D. Jehnichen, J. Müller*, et al.*, "In situ Synthesis of Poly(ethylene terephthalate)/layered Silicate Nanocomposites by Polycondensation," *High Performance Polymers,* vol. 19, pp. 565-580, October 1, 2007 2007.
[155] Y. Li, J. Ma, Y. Wang, and B. Liang, "Synthesis and characterization of sulfonated poly(ethylene terephthalate)/montmorillonite nanocomposites," *Journal of Applied Polymer Science,* vol. 98, pp. 1150-1156, 2005.
[156] J. Y. Kim, H. S. Park, and S. H. Kim, "Multiwall-carbon-nanotube-reinforced poly(ethylene terephthalate) nanocomposites by melt compounding," *Journal of Applied Polymer Science,* vol. 103, pp. 1450-1457, 2007.
[157] J. Bandyopadhyay, S. S. Ray, and M. Bousmina, "Thermal and Thermo-mechanical Properties of Poly(ethylene terephthalate) Nanocomposites," *Journal of Indian Engineering Chemistry,* vol. 13, pp. 614-623, 2007.
[158] C. F. Ou, M. T. Ho, and J. R. Lin, "Synthesis and characterization of poly(ethylene terephthalate) nanocomposites with organoclay," *Journal of Applied Polymer Science,* vol. 91, pp. 140-145, 2004.
[159] S. R. Lim and W. S. Chow, "Impact, thermal, and morphological properties of functionalized rubber toughened-poly(ethylene terephthalate) nanocomposites," *Journal of Applied Polymer Science,* vol. 123, pp. 3173-3181, 2012.
[160] C. Ge, L. Shi, H. Yang, and S. Tang, "Nonisothermal melt crystallization kinetics of poly(ethylene terephthalate)/Barite nanocomposites," *Polymer Composites,* vol. 31, pp. 1504-1514, 2010.
[161] J. K. Kim, K. H. Yoon, D. S. Bang, Y.-B. Park, H.-U. Kim, and Y.-H. Bang, "Morphology and rheological behaviors of poly(ethylene terephthalate) nanocomposites containing polyhedral oligomeric silsesquioxanes," *Journal of Applied Polymer Science,* vol. 107, pp. 272-279, 2008.

[162] J. Zeng, S. Kumar, S. Iyer, D. A. Schiraldi, and R. I. Gonzalez, "Reinforcement of Poly(ethylene terephthalate) Fibers with Polyhedral Oligomeric Silsesquioxanes (POSS)," *High Performance Polymers,* vol. 17, pp. 403-424, September 1, 2005 2005.
[163] K. H. Yoon, M. B. Polk, J. H. Park, B. G. Min, and D. A. Schiraldi, "Properties of poly(ethylene terephthalate) containing epoxy-functionalized polyhedral oligomeric silsesquioxane," *Polymer International,* vol. 54, pp. 47-53, 2005.
[164] R. S. Rajeev, E. Harkin-Jones, K. Soon, T. McNally, G. Menary, C. G. Armstrong*, et al.*, "Studies on the effect of equi-biaxial stretching on the exfoliation of nanoclays in polyethylene terephthalate," *European Polymer Journal,* vol. 45, pp. 332-340, 2009.
[165] R. Feng, G. Guan, W. Zhou, C. Li, D. Zhang, and Y. Xiao, "In situ synthesis of poly(ethylene terephthalate)/graphene composites using a catalyst supported on graphite oxide," *Journal of Materials Chemistry,* vol. 21, pp. 3931-3939, 2011.
[166] A. Al-Jabareen, H. Al-Bustami, H. Harel, and G. Marom, "Improving the oxygen barrier properties of polyethylene terephthalate by graphite nanoplatelets," *Journal of Applied Polymer Science,* vol. 128, pp. 1534-1539, May 2013.
[167] S. Aoyama, Y. T. Park, T. Ougizawa, and C. W. Macosko, "Melt crystallization of poly(ethylene terephthalate): Comparing addition of graphene vs. carbon nanotubes," *Polymer,* vol. 55, pp. 2077-2085, 4/10/ 2014.
[168] Y. Wang, J. Gao, Y. Ma, and U. S. Agarwal, "Study on mechanical properties, thermal stability and crystallization behavior of PET/MMT nanocomposites," *Composites Part B: Engineering,* vol. 37, pp. 399-407, 2006.
[169] A. Greco, A. Timo, and A. Maffezzoli, "Development and Characterization of Amorphous Thermoplastic Matrix Graphene Nanocomposites," *Materials,* vol. 5, pp. 1972-1985, 2012.
[170] I. M. Inuwa, A. Hassan, S. A. Samsudin, M. H. Mohamad Kassim, and M. Jawaid, "Mechanical and thermal properties of exfoliated graphite nanoplatelets reinforced polyethylene terephthalate/polypropylene composites," *Polymer Composites,* pp. n/a-n/a, 2014.
[171] "xGnP Graphene Nanoplatelets - Grade C - Technical Data Sheet," X. S. Inc., Ed., ed: XG Sciences Inc., 2013.
[172] S. Bandla and J. Hanan, "Microstructure and elastic tensile behavior of polyethylene terephthalate-exfoliated graphene nanocomposites," *Journal of Materials Science,* vol. 47, pp. 876-882, 2012.
[173] (2013, 5/5/2013). *xGnP Graphene Nanoplatelets*. Available: http://xgsciences.com/wp-content/uploads/2012/09/About-xGnP.pdf
[174] S. Bandla and J. C. Hanan, "Manufacturing Tough Amorphous Thermoplastic-Graphene Nanocomposites," presented at the Nanotech 2012, Santa Clara, 2012.
[175] D. M. Bryce, *Plastic Injection Molding: Manufacturing Process Fundamentals* vol. 1: Society of Manufacturing Engineers, 1996.
[176] Z. Bashir, I. Al-Aloush, I. Al-Raqibah, and M. Ibrahim, "Evaluation of three methods for the measurement of crystallinity of pet resins, preforms, and bottles," *Polymer Engineering & Science,* vol. 40, pp. 2442-2455, 2000.
[177] ASTM, "Standard Test Method for Determining Inherent Viscosity of Poly(Ethylene Terephthalate) (PET) by Glass Capillary Viscometer," vol. D 4603, ed: ASTM International, 2003.
[178] N. B. Sanches, M. L. Dias, and E. B. A. V. Pacheco, "Comparative techniques for molecular weight evaluation of poly (ethylene terephthalate) (PET)," *Polymer Testing,* vol. 24, pp. 688-693, 9// 2005.
[179] A. Mehta, U. Gaur, and B. Wunderlich, "Equilibrium melting parameters of Poly(ethylene Terephthalate)," *J. of Polym Sci: Polymer Physics Edition,* vol. 16, pp. 289-296, 1978.

[180] M. I. Aranguren, E. Mora, J. V. DeGroot, and C. W. Macosko, "Effect of reinforcing fillers on the rheology of polymer melts," *Journal of Rheology (1978-present),* vol. 36, pp. 1165-1182, 1992.
[181] H. Kim, A. Abdala, and C. W. Macosko, "Graphene/polymer nanocomposites," *Macromolecules,* vol. 43, pp. 6515-6530, 2010.
[182] M. Xanthos, "Modification of Polymer Mechanical and Rheological Properties with Functional Fillers," in *Functional Fillers for Plastics*, M. Xanthos, Ed., ed: Wiley, 2006, pp. 17-38.
[183] J. Vermant, S. Ceccia, M. K. Dolgovskij, P. L. Maffettone, and C. W. Macosko, "Quantifying dispersion of layered nanocomposites via melt rheology," *Journal of Rheology (1978-present),* vol. 51, pp. 429-450, 2007.
[184] M. S. Dresselhaus, A. Jorio, M. Hofmann, G. Dresselhaus, and R. Saito, "Perspectives on Carbon Nanotubes and Graphene Raman Spectroscopy," *Nano Letters,* vol. 10, pp. 751-758, 2010/03/10 2010.
[185] D. Yoon and H. Cheong, "Raman Spectroscopy for Characterization of Graphene," in *Raman Spectroscopy for Nanomaterials Characterization*, C. S. S. R. Kumar, Ed., ed: Springer, 2012, pp. 191-215.
[186] A. J. Melveger, "Laser-raman study of crystallinity changes in poly(ethylene terephthalate)," *Journal of Polymer Science Part A-2: Polymer Physics,* vol. 10, pp. 317-322, 1972.
[187] M. Li and Y. G. Jeong, "Influences of exfoliated graphite on structures, thermal stability, mechanical modulus, and electrical resistivity of poly(butylene terephthalate)," *Journal of Applied Polymer Science,* vol. 125, pp. E532-E540, 2012.
[188] D. Dikin, K. Kohlhaas, G. Dommett, S. Stankovich, and R. Ruoff, "Scanning Electron Microscopy Methods for Analysis of Polymer Nanocomposites," *Microscopy and Microanalysis,* vol. 12, pp. 674-675, 2006.
[189] K. M. Kohlhaas, E. A. Stach, S. Stankovich, and R. S. Ruoff, "Transmission Electron Microscopy of Polymer-Graphene Nanocomposites," *Microscopy and Microanalysis,* vol. 12, pp. 590-591, 2006.
[190] S. K. Basu, A. Tewari, P. D. Fasulo, and W. R. Rodgers, "Transmission electron microscopy based direct mathematical quantifiers for dispersion in nanocomposites," *Applied Physics Letters,* vol. 91, pp. -, 2007.
[191] P. Bleuet, P. Cloetens, P. Gergaud, D. Mariolle, N. Chevalier, R. Tucoulou*, et al.*, "A hard x-ray nanoprobe for scanning and projection nanotomography," *Review of Scientific Instruments,* vol. 80, pp. 056101-3, 2009.
[192] H. Hu, L. Onyebueke, and A. Abatan, "Characterizing and Modeling Mechanical Properties of nanocomposites - Review and Evaluation," *Journal of Minerals & Materials Characterization & Engineering,* vol. 9, p. 45, 2010.
[193] S. Bandla and J. C. Hanan, "Morphology and Failure Behavior of Polyethylene terephthalate-Exfoliated Graphene Nanocomposites," in *ANTEC 2011-69th Annual Technical Conference & Exhibition*, Boston, 2011, pp. 673-676.
[194] P. Huyskens, G. Groeninckx, and P. Vandevyvere, "What Rules the Melting Point of Semi-Crystalline Polymers?," *Bulletin des Sociétés Chimiques Belges,* vol. 99, pp. 1011-1017, 1990.
[195] L. Baldenegro-Perez, D. Navarro-Rodriguez, F. Medellin-Rodriguez, B. Hsiao, C. Avila-Orta, and I. Sics, "Molecular Weight and Crystallization Temperature Effects on Poly(ethylene terephthalate) (PET) Homopolymers, an Isothermal Crystallization Analysis," *Polymers,* vol. 6, pp. 583-600, 2014.
[196] Z. H. Ni, H. M. Wang, J. Kasim, H. M. Fan, T. Yu, Y. H. Wu*, et al.*, "Graphene Thickness Determination Using Reflection and Contrast Spectroscopy," *Nano Letters,* vol. 7, pp. 2758-2763, 2007/09/01 2007.

[197] S. Bandla and J. C. Hanan, "Microstructure and Elastic Tensile behavior of Polyethylene Terephthalate-Exfoliated Graphene Nanocomposites," *Journal of Material Science,* vol. Accepted, 2011.
[198] D. N. Bikiaris and G. P. Karayannidis, "Synthesis and characterisation of branched and partially crosslinked poly(ethylene terephthalate)," *Polymer International,* vol. 52, pp. 1230-1239, 2003.
[199] A. Carré, "Polar interactions at liquid/polymer interfaces," *Journal of Adhesion Science and Technology,* vol. 21, pp. 961-981, 2007/01/01 2007.
[200] M. Hassan, M. Walter, and M. Moseler, "Interactions of polymers with reduced graphene oxide: van der Waals binding energies of benzene on graphene with defects," *Physical Chemistry Chemical Physics,* vol. 16, pp. 33-37, 2014.
[201] S. Aoyama, Y. T. Park, T. Ougizawa, and C. W. Macosko, "Melt crystallization of poly(ethylene terephthalate): Comparing addition of graphene vs. carbon nanotubes," *Polymer*.
[202] M. Boström and B. E. Sernelius, "Repulsive van der Waals forces due to hydrogen exposure on bilayer graphene," *Physical Review A,* vol. 85, p. 012508, 01/11/ 2012.
[203] D. K. Owens and R. C. Wendt, "Estimation of the surface free energy of polymers," *Journal of Applied Polymer Science,* vol. 13, pp. 1741-1747, 1969.
[204] T. Jiang, R. Huang, and Y. Zhu, "Interfacial Sliding and Buckling of Monolayer Graphene on a Stretchable Substrate," *Advanced Functional Materials,* vol. 24, pp. 396-402, 2014.
[205] S. Aoyama, Y. T. Park, C. W. Macosko, T. Ougizawa, and G. Haugstad, "AFM Probing of Polymer/Nanofiller Interfacial Adhesion and Its Correlation with Bulk Mechanical Properties in a Poly(ethylene terephthalate) Nanocomposite," *Langmuir,* vol. 30, pp. 12950-12959, 2014/11/04 2014.
[206] L. Gong, I. A. Kinloch, R. J. Young, I. Riaz, R. Jalil, and K. S. Novoselov, "Interfacial Stress Transfer in a Graphene Monolayer Nanocomposite," *Advanced Materials,* vol. 22, pp. 2694-2697, 2010.

VITA

SUDHEER BANDLA

Candidate for the Degree of

Doctor of Philosophy

Thesis: INJECTION MOLDED POLY(ETHYLENE TEREPHTHALATE)-GRAPHENE NANOCOMPOSITES

Major Field: Mechanical and Aerospace Engineering

Biographical:

Personal Data: Born in Guntur, Andhra Pradesh, India.

Education:

Completed the requirements for the Doctor of Philosophy in Mechanical and Aerospace Engineering at Oklahoma State University, Stillwater, Oklahoma in May, 2015.

Received the Master of Science degree in Mechanical and Aerospace Engineering from Oklahoma State University, Stillwater, Oklahoma, in 2010.

Received the Bachelor of Technology degree in Mechanical Engineering from Acharya Nagarjuna University, Guntur, Andhra Pradesh, India, in 2006.

Experience:
Graduate Research Assistant for Dr. Jay Hanan, Oklahoma State University, Tulsa, OK (2008-2015). Has over 7 years of experience in processing and characterization of polymers and polymer composites, X-ray imaging and diffraction of materials.

Plant Engineer, ESSAR Steels LTD, India (2006-2007)